THE UNIVERSITY OF HULL

Advanced direct laser micro-structuring of polymers
for optical and other applications

being a Thesis submitted for the Degree of Philosophiae Doctor

in the University of Hull

by

Karl Lukas Boehlen,
Dipl. Ing. HTL (BSc) University of Applied Sciences Biel, Switzerland

March 2009

To my Mother,

who very sadly passed

away during these studies.

Acknowledgements

O Lord my God, I will give thanks onto thee for ever.   Psalm 30:12

The writing of a PhD thesis is not possible without the personal as well as academic support of numerous people. Hence I would like to take this opportunity to express my gratitude to all those who gave me the possibility to complete this thesis.

First of all I am indebted to my supervisor Prof Dr Peter E. Dyer at the Department of Physical Sciences of the University of Hull for his continued support and decisive feedback during my work on this thesis. In the same department special thanks go to Ms Judy Slator, Dr Howard Snelling and Dr Chris Walton for their support manifested in different ways. I would also like to thank the friendly staff at the Graduate School of the University of Hull, who readily supplied me with the required information whenever I called.

Furthermore, I am grateful to Dr Phil T. Rumsby and Dr Malcolm C. Gower, the directors of my former employer Exitech Ltd, who introduced me to the world of laser micromachining and gave me the opportunity to carry out the experiments for this thesis, and to my colleagues at Exitech, who welcomed me in the UK and with whom I had the privilege to tackle many challenges in laser micromachining.

I would also like to thank Dr Andrew S. Holmes and Dr James E.A. Pedder of Imperial College London for many fruitful discussions on the subject of excimer laser ablation.

Last, but not least, my thanks go to my family and friends, who encouraged me and helped me to see this thesis through to completion. In particular, I would like to thank my wife Ines; without her perseverance and wide-ranging support I would neither have started nor completed this work. Also my three sons, Pascal, Gabriel and Elias, all born during these studies, deserve my thanks for the little sacrifices they had to make.

                                                                                                 Karl Lukas Boehlen

Table of contents

Abstract

Excimer laser ablation is a very well researched field, and there is a vast amount of publications on this subject. Many of them focus on the fundamentals of the ablation process and try to find models to describe the ablation mechanisms. This doctoral thesis takes the existing research as basis to focus on a more applied approach. Using well-established knowledge of UV ablation of polymers this thesis presents the development of a novel technique for the ablation of repeating micro-structures into polymer surfaces. Applications for these structures include large area optical films, e.g. lenticulars for 3D effect displays.

As motivation for this thesis **chapter 1** gives an overview over the emerging market of advanced micro-structures for displays and novel lighting solutions. State-of-the-art methods of realising micro-structures other than by laser ablation are presented. A review of the history of UV ablation of polymers, mask imaging and industrial applications in this field lays the foundation to validate the potential of employing excimer lasers to ablate complex 3D micro-structures.

In **chapter 2** the so-called Synchronised Image Scanning (SIS), an advanced mask imaging technology, is introduced along with the basic hardware components. The fundamentals of SIS are presented and the evolution of the technique from simple 2D thin film patterning to complex 3D micro-structuring is described. Furthermore, the growing complexity of the mask design as well as considerations regarding the mask set-up in the system are expounded.

Chapter 3 looks more closely at the required hardware and the potential in efficiency, quality and new feature geometries and compares SIS to classical mask imaging methods. For instance, it is outlined that a Step & Repeat approach is not a valid option to ablate millions of features into a surface as it would take far too long while SIS cuts

down process times dramatically by its on-the-flight and parallel processing. Furthermore, a portfolio of a great variety of different 3D features realised with the SIS technology is presented.

Moving on from just qualitative considerations to more quantitative investigations, **chapter 4** describes how a specific micro-lens array design is realised by SIS and analysed in detail using various metrology equipment and optical performance tests. These tests reveal generally a good agreement between design and ablation result. The cause of the relatively high surface roughness of the ablated features is investigated in more detail and the influence of ablation debris on the processed features is discussed.

Chapter 5 looks at artefacts created between individual scans when convex (positive) micro-structures are processed. The appearance of the artefacts is first modelled and then compared to experimental results in order to validate the model. Further it is shown which measures can be used to eliminate these artefacts.

Chapter 6 presents experiments in which the surface quality is enhanced by a laser polish post process. It was found that with the right combination of fluence and number of pulses per area it is possible to reduce the RMS value from 56 nm to 12 nm.

While in all the experiments in the preceding chapters the material ablated was Polycarbonate, in **chapter 7** the SIS technique is applied to a wider range of polymers. It is demonstrated that by finding the etch rate data of the relevant polymers and adapting the process parameters accordingly the technique used for Polycarbonate machining is indeed transferable to other polymers as long as they show a suitable ablation behaviour.

The conclusion and summary **chapter 8** shows that SIS is a valid technology to produce a wide range of feature geometries on large area substrates. Enquiries from next-generation product developers in industries like displays, lighting and anti-counterfeiting show that this technology is indeed relevant for industrial applications.

1 Motivation

1.1 State-of-the-art micro-structures for optical applications

Even though micro-structures in optical applications are widespread, this will not be immediately recognised as these micro-structures are usually not visible. The definition of 'micro' refers to an object as being smaller than an object or scale of focus [1]; it is also 10^{-6} (one millionth) of a meter as an SI unit (μm). Hence the naked human eye cannot see them, and we may be unaware that they play a very important role in many every-day applications like displays, lighting or optical MEMS for telecommunication, imaging and others. The global displays market alone is well on its way to overtake the one for semiconductors and become a $ 100 billion industry. Liquid Crystal Displays (LCDs) have a product span from mobile phones or smaller to big screen TVs, and most of them rely on light management films with micro-structures [2] or, more specifically, micro-prisms [3].

A recent innovation in the lighting market, which is usually associated with the more than 100 years old technology of the light bulb, comes surprisingly close to the light management technique in displays. A range of activities are underway to design light guiding films for illumination purposes, and many of them employ micro-structures to out couple the light. The lighting industry will undergo revolutionary changes in the near future after they have turned their back on the classic light bulb. It is foreseen that Light Emitting Diodes (LEDs) – inorganic and organic – will further expand their market share. The significance of optical micro-structures will rise with the multiplication of LED usage as they are often enhanced with micro-optics [4].

The area of micro-structured films for displays and lighting applications can reach square meters with billions of individual features. There are many modern applications where the need is for optical products that incorporate ever smaller micro-structures in

ever larger formats. This is in contrast to the far smaller areas with a few tens or hundreds of features used in optical MEMS devices. Optical structures like Micro-Lens Arrays (MLAs) are usually fabricated on wafer scale. Micro-lenses and micro-lens arrays are very important optical components in advanced optical and electro-optical systems [5]. The application range is impressive and includes optical communication, data storage, vision and imaging systems and optical metrology. All these require pre-defined and specially designed lenses to enhance performance or to realise a certain optical system.

1.1.1 Existing fabrication methods for micro-structures

The variety of MLAs available is as wide as their application range; basically all different types of lenses that exist for macro-optics − spherical, a-spherical, convex, concave, Fresnel, refractive, diffractive etc. − also exist as MLAs. The fabrication methods for MLAs are nevertheless completely different from those used for macro-lenses. Furthermore, in most cases it is paramount that micro-lenses with accurate surface profiles can be mass-produced; hence advanced replication methods play a key role. The following list of different fabrication options for MLAs and other micro-structure arrays is a selection of the most common state-of-the-art processes.

Photoresist reflow [6,7]: Thick photoresist is lithographically patterned, then developed and etched to leave short cylindrical pillars. By heating the substrate above the melting point of the resist the surface tension pulls the photoresist into a sphere. Sur-
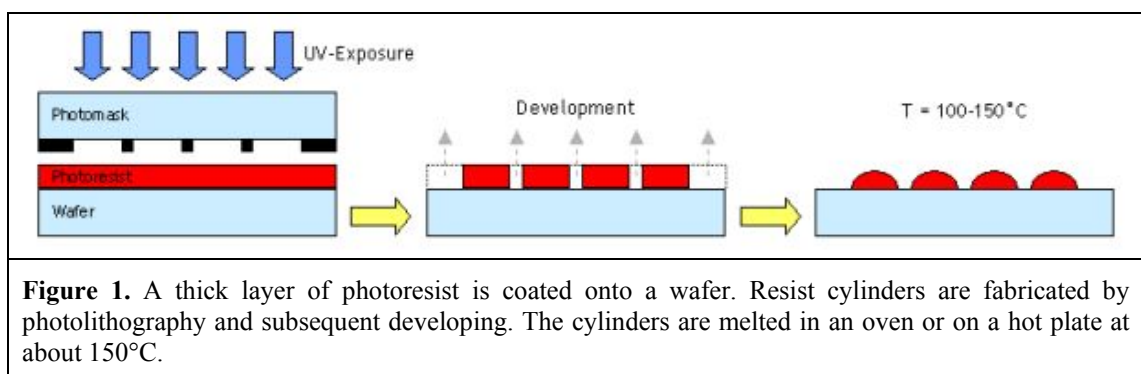
Figure 1. A thick layer of photoresist is coated onto a wafer. Resist cylinders are fabricated by photolithography and subsequent developing. The cylinders are melted in an oven or on a hot plate at about 150°C.

face shape and reproducibility are excellent. However, the difficulty of applying thick photoresist layers limits the sag height of the lenses that can be produced by this method.

Micro-jet fabrication [8]: Optical adhesive or thermoplastic droplets are propelled onto a heated substrate. By controlling coalescence and solidification it is possible to make a-spherical surfaces; controlling the number of droplets and their spacing allows the creation of elliptical and cylindrical lenses.

Direct laser writing of photoresist [9]: A focused laser beam exposes a substrate coated with photoresist on a precision translation table. The surface relief pattern is formed by grey-scale exposure and development of photoresist. Fresnel lenses may be fabricated in this way.

Direct e-beam writing of photoresist [10]: A focused e-beam exposes a photoresist. High resolution writing is possible as spot sizes can be as small as 100 nm. For continuous-relief exposure varying dose and linearising resist are required. It is generally a slow process.

Half-tone and grey-scale mask exposure of resist [11]: Instead of using a writing beam exposure dosage can also be controlled using an imaging system with reduced resolution converting binary half-tone to grey levels and exposing liberalising photoresist [12]. Alternatively a mask made of High Energy Beam Sensitive (HEBS) glass can be written to produce a grey-scale mask.

Figure 2. All thick film lithography processes mentioned above will expose the resist with a variable dose and the 3D structures will remain in the resist after the development process.
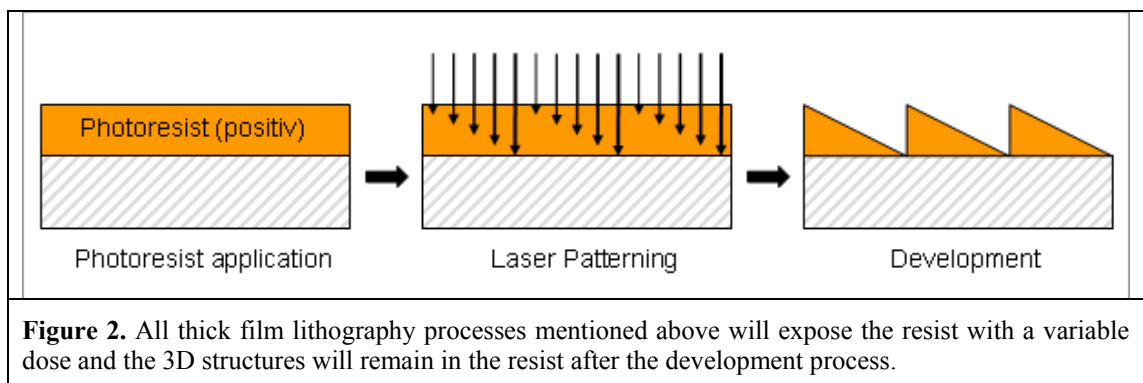
Diamond machining [13]: This is another important technique for producing micro-structures for optical applications; it can be split into two main fields: (a) micro-grooving, where a geometrically defined profile cuts grooves into a metal surface (mostly nickel or copper) and (b) Single-Point Diamond Machining (SPDM), which employs high-precision axes to move a diamond cutting edge over the workpiece to realise a numerically defined surface; high-frequency cutting heads are used to produce micro-optical arrays with SPDM.

Most micro-prism films used today have their origin in a mother plate or drum manufactured with a profiled diamond tool. With single-point diamond machined parts the primary limiting factors for the substrate size are the substrate preparation and the machine tool size. There are lathes that are able to machine Fresnel surfaces of up to 5.0 meters diameter, but fly cutters and drum lathes have limitations in the 1 meter size range. Further factors limiting the substrate size are the durability of the diamond tool and the fact that the probability of impurities in the metal surface in the material increases with the size of the substrate.

Photolithography is mainly driven by the semiconductor industry and has maximum substrate sizes in the 300 millimetre range. Laser writing is machine tool dependent and current size limitations are in the 1 by 1 metre range with significant writing times (10 h for binary exposure).

1.1.2 Replication

An important aspect of micro-optical structures is that they are relatively expensive to fabricate; hence replication methods are often as important as the fabrication technique itself.

Once a master or mother plate has been produced, two main options are available to produce first generation daughters. In many instances, electroforming is used to take the

master and make an exact (but opposite generation) replication. If the master is conductive as is the case with most metals, the part can readily be electroformed. For plastic or photoresist masters, a conductive coating must be applied prior to electroforming. This is usually done with a silver spray process or by evaporating or sputtering a thin conductive metal film on the surface.

An alternative replication process involves UV casting [14]. A liquid polymer material is dispensed between the desired substrate and the profile of the master plate. Then, in a controlled atmosphere, UV illumination initiates the polymerisation of the material. Both processes can be repeated to produce second or third generation daughters which will then be used as tools for production of polymer or glass optics through processes such as injection moulding, compression moulding, hot embossing [15] or UV moulding.

Figure 3. Principle of UV embossing with the mould being pressed into a UV polymer substrate, which is then cured and released from the mould.

1.1.3 Limitations

When looking at the various micro-structuring methods presented above, it can be observed that large area (> 1 m^2) structuring is more or less limited to mechanical diamond machining and laser direct writing. While the mechanical diamond machining is established for micro-prisms and lenticular arrays, it is not suitable for large area MLAs; furthermore, tool wear becomes an important issue when machining large areas. Laser direct writing brings with it the disadvantages of lithography and its etching process; it is also rather slow and expensive.

Driven by the limitations of current technologies in producing optical micro-structures investigations into direct laser ablation as an alternative method are carried out. As a starting point we present reviews on direct ablation of polymers in general and mask imaging techniques in particular.

1.2   Micro-structuring by direct laser ablation – an alternative?

In the following a compact review on ablation of polymers is given. Later, moving from a scientific to a more practical approach, mask imaging and its applications are introduced. Finally state-of-the-art techniques for the fabrication of micro-optical components are presented to investigate if micro-structuring by laser ablation can offer an alternative to the competing technologies mentioned above.

1.2.1   Laser ablation of polymers

It is already more than a quarter of a century since UV laser ablation of polymers was discovered [16,17]. In these past years a large number of papers describing this phenomenon have been published. Many comprehensive reviews are available [18,19,20,21,22]. Already at the outset a combination of practical utility and scientific interest characterised the research into UV ablation of polymers: Srinivasan and his co-workers at IBM were motivated by the potential of mastering direct ablation for the micro-electronic industry. The employment of deep UV lasers opened up the possibility of unprecedented resolution of quasi 3D structures.

Note that this happened on the background that discharge-pumped Rare-Gas Halide (RGH) excimer lasers [23,24] realised years before were further developed to more powerful and reliable tools. The availability of a light source providing discrete lines in a range of UV wavelengths and emitting short and high-power pulses in the tens to hundreds of millijoules at reasonably high repetition rates attracted researchers, and many began to exploit the potential of high-power UV light in different technical areas.

In the beginning UV ablation of polymers was believed to be a purely photochemical effect, where the incident photons have sufficiently high energy (e.g. 5.0 eV for the KrF, 6.4 eV for the ArF laser) to directly break the covalent bonds in the long polymer chains, and are hence responsible for breaking them into small fragment pieces [25,26]. Later, scientists found that laser irradiated material is significantly heated and purely thermal models were proposed [27,28,29,30], coining the term "photothermal" for a process where laser light is the reason for the temperature rise.

Although the nature of photochemical and photothermal processes is very different, in both cases the photoabsorption creates an excited state of the molecules. When keeping the models simple enough both approaches lead to the same basic mathematical expression for etch rates.

If it is accepted that the UV photons have enough energy to break the covalent bonds of a polymer chain and the Bouguer-Lampert-Beer intensity distribution inside the material is taken into account, this "photochemical law" [31] can be found:

$$x = \begin{cases} 0 & \text{if } F < F_T \\ \dfrac{1}{\alpha} \ln\left(\dfrac{F}{F_T}\right) & \text{if } F \geq F_T \end{cases} \qquad \textbf{Equation 1.}$$

Here x is the etch depth per pulse (if the pulse length is < 100 ns), α is the absorption coefficient, F the laser fluence and F_T the threshold fluence. This threshold fluence is the lowest fluence that results in enough fragmentation of polymer chains that material is expelled. In many publications the dependence of $x = x(F)$ is used to describe experimental results, but it is important to note that a measured small segment value for α can differ significantly from an α found by fitting Equation 1 through experimental etch-rate data points. Furthermore, Equation 1 fails to represent the so-called Arrhenius tail [32] at very low fluences where ablation rates do not follow the log function. Equation 1 implies another simplistic view, which assumes that the ablation product

generated within the pulse length [33,34] has the same absorption as the parent solid. With changes taking place in chemical composition, temperature and plasma absorption it is most likely that the ablation plume will differ in respect of absorption compared with the solid. In order to take this into account Equation 1 can be modified to [35]:

$$x = \frac{\mu}{\alpha\mu_p} \cdot \ln\left\{1 + \frac{\mu_p}{\mu}\frac{(F - F_T)}{F_T}\right\}$$ **Equation 2.**

Here $\mu = \alpha/\rho$ is the mass absorption coefficient of the solid and $\mu_p = \alpha_p/\rho_p$ the mass absorption coefficient of the plume. This means that if fits through data points of an $x - \ln F$ plot are non-linear and curving upwards or downwards that the plume is more respectively less transparent than the solid [36].

Looking at the photothermal modelling it was understood that the absorbed energy produces an elevated temperature high enough to decompose the polymer material. The etch depth is calculated as a penetration of the isotherm where the temperature reaches the decomposition value, $T = T_{de}$. An adiabatic approximation for the increase in temperature can be found when neglecting the heat diffusion:

$$\frac{dT}{dt} = \frac{\alpha I}{c_p \rho}$$ **Equation 3.**

Here I is the light intensity at a particular point, c_p is the specific heat capacity of the polymer and ρ is its density. Using the Bouguer-Lambert-Beer intensity distribution, one arrives again at Equation 1 for the etch depth, and the threshold fluence can be estimated as

$$F_T = \frac{c_p \rho T_{de}}{\alpha(1 - R)}$$ **Equation 4.**

where R is the reflection coefficient.

As mentioned above mathematically there is no difference between the above formulated photochemical and photothermal models as in the latter the temperature

plays the role of a photochemical variable. Nonetheless both approaches presented here are over-simplified and cannot fully describe the phenomenon of laser polymer interaction mechanisms as polymers themselves are complex materials.

Formulating more complex approaches based on either pure thermal or pure chemical ablation did not yield a model which is generally applicable. Hence newer theories combine different models like Arnold and Bityurin [37], who present a combination of features of photochemical and thermal surface models. In their model the process follows an Arrhenius-like thermal decomposition of the polymer and assumes that a certain number of bonds have to be broken before ablation is observed. This model predicts an Arrhenius tail and a sharp ablation threshold. However, it has to be said that this model has only been applied to Polyimide and that the laser-material interaction creates conditions which differ significantly from those of usual experiments; hence the relevant parameters cannot be determined (e.g. it is basically guess work what the temperature coefficients are at exceptional high heating rates of $10^{11}Ks^{-1}$).

This led Bityurin et al together with Paltauf and Dyer in their recent reviews in Chem. Rev. [38,39] to the conclusion that modelling of laser ablation of polymers is still far from its completion and that more information on the dynamics of laser ablation and on surface temperature are needed to move forward in this field.

Regardless of the exact mechanism of the ablation process, the technique of inferring the absorption coefficient from etch plots gives a phenomenological characterisation of the ablation process and has proven to be very useful in comparing results obtained under different experimental conditions. From the correlation of surface quality and absorption coefficient it can be concluded that the term 'strong absorber' coincides with the ability to obtain high quality micro-structures with precise definition of the edges and smooth surface profile where thermal side-effects can be ignored. Many polymers

are strong absorbers in the UV range and are therefore perfectly suitable for a wide range of applications.

One of the very first industrial applications of excimer lasers was the via hole drilling of multi-layer Printed Circuit Boards (PCBs) [40] followed by hole drilling for inkjet printer nozzles [41], catheters and fibres [42]. More recently advanced parallel hole laser drilling by employing lens arrays or holograms has been reported [43]. Micromachining of opto-electronic components [44], micro-structuring of large areas for display applications [45], micro-patterning of OLED material [46,47], ablated gratings on polymers [48] and cleaning by ablation [49] are further examples that show how versatile excimer laser ablation is.

Note that for most applications it is not the focused raw beam but a relatively complex beam delivery system with mask imaging which is employed thus exploiting the unique properties of an excimer laser beam. Low coherence, rectangular shape and axis-dependent divergence make it unsuitable for tight focusing but favourable for high-resolution imaging; this is used not only for ablation but hugely successfully in photolithography where presently feature sizes of illumination $\lambda/4$ are achieved [50]. This shows that most likely for ablation, too, the limit in feature miniaturisation is not yet reached.

1.2.2 Excimer laser wavelength, matching polymers, depth and spatial resolution

An excimer laser is a powerful kind of laser which is nearly always operated in the UV and generates nanosecond pulses. The excimer gain medium is a gas mixture, typically containing a noble gas (rare gas) (e.g. argon, krypton, or xenon) and a halogen (e.g. fluorine or chlorine), apart from helium or neon as buffer gas. An excimer gain medium is pumped with short (nanosecond) current pulses in a high-voltage electric discharge.

Energy per Pulse	10 – 1000 mJ
Repetition Rate	10 – 6000 Hz
Power Range	1 – 1000 W
Pulse Length, FWHM	10 – 35 ns
Beam Quality	Large cross-section, multimode
Spatial Coherence	Low
Max. Energy Density	up to 200 Jcm^{-2}
Max. Peak Power Density	up to 1 TWcm^{-2}

Table 1. Key specification ranges of commercially available excimer lasers.

Table 1 shows the technical specification range and top values of commercially available excimer lasers. Different types of excimer lasers emit at wavelengths between 157 and 351 nm. In Table 2 the most common excimer laser wavelengths, the corresponding gas mixtures and photon energies are listed. The photon energy is relevant as the excimer laser radiation is strongly absorbed by molecules via electronic transitions into an excited state. Examples are H-H and O-H bonds, both of which have a bonding energy below the photon energy of the 248 nm wavelength. Nevertheless as discussed earlier it is not finally established if there is a pure photochemical ablation even if the relevant bonds are present in the polymer. Nonethe-

Excimer Laser Wavelength / Gas	Photon Energy	Strongly absorbing Polymer (typical)	Spatial (k·λ/NA, k=0.8) / Depth Resolution (λ/NA^2); NA=0.13
351 nm / XeF	3.53 eV	PI	2.16 μm / 20.77 μm
308 nm / XeCl	4.02 eV	PI	1.9 μm / 18.22 μm
248 nm / KrF	5.00 eV	PC	1.53 μm / 14.67 μm
193 nm / ArF	6.42 eV	PMMA	1.19 μm / 11.42 μm
157 nm / F$_2$	7.90 eV	PTFE	0.97 μm / 9.29 μm

Table 2. List of the most common excimer gases emitting between 157 and 351 μm wavelength and the corresponding photon energy. Example polymers in which at least the calculated spatial and depth resolution is achievable by a given λ are mentioned.

less what can be said is that for a strongly absorbing polymer (optical penetration depth $\alpha^{-1} < 1$ μm) the Heat Affected Zone (HAZ) is so small that the calculated optical resolution limit (spatial and in depth with a NA 0.13 lens; see Table 2) is not breached by the ablation behaviour of the material. In fact it is possible to achieve better than the optical resolution as reported earlier [51].
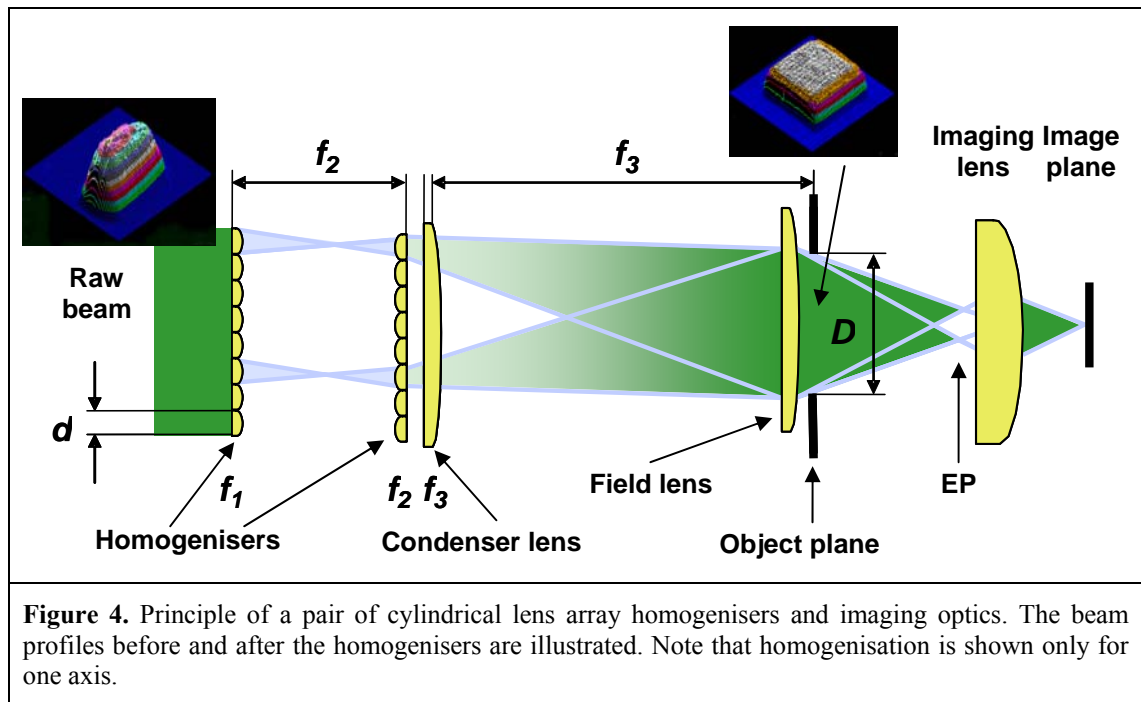
The choice of the right excimer laser wavelength for direct ablation is not only influenced by the absorption of the polymer although this is the crucial factor. Looking

at PMMA for instance the absorptivity changes two orders of magnitude from 2000 cm^{-1} at 193 nm over 200 cm^{-1} at 248 nm to 20 cm^{-1} at 308 nm excimer radiation [52]. Taking these figures into consideration only 193 nm can be regarded as a valid wavelength for high quality ablation in PMMA. Nevertheless there are other polymers like Polyimide which have a strong absorption in the whole UV range and the quality of ablation is more or less constant. In this case, mainly for economical reasons, another factor influences the choice of the wavelength. It can generally be said that the shorter the wavelength the more expensive it gets as the output power of the laser goes down with the wavelength while the costs for beam delivering optics and their degradation go up. Additionally the ablation process is generally more efficient at the longer wavelength. For Polyimide (Kapton) for instance the ablation depth per pulse at 1 Jcm^{-2} at 308 nm radiation is with 0.51 μm more than 3 times higher and at 248 nm with 0.35 μm still more than double than at 193 nm reaching 0.16 μm [53]. Hence it is self-evident that for an industrial application like inkjet printer nozzle drilling the longest excimer wavelength ensuring the required quality is chosen. As a summary it can be said that the polymer to be machined determines the excimer wavelength first from an ablation quality and second from an economical point of view.

1.2.3 Excimer laser mask imaging techniques for ablation

As mentioned above excimer lasers are well suited to illuminate masks. Nevertheless to achieve high quality results the raw laser beam needs to be treated (homogenised) to correct for its non-uniform intensity profile. Different types of homogenisers are known [54,55,56,57]. What they all have in common is that they divide the laser beam into multiple small beamlets, which are then overlapped or combined at the mask plane. For industrial applications homogenisers as the ones shown in Figure 4 have found the highest resonance. For each axis of the raw beam, they are composed of individually

polished cylindrical lens arrays (f_1 and f_2) arranged as a pair and combined with a condenser lens (f_3). The mask illumination D is then given by $D = (f_3 / f_2) \cdot d$ where d is the aperture size of one cylindrical lens. Typical beam profiles of the raw beam and at the object plane and the rest of the beam delivery system including telecentric imaging lens are also shown.

Figure 4. Principle of a pair of cylindrical lens array homogenisers and imaging optics. The beam profiles before and after the homogenisers are illustrated. Note that homogenisation is shown only for one axis.

Although mask techniques like contact and proximity masks used in photolithography can also be employed in direct ablation [58], the relatively high fluence and the debris deposition favour mask projection imaging.

Several variations of mask imaging techniques for pulsed laser ablation are employed in industrial applications. What follows is a brief overview over the state of the art. There are generally speaking three main elements when looking at mask projection: the mask, the lens and the workpiece or target. Furthermore we have three modes of translation: static, Move & Stop (also known as Step and Repeat) and continuous translation. Since the fill factor of the imaging lens should be optimised, is it not usually satisfactory to translate the lens relative to the beam axis. Table 3 lists the most common techniques together with a brief description of each; for the sake of simplicity the lens is left out in
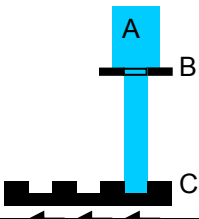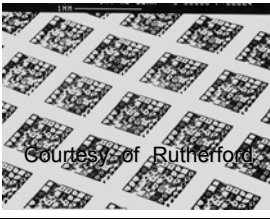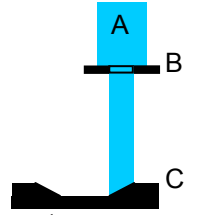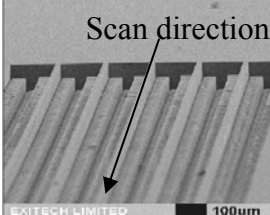
Technique	Example picture	Description
Step & Repeat	Ref [59]	
	Courtesy of Rutherford	The basis for Step & Repeat is the all static exposure. Beam position (A), mask (B) and target (C) are static throughout exposure until the required depth is achieved; then translation between C and (A&B) perpendicular to the beam axis is introduced and a new position is exposed.
Image Dragging	Ref [60]	
	Scan direction	For Image Dragging there is a relative translation between the unit of beam and mask (A&B) and the target (C) during exposure. Hence the imaged mask pattern is dragged over the workpiece ablating a channel with a profile corresponding to the mask pattern geometry.
Mask Dragging	Ref [61]	
		In addition to the mask (B) containing the geometry of the ablation pattern a moving aperture (D) is introduced. Beam (A), mask (B) and target (C) are kept static while D is moved during exposure enabling a modulated depth profile.
Mask Scanning	Ref [62]	
		Synchronised translation between the mask (B) and workpiece (C) enables the imaging of objects which are bigger than the available beam size. Given by the nature of the imaging lens (D) the two scan movements are in opposite directions and the factor between the scan velocities is equal to the magnification factor of the lens.
Mask Changing	Ref [59]	
		For Mask Changing the beam (A), mask (B) and target (C) are kept static during one sub-exposure. The same target position is then exposed with several different mask patterns in a Step & Repeat process at mask level. The same effect is achievable with a variable aperture.
Half-tone / Grey-scale Mask	Ref [63]	
		The half-tone / grey-scale pixels in the mask pattern modulate the intensity profile of the beam, hence linear and non-linear depth profiles are achievable with simple static exposure. Image Dragging can be done with a half-tone mask to achieve extra-long features.
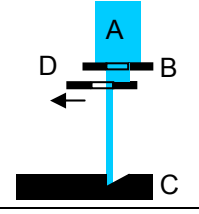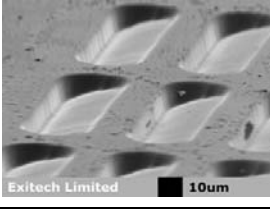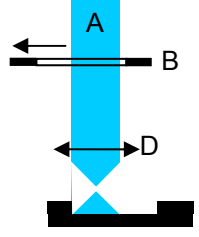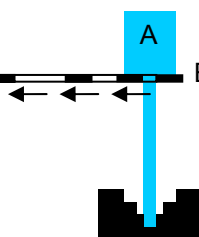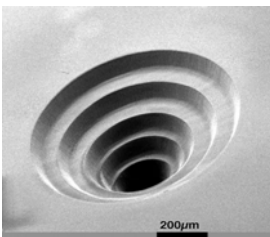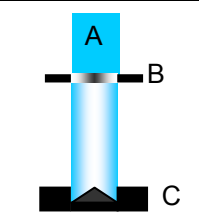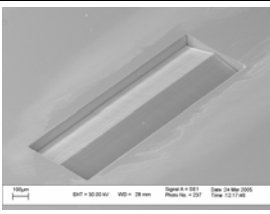
Table 3. State-of-the-art mask imaging techniques for the ablation of micro-structures.

all the sketches but the one for the Mask Scanning where it makes a significant difference.

The techniques introduced above can be regarded as a toolbox to realise 2D and 3D micro-structures. One of the techniques or a combination thereof can be chosen to create the geometry of a given micro-structure [64]. This enables a rich activity for prototyping of micro-structures ranging from micro-fluidic to micro-optical components [65].

More details are given in the following section where the focus is on advanced ablation techniques for micro-optical components.

1.2.4 Advanced mask imaging techniques for optical applications

The most popular optical micro-structures are micro-prisms and micro-lenses; for both advanced laser ablation techniques exist. Excimer laser ablated lenses have been demonstrated [66] and can be used to increase the coupling efficiency of optical fibres [67], and laser ablated prisms are used for instance to enhance displays [68]. Maybe the most dramatic application that involves laser ablation of an optical surface by mask imaging is in correction of the human cornea. Both PhotoRefractive Kreatectomy (PRK) on the surface or LAser in-SItu Keratomileusis (LASIK) underneath the surface employ one of the same three possible laser ablation methods to either flatten the cornea for the correction of Myopia (short-sightedness) or steepen the cornea for correction of Hyperopia (far-sightedness). The approaches taken are:

(A) Static ablation: Aperture size changes during laser firing produce the required flattening (principle of mask changing or variable aperture technique).

(B) Scanning slit ablation: Scanning an image of a slit aperture in a criss-cross manner across the surface.

(C) Flying spot ablation: Scanning a relatively small spot (~1 mm diameter) in a circular trajectory.

Newer techniques combine (A) and (C) and employ a flying spot with variable diameter to be able to correct for more complex wave front errors of the eye including astigmatism. In all approaches depth accuracies of around 100 nm and total cut depth of 20 to 50 μm are common.

The principle of the flying spot ablation has been reported for the manufacturing of micro-cones [69], and Naessens *et al* have further developed the technique of a circling spot to fabricate micro-lenses [70]. While this method offers flexibility with a relatively simple setup, the machining time per lens and the size of the affected area around the lens are clear disadvantages and make this method unfit for larger lens arrays. Neither do more sophisticated flower-like mask geometries as proposed in [71] address these issues. Better suited for lens or prism arrays are techniques based on Image Dragging as described by several authors [72,73,74].

All these reports show that excimer laser mask projection is well suited for processing not only binary 3D features but also structures with continuously changing depth profile. Although proof of principle is given, excimer laser mask projection for 3D optical structures has not yet had the breakthrough into industrial use beyond prototyping. The reason for this can be found in long processing times, low surface and geometrical quality and lack of feature consistency.

To address these issues a novel mask imaging technique was invented [75] and further developed. This technique and extensive investigations into it are presented in detail in the following chapters. The basic principle of this technique called Synchronised Image Scanning (SIS) [76,77] is here briefly described as follows and illustrated in Figure 5. Similar to the Mask Changing technique several mask positions are superimposed at one target position. The difference is that beam (A) illuminates several patterns at the mask (B) simultaneously and the workpiece (C) is moved continuously coupled to a synchronised pulse trigger to ensure accurate superposition.

Figure 5. (A) Laser beam, (B) mask pattern, (C) workpiece. The workpiece is moved from right to left. The laser is triggered every time the workpiece is translated by the distance *x*.

Figure 6. Typical result if workpiece is scanned in the way described on the left.
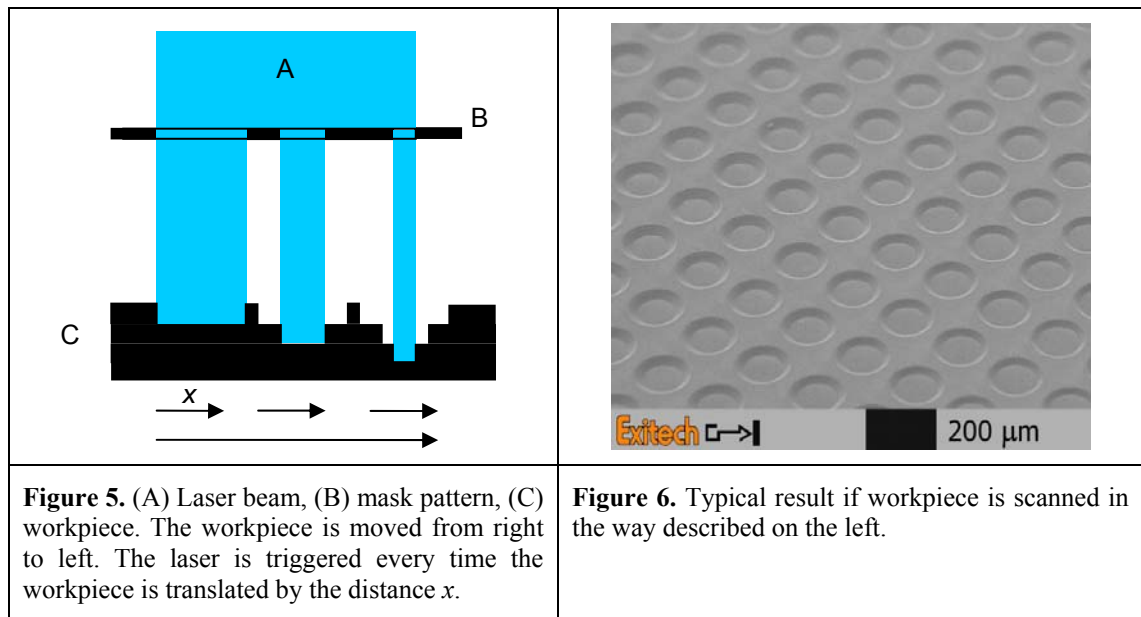
In the following chapters a detailed description of and thorough investigation into SIS are presented.

---

1. http://en.wikipedia.org/wiki/Micro

2. Y.-P. Huang, H.-P. D. Shieh, S-T. Wu, Appl. Opt. 43, 18, (2004)

3. Patent: WO2006132913, Brightness Enhancing Film and display device having the same, 3M Innovative properties CO (US)

4. LEDmagazine.com, July 2005, pp27

5. H.P. Herzig, Micro-optics: Elements System and Applications, Taylor & Francis Ltd., Bristol, PA, 1997

6. Z.D. Popovic, R. A. Sprague, G. A. Davies, Appl. Opt. 27, 1281 (1988)

7. D. Daly, R.F. Stevens, M.C. Hutley, N. Davies, J. Meas. Sci. Technol. 1, 759 (1990)

8. D.L. MacFarlane, V. Narayan, J.A. Tatum, W.R. Cox, T. Chen and D.J. Hayes, IEEE Photonics Tech. Lett. 6, 1112 (1994)

9. M.T. Gale, M. Rossi, J. Pedersen, and H. Schutz, Opt. Eng. 33, 3556 (1994).

10. M.T. Gale, in Micro-optics: Elements System and Applications, H. P. Herzig, ed., Taylor & Francis Ltd., Bristol, PA, 1997

11. H.J. Quenzer, W. Henke, W. Hoppe, W. Pilz, K. Reimer, B. Wagner, Microsys. Tech. 1, No. 4, 169, (2005)

12. J.J. Yang, Y.S. Liao, C-F. Chen, Opt. Com. 270, 433, (2007)

13. W.C. Sweatt, D.D. Gill, D.P. Adams, M.J. Vasile, A.A. Claudet, IEEE. 4 , Issue 11, 6, (2006)

14. M.T. Gale, SPIE Vol. 1577, 113 (2003)

15. X.C. Shan, R. Maeda, Y. Murakoshi, Jap. J. Appl. Phys., 42, 6B, 3859 (2003)

16. R. Srinivasan, V. Mayne-Banton, Appl. Phys. Lett.41, 576 (1982)

17. Y. Kawamura, K. Toyoda, S. Namba, Appl. Phys. Lett. 40, 374 (1982)

18. R. Srinivasan, B. Braren, Chem. Rev. 89, 1303 (1989)

19. J.C. Miller, R. Haglung, Jr.Eds, Laser Ablation Mechanisms and Applications, Springer-Verlag, Berlin (1991)

20. E. Fogarassy, S. Lazare, Laser Ablation of Electronic Materials – Basic Mechanisms and Applications, Elsevier, Amsterdam (1992)

21. P.E. Dyer, Laser Ablation of Polymers, in Photochemical Processing of Electronic Materials, ed. By I.W. Boyd, R.B. Jackman (Academic, London 1992)

22. D. Bäuerle, Laser Processing and Chemistry, 3rd ed, Springer, (2000)

23. R. Burnham, N. Harris, N. Dieu, Appl. Phys. Lett. 28, 86 (1976)

24. C. Wang, H. Mirels, D. Sutton, S. Suchard, Appl. Phys. Lett. 28, 326 (1976)

25. H.H.G. Jellinek, R. Srinivasan, Phys. Chem. 88, 3048 (1984)

26. J.E. Andrew, P.E. Dyer, D. Foster, P.H. Key, Appl. Phys. Lett. 43, 717 (1983)

27. P.E. Dyer, G.A. Oldershaw, J. Sidhu, Appl. Phys, B48, 489 (1989)

28. D. Dijkkamp, A.S. Gozdz, T. Venkatesan, X.D. Wu, Phys. Rev. Lett. 58, 2142 (1987)

29. S. Küper, J. Brannon, K. Brannon, Appl. Phys. Lett. 48, 1226 (1986)

30. G.A. Oldershaw, Chem. Phys. Lett. 186, 23 (1991)

31. J.E. Andrew, P.E. Dyer, D. Forster, P.H. Key, Appl. Phys. Lett. 43, 717 (1983)

32. J. Frisoli, Y. Hefetz, T. Deutsch, Appl. Phys. B 52, 168 (1991)

33. R. Srinivasan, Appl. Phys. 73, 2743 (1993)

34. P. Simon, Appl. Phys. B 48, 253 (1989)

35. K. Schildbach, SPIE Vol. 1279 (1990)

36. P.E. Dyer, SPIE Vol. 3092 (1997)

37. N. Arnold, N. Bityurin, Appl. Phys. A 68, 615 (1999)

38. N. Bityurin, B.S. Luk'yanchuk, M.H. Hong, T.C. Chong, Chem. Rev. 103, 519 (2003)

39. G. Paltauf, P.E. Dyer, Chem. Rev. 103, 487 (2003)

40. F. Bachmann, Appl. Surface Science 46, 254 (1990)

41. Patent: US 5305015, Laser ablated nozzle member for inkjet printhead, Hewlett-Packard Company (US)

42. M. Gower, SPIE Vol. 3618, 251 (1999)

43. M. Hatcher, Opto & Laser Europe Issue 94, 12 (2002)

44. B.L. Booth, Polymers for Lightwave and Integrated Optics, ed. L. Hornak, Dekker, New York (1992)

45. K.L. Boehlen, I.B. Stassen Boehlen, R. Allott, SPIE Vol. 5720, 204 (2005)

46. D.G. Lidzey, M. Voigt, C. Giebeler, A. Buckley, Jeff Wright, K. Boehlen, J. Fieret, Ric Allott, Organic Elec. 6, 221 (2005)

47. Patent: WO2005/101505A2, Method of patterning a functional material on to a substrate, Exitech Ltd (UK)

48. P.E. Dyer, R.J. Farley, R. Giedl, C. Ragdale, D. Reid, Appl. Phys. Lett. 64, 3389 (1994)

49. E. Hontzopoulos, C. Fotakis, M. Doulgerdis, SPIE Vol. 1820, 749, (1992)

50. B.J. Lin, Microel. Eng., 83, 4-9, 604 (2006)

51. K. L Boehlen, Phil T Rumsby, Neil Sykes, Celine Lefevre, SPIE Vol. 6261 (2006)

52. R. Srinivasan, B. Braren, Appl. Phys. A 45, (1988)

53. R. Srinivasan, Lambda Highlights 1, (1986)

54. K. Mann, A. Hopfmueller, P. Grozellik, R. Schmid, W. Stoeffler, H. Wagner, G. Wolbold, SPIE Vol. 1834, 184 (1993)

55. K. Jasper, S. Scheede, B. Burghardt, R. Senczuk, P. Berger, H.J. Kahlert, H. Hügel, Appl. Phys. A 69, 312 (1999)

56. C. Lewis, I. Weaver, L. Doyle, G. Martin, T. Morrow, D. Pepler, C. Danson, I. Ross, Scientific Intr. 70, 2116 (1999)

57. Y. Kato, K. Mima, N. Miyanaga, S. Aringa, Y. Kitagawa, M. Nakatusuka, C. Yamanaka, Phys. Lett 53, 1057 (1984)

58. J. Brannon, J. Lankard, et al. J. Appl. Phys. 58 (5), 2036 (1985)

59. E.C. Harvey, P.T. Rumsby, M.C. Gower, J.L. Remnant, SPIE Vol. 2452, 351 (1994)

60. N.H. Rizvi, SPIE Vol. 3680, 546 (1999)

61. N.H. Rizvi, P. Apte, J. Mat. Proc. Tech. 127, Issue 2, 206 (2002)

62. P. Rumbsby, E. Harvey, D. Thomas, N. Rizvi, SPIE Vol. 3184, 176 (1997)

63. A.S. Holmes, IEE, Sci. Meas. Tech., 151 (2), 85 (2004)

64. K. Zimmer, A. Braun, F. Bigl, Appl. Surf. Sci. 154–155, 601 (2000)

65. M. Gower, Riken Review No32, 50 (2001)

66. T. Fricke-Begemann, J. Li, J. Ihlemann, P.R. Herman, G. Matowsky, SPIE Vol. 5578, 589 (2004)

67. M. Rabarot, L. Fulbert, E. Molva, P. Thony, V. Marty, S. Dastouet, Pure Appl. Opt. 6 699–705 (1997)

68. N.H. Rizvi, J. Greuters, J. Dallimore, K. Hamilton, R. Clabburn, B. Ebsworth, SPIE Vol. 4274, 278 (2001)

69. K.L. Boehlen, P. Rumsby, A. Cerezo, M. Huang, SPIE Vol. 4557, 129 (2001)

70. K. Naessens, H. Ottevaere, P. Van Daele, R. Beats, Appl. Surf. Sci. 208, 159 (2003)

71. Y-C. Lee, C-M. Chen, C-Y Wu, Sen. & Act. A, 117, 349 (2005)

72. K. Zimmer, A. Braun, F. Bigl, Appl. Surf. Sci. 154, 601 (2000)

73. C.T. Pan, S.C. Shen, C-C. Hsieh, C-H. Chien, Y-C. Chen, J. Microlith. Microfab. Microsyst. 3, 4 (2004)

74. S-Y. Wang, J. Micromech. Microeng. 15, 1310 (2005)

75. Patent: WO 2007/135379A3, Method and unit for micro-structuring a moving substrate, Exitech Ltd, K. Boehlen

76. H.J. Booth, Thin Solid Films, 453-454, 450 (2004)

77. K.L. Boehlen, I.B. Stassen-Boehlen, SPIE Vol. 5339, 118 (2004)

2 Synchronised Image Scanning

2.1 Introduction

Synchronised Image Scanning (SIS hereafter) is an on-the-flight micro-structuring process producing uniformly repeated 2D or 3D micro-structures. This chapter presents the experimental set-up and gives a detailed description of the process using four different applications of increasing complexity as illustrations.

2.2 System used for experiments

The majority of the results and data presented in this thesis were acquired by employing an Exitech M8000 micromachining tool. In this section the tool is described in detail as the individual components can have a significant influence on the final result.

The elements of the experimental set-up are shown in Figure 7. The laser (1) is in this case a Lambda Physik LPX 220. It is run with a KrF gas mixture producing a wavelength of $\lambda = 248$ nm with a maximum pulse energy of 400 mJ and a maximum repetition rate f_p of 200 Hz. The dimensions of the direct output beam are approximately 24 mm (long axis with flat-topped intensity distribution) and 12 mm (short axis with Gaussian intensity distribution). The energy of the laser pulses at the workpiece can be controlled by a dielectric double plate attenuator (2) in a transmission range from 10 – 90%; the angles of the plates are numerically controlled.

A Kepler telescope with spherical lenses expands and relays the out beam (3). The ex-
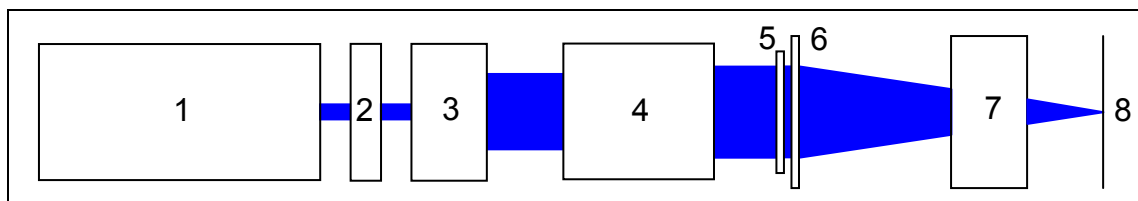

Figure 7. Major hardware elements of the Exitech M8000 used for the experiments: 1) excimer laser, 2) variable attenuator, 3) relay optics and beam expander, 4) homogeniser optics, 5) field lens, 6) manual mask stage with *x*-, *y*-, φ-axes and tip-tilt, 7) imaging lens, 8) workpiece stages with numerically controlled *x*-, *y*-, *z*-, φ-axes.

pansion serves to fully illuminate the first set of homogenisers. To achieve a homogenous illumination at the mask plane two pairs of cylindrical arrays with a condenser lens each are used (4). There is one pair of arrays for the long and one for the short axis of the beam. Beam shaping has two main purposes: one is to obtain a uniform irradiance distribution across the whole beam in the mask plane and the other to actually shape the beam to illuminate a given footprint at the mask. The Radius Of Curvature (ROC) and position are chosen to give a rectangular beam of 70 mm x 6 mm at the mask plane. Beam shaping and mask imaging system are explained in subsection 1.2.3. It can be argued that beam shaping is not essential to successfully perform basic SIS and that it is a big advantage of this technique that a perfect top flat beam is not required to achieve good results. Nevertheless – as will be shown later – for more advanced SIS applications beam shaping is important.

Just before the mask plane there are two cylindrical field lenses (5), which image the light source into the entrance pupil of the imaging lens. The study in this thesis employs a laser ablation mask projection system where the mask (6) is of binary nature, e.g. patterned chrome on quartz or a metal aperture mask. A binary mask has areas where most of the photons emitted by the laser in the system are either absorbed or reflected away from the target and areas where most of the photons are transmitted towards the target; the intensity level after the mask is therefore normalised to either 1 or 0 over the mask pattern. Other types of mask could be used, (e.g. grey-scale or phase masks), provided the defined pattern produces a sufficiently high energy density at the workpiece. However, experiments with these kinds of masks are beyond the scope of the present work and require a system layout different from the one shown above.

The manual mask stages can hold masks up to a size of 6" x 6" and permit x and y movement relative to the laser beam and in-plane rotation φ by a few degrees. With the tip-tilt adjustment the mask can be made perpendicular to the laser beam.

The imaging lens (7) is a telecentric lens with 5x demagnification, an NA of 0.13 and a maximum image field of 18 mm diameter. The lens sits on a kinematic mount to ensure that the right magnification can be found and to line up the lens with the laser beam.

The workpiece is brought into position by a stack of stages (8) consisting of very high resolution (10 nm) air bearing stages (Aerotech) for the *x*- and *y*-axes where both axes sit on the same lapped granite surface. On top of the main axis sit a rotary and an elevator stage. In both *x*- and *y*-directions there is a maximum of 250 mm travel. The stages are driven by DR 500 amplifiers and commanded by a U500 (Aerotech) card in a PC running under Windows NT.

There is furthermore an alignment camera installed which allows features already on the workpiece to be precisely aligned with the image area. The system has also a gas assist nozzle installed to direct a gas jet onto the ablation site.

2.3   Detailed description of the SIS process

The method presented here employs an excimer laser mask projection system. The mask object is imaged onto a workpiece while both are in relative motion to each other and laser pulses are triggered by a position sensor, i.e. the image is scanned over the workpiece in a synchronised manner [1]. Although in the majority of cases it is the workpiece that moves, it is also possible to keep the workpiece static and to move the image as long as the projection lens, the mask, the field lens and the laser beam form a rigid unit without movement relative to each other.

In most cases each laser pulse provides less than the amount of illumination necessary to completely ablate a structure in the substrate. In order to provide additional illumination the substrate and the image are translated relative to each other by a distance less than the image field between laser pulses so that a different part of the image exposes the unfinished feature on the workpiece, and thus the features are ablated

layer by layer. Accordingly the mask consists of an array of apertures at a constant pitch, which are all simultaneously illuminated by the incoming laser pulse. Figure 8 shows on the left a schematic of the SIS process with mask, laser beam and projection lens kept static and the workpiece moving.

Figure 8. On the left a schematic of SIS with static mask, laser beam and projection lens position scanning over a moving workpiece. On the right a graph of the encoder signal train of laser pulse triggering for SIS: x = stage travel in mm, y = encoder signals, d = firing distance and z = number of encoder pulses between laser pulses.
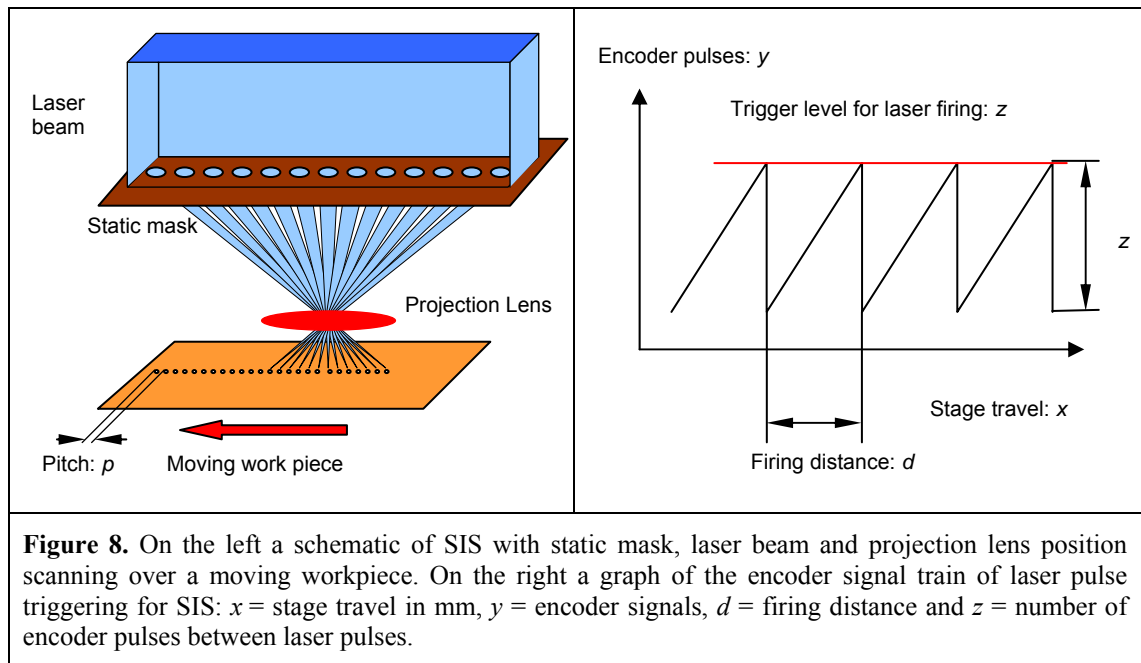
On the right a graph of a typical encoder signal train of laser pulse triggering for SIS is shown. It illustrates how the number of encoder pulses increases until it reaches a user-defined level, at which a laser pulse is triggered, and then starts again at zero. To find out how many encoder signals there are between each laser pulse the number of encoder signals per millimetre needs to be multiplied by the firing distance. It is obvious that in this case the stage movement does not need to be constant to ensure that the laser is triggered at a given pitch.

In principle it is not essential to trigger the laser directly linked by position. A constant velocity and trigger signal repetition rate will also result in a constant firing distance on the workpiece.

As the apertures in the mask are on an equal pitch p / m, where p is the pitch of the features on the workpiece and m the lens magnification, it is possible to choose the

number of shots per area n_s on the workpiece and derive the corresponding firing distance d as follows:

$$d = \frac{n_a}{n_s} \cdot p$$

Equation 5.

where n_a is the number of apertures in the mask. It is obvious that n_a / n_s needs to be an integer.

It is always possible to choose $d = p$ or $d = n_a \cdot p$ resulting in the maximum and minimum number of shots per area in one scan respectively. The minimum is one shot per area and represents the very simplest case of SIS, which is nevertheless useful for thin film patterning. Firing at an interval of $d = p$ opens up the possibilities of SIS to machine more complex repetitive structures with 3D features as individual elements.

In the following we consider four different applications of increasing complexity in order to illustrate various aspects of the SIS process:

Application	Characteristics
1. Thin film patterning	- few shots per area - all apertures in the mask are identical
2. Hole drilling	- many shots per area - all apertures in the mask are identical
3. Nozzle drilling	- many shots per area - all apertures in the mask are of identical shape, but different in size
4. Structuring a surface with 3D micro-features	- many shots per area - different apertures in the mask
Table 4. Overview over four different applications and their characteristics.	

2.3.1 Thin film patterning

Patterning thin films, e.g. Indium Tin Oxide (ITO) on Glass, ITO on organics or Chrome on Glass, is essentially a 2D process. Only one or a few shots per area are needed to remove thin films completely [2,3,4,5]. Therefore an individual feature of the

repetitive pattern (scaled to account for the magnification of the imaging lens) or an array of copies thereof is represented in the mask object and imaged onto the workpiece. Consider the following example: an area is to be patterned with 50 μm x 50 μm squares on a 100 μm pitch; the required ablation fluence is 200 mJcm^{-2}. Taking into account that the laser beam of our micromachining system is 70 mm x 6 mm at the mask and that the imaging lens has 5x demagnification, the mask pattern could consist of a linear array of 100 squares, each 250 μm x 250 μm, at a pitch of 0.5 mm. This fits easily into the beam. The firing distance d can be derived from the number of shots per area n_a using Equation 5: if 1 shot per area is sufficient, the firing distance is $100 \cdot 0.5$ mm $/ 5 = 10$ mm; if 5 shots per area are needed, the firing distance has to be 2 mm. As mentioned before, the number of apertures in the mask has to be a multiple of the number of shots per area required. Triggering the laser accordingly, we can now scan the image over the workpiece thus completing one row of ablated features. We then step one pitch perpendicularly to the scan direction and scan the image again over the workpiece to complete the second row of features. In this way we step and scan until the whole area is patterned.

Obviously, this process can be made more efficient by putting several rows of square apertures in the mask. The beam width of 6 mm at the mask allows 10 rows of squares to be fitted into the illuminating beam, forming a pattern of 100 x 10 squares. With this new mask one scan completes 10 rows of features on the workpiece; accordingly the subsequent step needs to be 10 times the pitch.

There is nothing to prevent scanning parallel to the short axis of the mask. This allows completion of 100 rows of features in one scan; however, the firing distance is reduced by a factor of 10. Which of the two scan directions makes the process more efficient depends on the specifications of the hardware. As the micromachining system available has a maximum laser pulse frequency of 200 Hz and a maximum stage speed of

50 mms^{-1}, the following options are available (assuming that 10 shots per area are required): (i) scan in the long axis of the mask with a firing distance of 1 mm running the system at the maximum stage speed and finishing 5000 squares/s (ii) scan in the short axis of the mask with a firing distance of 0.1 mm running the laser at 200 Hz and the stages at 20 mms^{-1} and finishing 20000 squares/s. For efficiency the short axis scan is the obvious choice.

2.3.2 Hole drilling

As thin film patterning, hole drilling requires a mask with an array (ideally 2D) of identical apertures (in the case of cylindrical holes the apertures are circular, but other shapes are equally possible). Thus the considerations of the previous subsection are still valid in the present context.

The main difference between thin film patterning and hole drilling [6] is that hole drilling requires many more shots per area, often several hundred. This has the following implication:

2.3.2.1 *Multiple scans*

As explained above the maximum number of shots per area in one scan is given by the number of apertures in the mask. We recall that all the apertures must be illuminated simultaneously by the laser beam. And so it may well happen that the number of apertures that can be accommodated at the required pitch p / m is smaller than the required number of shots per area n_s. If this is the case, the image needs to be scanned over the same holes several times.

Consider the following example: a grid of holes at a pitch of 200 μm needs to be drilled into a Polyimide (PI) film of 50 μm thickness; around 200 shots are needed to drill through this substrate. Accounting for the demagnification of the imaging lens, the pitch of the apertures at the mask needs to be 1 mm. As the length of the beam at the mask is

70 mm, a maximum of 69 apertures can be accommodated, corresponding to a maximum of 69 shots per area in one scan. Hence three scans are needed to drill through the 50 μm Polyimide.

2.3.3 Nozzle drilling

This subsection explains how SIS can be used to drill nozzles, i.e. tapered holes.

2.3.3.1 Mask design for tapered holes

By the nature of SIS every hole at the workpiece is scanned by the entire image; the result is the superposition of every individual aperture illumination. The conclusion can now be drawn that linearly decreasing or increasing apertures will result in a tapered hole in the workpiece. Using this technique it is theoretically possible to create any taper angle as long as it is bigger than the minimal wall angle[1] achievable with constant aperture size. This depends on the NA of the imaging lens as well as the fluence and may well be a negative taper [7]. Figure 9 illustrates the principle of SIS mask design used to fabricate nozzles with a controlled taper.
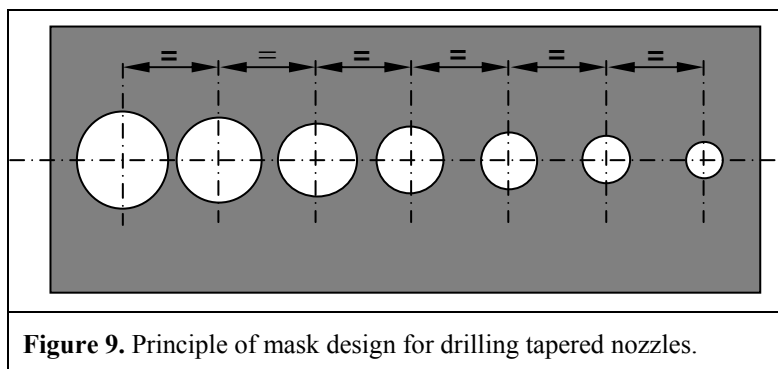
Figure 9. Principle of mask design for drilling tapered nozzles.

One individual position at the workpiece is scanned by the entire image; hence it sees the whole series of apertures. It depends on the scan direction whether the biggest or the smallest aperture is the first to illuminate the workpiece; the discussion here concentrates on the former case (for a comparison of the two scan directions cf.

---

[1] In this context the 'wall angle' is defined as the angle between the machined slope and the vertical axis positioned at the deepest point of the feature. The angle is positive if the feature opens up towards the top and negative if the feature opens up towards the bottom.

subsection 2.3.3.4). Figure 10 illustrates the light from subsequent laser pulses coming through the different apertures and the resulting ablation of the workpiece. The light from the first laser pulse is shaped by the biggest aperture (red); it hits the unexposed surface and removes a shallow cylinder-like volume (provided that the energy density is above the ablation threshold). Given a uniform intensity distribution across the imaged aperture it is reasonable to assume that the ablation depth is constant and the bottom of the ablated area is flat and relatively smooth [8]. The second pulse exposes and removes a cylinder-like volume with slightly smaller aperture diameter inside the first one. This leaves a two-step structure behind with a flat bottom where the 3rd pulse will remove a next cylinder-like volume with a further reduced aperture diameter. This procedure is repeated until the entire image is scanned. Figure 10 shows only five apertures to illustrate the principle; in practice there will be many more.

Figure 10. Series of apertures exposing the workpiece incoming pulses are represented by the apertures (above) the resulting ablation is shown below.
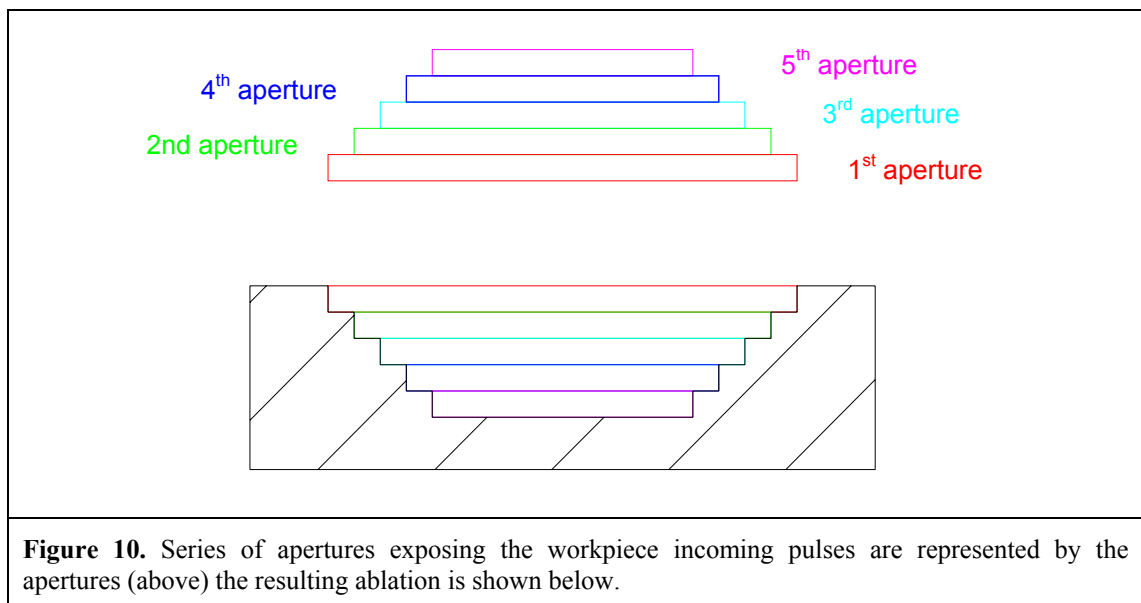
2.3.3.2   *The underlying ablation model*

The assumption on which these considerations are based, namely that each shot removes a cylinder with the diameter of the imaged aperture and the height according to the exposure fluence and ablation behaviour of the material, is actually not accurate. This simplification may be valid over most of the imaged aperture area, but certainly

fails at the edge of the image. Exposing a binary mask with zero transmission outside the aperture and transmission of one inside does not result in a perfect step function of the intensity profile after the mask as diffraction effects appear [9]. Nevertheless as these edge effects are relatively small, they are ignored for the moment (for a discussion of the edge effects cf. section 4.5). Moreover, if there are more than just a few superimposed apertures and the surface to be ablated moves beyond the depth of focus, other factors have to be taken into account when modelling ablation.

Despite of its shortcomings this simplified ablation model has been used as the basis for a program that simulates nozzle drilling. It takes into account the following input para-
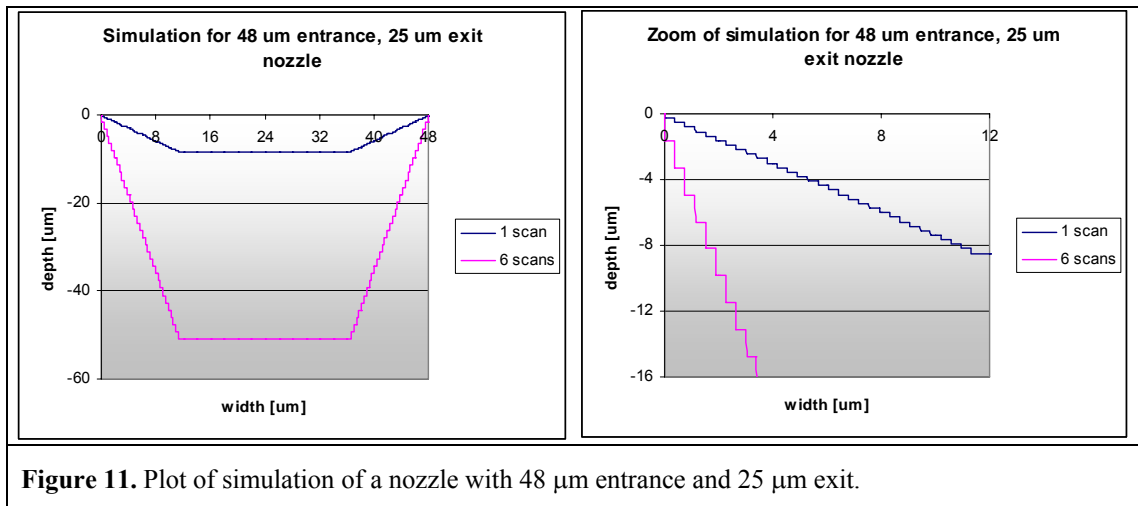
Figure 11. Plot of simulation of a nozzle with 48 μm entrance and 25 μm exit.

meters: the absorption coefficient and the threshold fluence of the material, the entrance and exit diameter of the required nozzle, the fluence and the number of apertures in the mask. The ablation depth per shot is determined by an ablation curve according to Beer's law. A plot generated by this program is shown in Figure 11 with simulation values taken from industrially used nozzle dimensions. The parameters were: absorption coefficient a = 8.8; threshold fluence, F_t = 63; process fluence F = 0.7 Jcm^{-2}; entrance diameter d_{en} = 48 μm; exit diameter d_{ex} = 25 μm; number of apertures n_a = 30. The simulation was done for 1 scan (blue line) and 6 scans (pink line). The simulation

predicts the same entrance and exit diameter and stepped side walls for both cases. The differences like the total depth and the greater step height with 6 scans are clearly visible.

2.3.3.3 Steps in the wall of the features

The graph on the right of Figure 11 gives a good visualization of the issue of the stepped side wall. For one scan one step is 0.38 μm wide and 0.274 μm deep; with 6 scans the width stays the same while the depth is multiplied by 6 resulting in 1.642 μm. Although the width of the steps is relatively small, it is probably not desirable to have steps in a nozzle where laminate flow of a liquid is required. As for this simulation a very basic model has been used, it is likely that experimental data will disagree with the findings above.
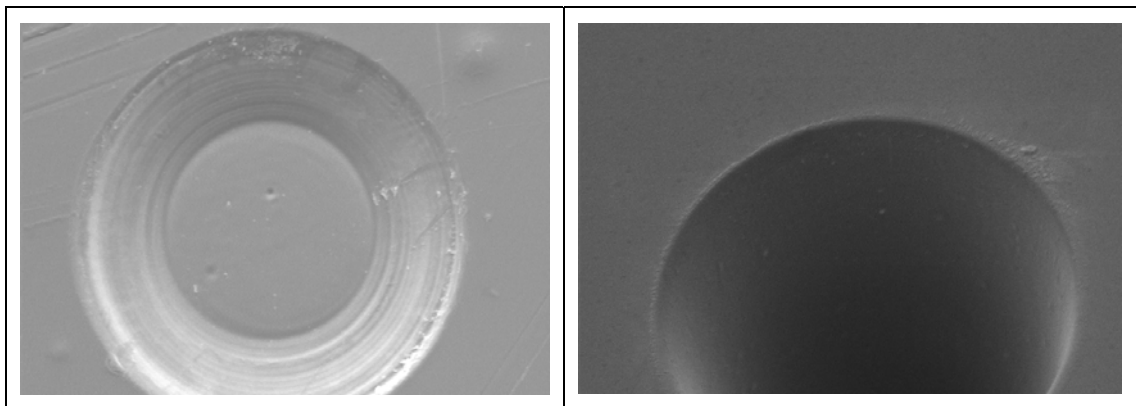
Figure 12. Experimental result for nozzles drilled into Polyimide. After 1 scan, steps can be seen on the side wall (left) but 6 scans produce a smooth side wall (right). The entrance diameter is 48 μm.

Indeed when drilling nozzles by SIS and choosing the same parameters as above, steps can be seen after 1 scan (Figure 12 left); after 6 scans, however, the ablated surface looks very smooth similar to the unirradiated area around the nozzle and no steps can be seen in the SEM picture (right). Repeated scans do obviously polish the surface; hence there is a significant disagreement with the simulation.

2.3.3.4 Scan direction

As the apertures in the mask are no longer identical, we do not have any more the choice in which axis of the mask we scan. It is, however, still possible to place several rows of apertures in the mask in order to increase efficiency.

Even though the scan axis is fixed, there are still two different scan directions, namely the positive and the negative direction of this axis. And as the apertures in the mask change in size, the process − and the result − is actually slightly different for the two directions.

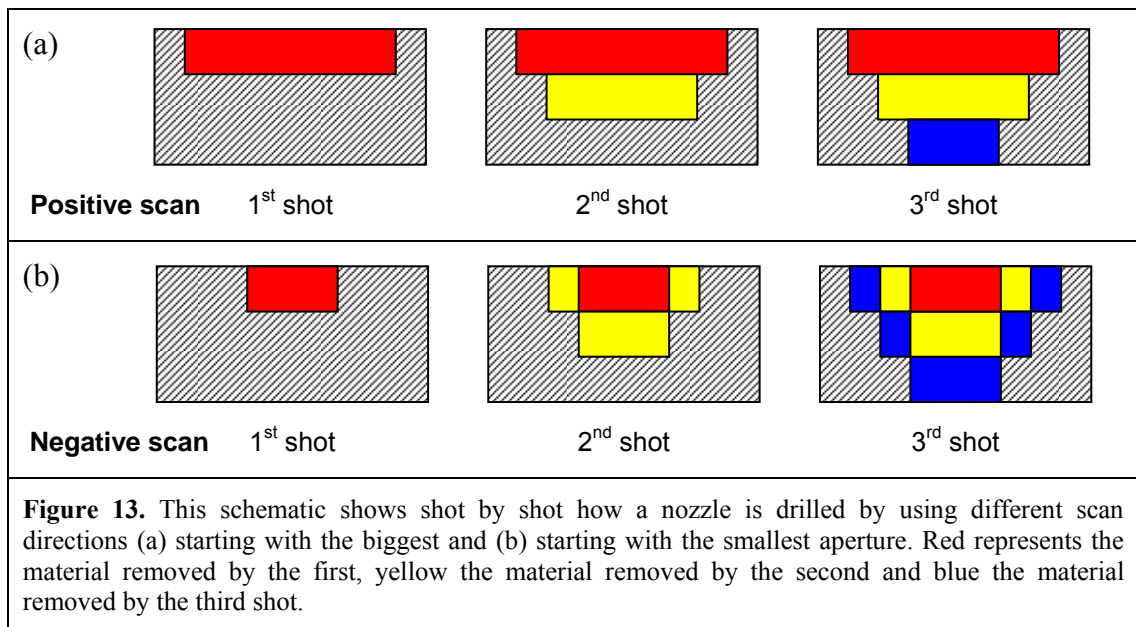The scan can start with the biggest aperture as shown in Figure 13(a) or with the smallest aperture in the mask in Figure 13(b). Hereafter the convention is that the 'positive' scan direction is from maximal transmission to minimal transmission, while the opposite scan direction is referred to as 'negative'. In other words in the positive scan the exposed area is decreasing while in the negative scan it is increasing.

Figure 13. This schematic shows shot by shot how a nozzle is drilled by using different scan directions (a) starting with the biggest and (b) starting with the smallest aperture. Red represents the material removed by the first, yellow the material removed by the second and blue the material removed by the third shot.

For the positive scan direction the first laser pulse defines the footprint of the feature and the top layer of the substrate into which the feature will be cut is removed with the first pulse. This can be an advantage over the negative scan direction as every imaged aperture has to nibble away a small portion of the top layer and it is well-known that the

very top layer of bulk material can behave differently from the rest of the material for various reasons [10]. A further significant difference between the scan directions is that for the positive scan every subsequent aperture imaged exposes a reasonably flat horizontal surface while for the negative scan every aperture but the first exposes a surface with an increasing degree of 3D topography. How this influences the result will be discussed in chapter 4.

If, however, multiple scans are used to reach the required depth, a change in the scan direction has no influence on the surface finish and hardly any on the overall quality of the nozzle (cf. Figure 14). This is good for the efficiency of nozzle drilling as it enables a bidirectional scan process avoiding empty moves.

Figure 14. Comparison of nozzles demonstrating that the drilling sequence of increasing or decreasing image size is unimportant when using multiple scans. The left and right nozzles are drilled by progressively decreasing and increasing image sizes respectively.
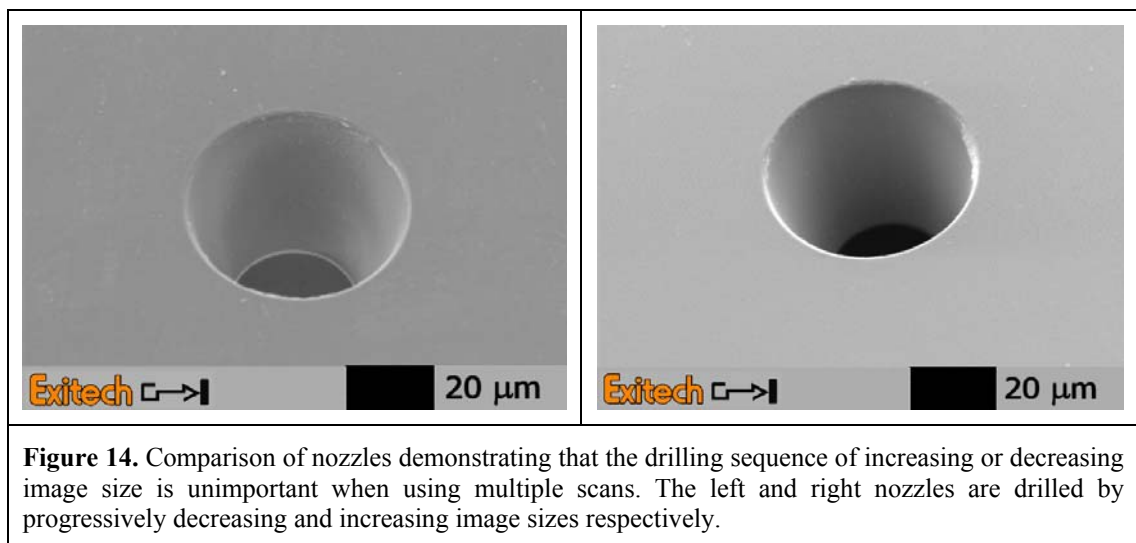
2.3.3.5   On the adjustment of the focus

Another issue when using SIS for thicker substrates is that even though the thickness of the substrate may exceed the depth of focus of the system (about 20 μm), it is not possible to adjust the focus during machining. This is due to the fact that each laser pulse ablates material from as many holes as there are apertures in the mask and the ablation takes place at different height levels simultaneously (cf. Figure 15). Correcting

the image plane of one aperture relative to the workpiece would consequently defocus the others.

Figure 15. Schematic representation of three of a series of holes being drilled by SIS. Each colour represents the material removed by one shot; red stands for the first shot that hits this part of the substrate, orange for the second, yellow for the third, etc. The workpiece moves towards the left, the image is static.
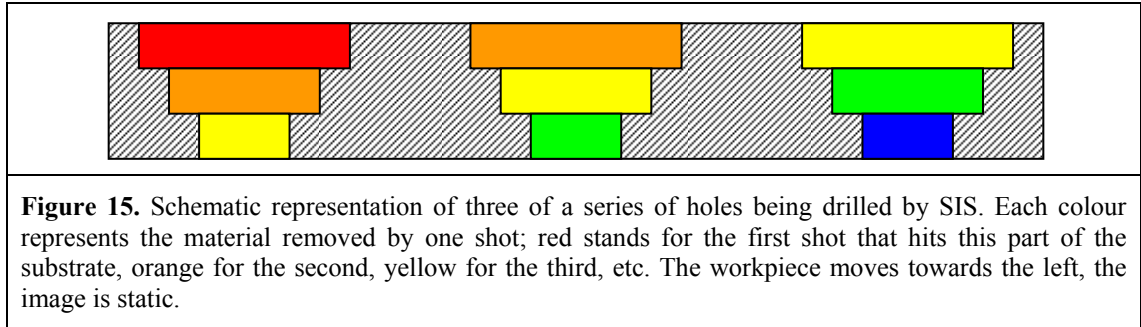
2.3.4 Machining of 3D micro-feature arrays

Having machined a tapered nozzle as a basic 3D feature there is no reason why the change of the aperture diameters could not follow a non-linear function or why the apertures could not have a shape other than a circle, thus enabling the creation of more complex 3D features. Indeed, with SIS it is possible to machine large areas of uniformly repeated 3D micro-features, and there are only few restrictions in the freedom of feature design. It is in the nature of mask imaging systems that there are restrictions regarding the angle of incidence and that machining cannot take place beneath the top surface. This means that freeform undercuts are not possible. Simple undercuts may be possible by employing specific optics and high fluence [11]. Although the freedom in feature design is thus restricted, there is still a great variety of possible geometries, and luckily most of the conventional micro-optical structures lay within reach of SIS.

2.3.4.1   SIS for 3D micro-structuring

The definition of the individual feature is the starting point of any SIS micro-structuring project [12]. Furthermore, for SIS it is also important how the features are arrayed. The ablation model used here is the same as the one introduced in subsection 2.3.3.2 and discussed in the context of nozzle drilling. It assumes that each laser pulse removes a certain volume of material given by the area defined by the mask aperture and the

ablation depth corresponding to the fluence of the pulse. Hence we can decompose the feature to be ablated into horizontal slices; the slice thickness corresponds to the ablation depth at a given energy density, the cross-sections define the apertures.

To describe the process of SIS for 3D micro-structuring from mask design to machining we consider the example of a simple structure. All the crucial steps are needed and are in principle the same as for geometrically more complex structures. The structure under consideration is a negative pyramid with a square footprint of 150 μm x 150 μm and consists of 3 steps each 200 nm in height while the width of the footprint is reduced by 50 μm each time. This individual feature is then arrayed on a 300 μm x 300 μm pitch in *x* and *y*. The material to be structured is Polycarbonate. First we need to slice the feature with a slice thickness which is achievable for the given material and a fluence range of 100 - 1000 mJcm^{-2}. For Polycarbonate this corresponds to a slice thickness range of 52 - 315 nm according to the ablation curve shown in chapter 4. The feature to produce has a step height of 200 nm, hence it is possible to cut it into 12, 6 or 3 slices with a thickness of 50 nm, 100 nm, or 200 nm respectively. The 50 nm ablation per shot requires a fluence below 100 mJcm^{-2} where the Beer's law function has a high gradient and starts to deviate significantly from experimental data. A slice thickness of 100 nm and 200 nm is equivalent to ~160 mJcm^{-2} and ~375 mJcm^{-2} respectively. Both are within the proposed fluence range of the micromachining system. For reasons of efficiency the higher fluence is chosen to give 1 shot per feature step.

In this case the slice thickness is 200 nm; hence the feature is cut into three slices. The footprints of the slices are 3 squares. These squares represent the imaged apertures to go in the mask scaled to account for possible image magnification. The same scaling factor applies to the array pitch by which these apertures are separated on the workpiece.

Assuming 5x demagnification, the mask will contain three square apertures with a side length of 0.75 mm, 0.5 mm and 0.25 mm on a 1.5 mm pitch.

For the general case we have:

$$x_c(n) = x_c(1) + (n-1) \cdot \frac{p}{m}$$

Equation 6.

where x_c is the x-co-ordinate of the centre of the n-th aperture at the mask, m the magnification factor of the optical system and p the array pitch on the workpiece.

Figure 16. Principle of SIS showing the first three shots with moving workpiece and static mask, the laser beam illuminates all apertures.
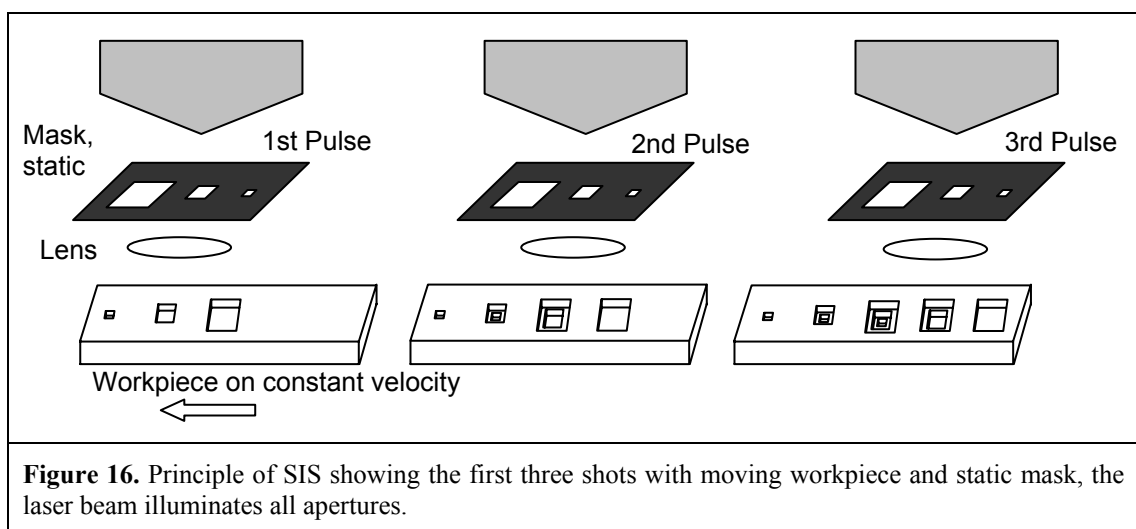
Figure 16 is a schematic of an imaging system with the mask in question. Four of the most critical components are shown: the incoming laser beam is represented by the wide arrow at the top, the mask with the three square apertures, the imaging lens and the workpiece. The laser beam, the mask and the lens are static relative to the optical axis while the workpiece is moving at a constant velocity and the laser pulse is triggered at the pitch of the sample array. The depth per pulse is exagerated to give a better idea of the technique. As mentioned before the laser beam illuminates the whole array of apertures. The first pulse therefore imprints the whole mask image onto the workpiece, in this simple case three squares increasing in size. After the workpiece has travelled one feature pitch, the second laser pulse imprints squares one and two into squares two and three respectively. As soon as the stage has travelled the pitch again, the third pulse

will finish off the first feature as square one is superimposed onto squares two and three. By continually moving the workpiece and firing the laser a new feature is completed by every laser pulse and a linear array of features is finally produced.

Even this simple example shows the core characteristics of SIS for 3D features, namely:

    (a) There are ramping effects at the start and the end of the scan.

    (b) Each laser pulse finishes one feature (except during the ramping phase).

    (c) The technique is highly efficient for feature arrays, but not necessarily for single features.

    (d) The pitch at the mask needs to be constant, accurate and stable over time.

    (e) The laser beam needs to have the same fluence over the whole object field.

    (f) There is binary intensity modulation of energy across the object.

The ramping effect (a) and measures to prevent damage of the workpiece will be discussed in chapter 3.

In this example there is only one array of apertures in the mask, but if there is enough energy in one laser pulse there is nothing to prevent us from copying the array perpendicularly to the scan direction. If this is done, not one feature is finished by each pulse (b), but as many as there are linear arrays illuminated by the laser beam; this obviously increases the machining efficiency (c).

Basically all the information about the feature is stored in a 2D array at the mask; the translation of the workpiece and the ablation depth adds the third dimension. Hence the feature can never be better than the mask (d). In practice an SIS pattern at the mask can be quite complex and contain many more than just a few apertures. The tolerances on the feature array demand a chrome-on-quartz mask patterned by lithography as used in the micro-electronic industry.

SIS for 3D structuring relies on a well homogenised beam profile at the object plane (e) as variation over the object field results in a variation of the ablated slice thickness and ultimately distorts the feature.

Due to the binary characteristic of the energy modulation (f) the ablated volume of each aperture has relatively steep edges making the individual imaged apertures clearly visible on the feature especially if the apertures change significantly in size.

The complexity of the features translates directly to the complexity of the mask design as it is essentially the mask that determines the shape. Thus we will now turn to discuss the design and alignment of the mask.
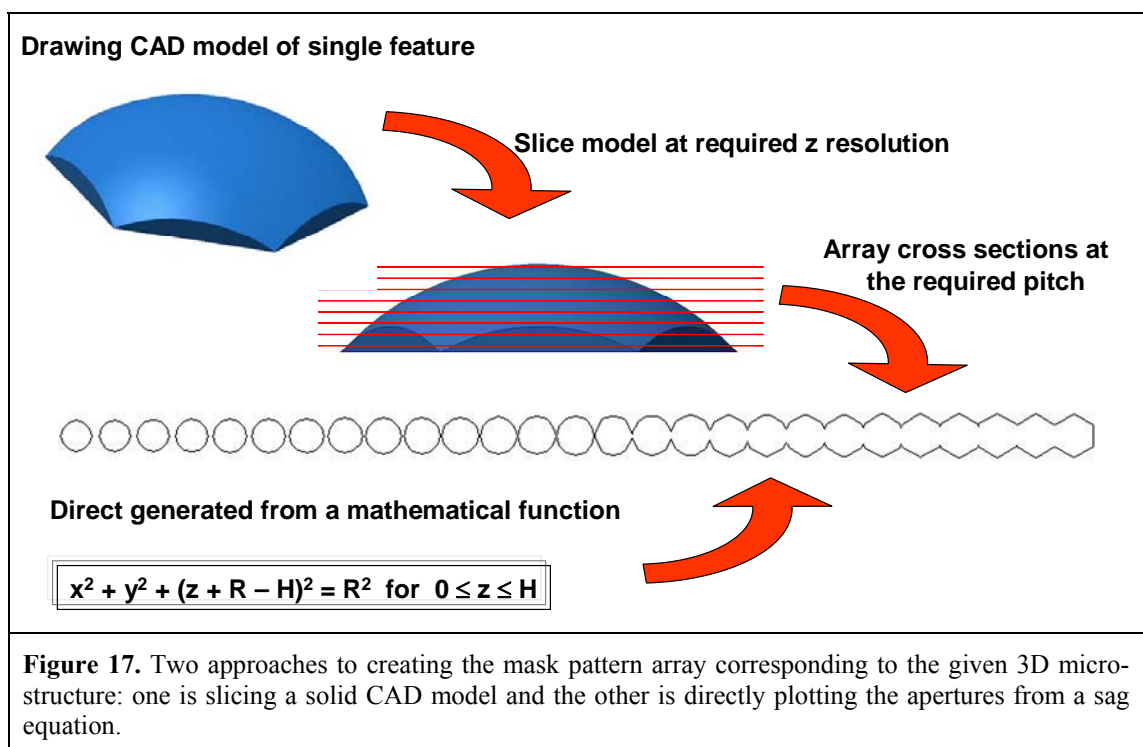
2.3.4.2   *Mask design*

As mentioned above most of the information about the shape of the feature is contained in the mask, which consists of arrays of sections of the feature at different z-levels [13]. The shape of the feature can be complex and may be described by a mathematical formula. The fact that the array for one feature consists often of more than a hundred apertures adds to the complexity of the mask design. Hence some sort of automation to draw the mask pattern is crucial for 3D structuring by SIS. The present subsection discusses the mask pattern design in more detail.

The cornerstone of the mask design is the ablation model introduced in subsection 2.3.3 and already applied to nozzle drilling. It assumes that every laser pulse removes material to a certain depth with the removed area defined by the imaged aperture. In contrast to stereo-lithography where the feature is built up, SIS removes the material around the feature in the case of a positive/convex structure or inside the feature in the case of a negative/concave structure thus carving the feature out of the bulk material. This means that it is not actually the feature which is sliced to define the apertures but

rather the material that has to be removed, which is simply the negative of the remaining structure.

Two main approaches to generating an array of apertures corresponding to a given 3D micro-feature are outlined here (see Figure 17). One employs a 3D CAD system to create a solid model of the material to be removed, slice it with the chosen slice thickness along the *z*-axis from top to bottom and then arrange the cross-sections at the right pitch in a linear array. The other approach creates the apertures directly from the mathematical function describing the feature shape by plotting the apertures corresponding to the *z*-levels of the slices and placing them in the right positions in the linear array.

The first approach using a CAD system is compelling. However, one major application for SIS 3D micro-structuring are micro-lens arrays, and often the demand is for lenses

Drawing CAD model of single feature

Slice model at required z resolution

Array cross sections at the required pitch

Direct generated from a mathematical function

$$x^2 + y^2 + (z + R - H)^2 = R^2 \ \text{ for } \ 0 \le z \le H$$

Figure 17. Two approaches to creating the mask pattern array corresponding to the given 3D micro-structure: one is slicing a solid CAD model and the other is directly plotting the apertures from a sag equation.

defined by a relatively complex sag equation. The author did not have a CAD package at his disposal which could automatically generate a solid model with a surface representing the sag equation, slice it up and array the slices in a linear array. Hence a

significant effort had to be made to enable the CAD system with add-on programs to do the job.

The second approach, where the aperture edges at the given z-levels are derived directly from the equation, reveals more of the principle behind the technique. To illustrate the steps necessary to create the aperture array corresponding to a given structure in this way, we consider the example of a bi-conical lens defined by the following equation:

$$z = \frac{c_x \cdot x^2}{1 + \sqrt{1 - (K_x + 1) \cdot c_x^2 \cdot x^2}} + \frac{c_y \cdot y^2}{1 + \sqrt{1 - (K_y + 1) \cdot c_y^2 \cdot y^2}} \qquad \textbf{Equation 7.}$$

As we are looking at horizontal sections of the lens, z equals some constant z_n for each of them. The section we want to draw is therefore a curve described by an equation in x and y. In many cases, this equation will be such that y is not a simple analytical function of x. But this does not really matter: the resolution of the imaging system is finite; we do not lose anything by approximating the curve by a short-edged polygon as long as the deviation from the curve is well below the resolution of the imaging system. A grid of 0.5 μm spacing is a good place to start.

After some transformations, we can rewrite the defining Equation 7 in such a way that y is a function of the independent variable x (assuming that z is constant):

$$y = \pm \sqrt{2 \cdot \frac{b}{c_y} - (K_y + 1) \cdot b^2} \qquad \textbf{Equation 8.}$$

with

$$b = z - \frac{c_x \cdot x^2}{1 + \sqrt{1 - (K_x + 1) \cdot c_x^2 \cdot x^2}} \qquad \textbf{Equation 9.}$$

Because the curve is symmetric with respect to both the x- and the y-axes, only the part of the curve in the first quadrant is needed. Hence the positive solution of the equation is used and afterwards mirrored at the x- and y-axes.

In order to determine the maximum and minimum x-values for the given z-level we need to solve Equation 7 for $y = 0$. We find that

$$x_{max} = \sqrt{2 \cdot \frac{z}{c_x} - (K_x + 1) \cdot z^2}$$

Equation 10.

The curves in x and y at the various z-levels form a contour plot of the feature. It has not yet been defined if the material is removed inside or outside the curves thus found, resulting in a concave or convex lens respectively, nor how the lens is packed in the array. To discuss this matter we make the assumption that the lenses are hexagonally arranged in a honeycomb-like structure. This means that bits of the lens need to be chopped off, and hence those sections that are partially outside the hexagon need to be trimmed accordingly. In this particular situation, we can distinguish the following cases:
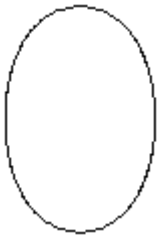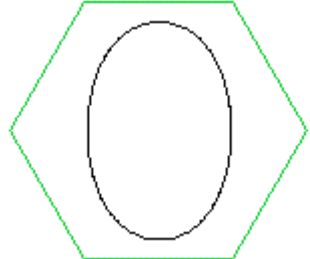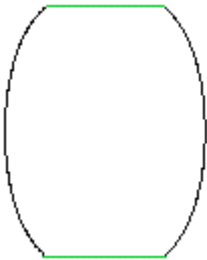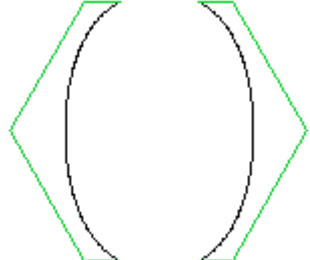
	Design for concave lenses	Design for convex lenses
Case 1: The lens cross-section does not intersect with the hexagon.		
Case2: The lens cross-section intersects with the horizontal edges of the hexagon.		
Case 3: The lens cross-section intersects with the sloping edges of the hexagon.		
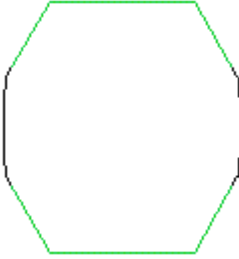
Table 5. Illustration of how the packaging affects the shape of the apertures.

For the sake of clarity, the lines belonging to the hexagon are drawn in green, whereas the lines belonging to the lens section are black.

Figure 18 shows the mask patterns for concave and convex lenses hexagonally packed; they each consist of eight copies of the corresponding aperture array.

Figure 18. Representation of mask pattern for concave (top) and convex (bottom) lenses hexagonally packed. These mask patterns will result in 8 rows of lenses after one scan.
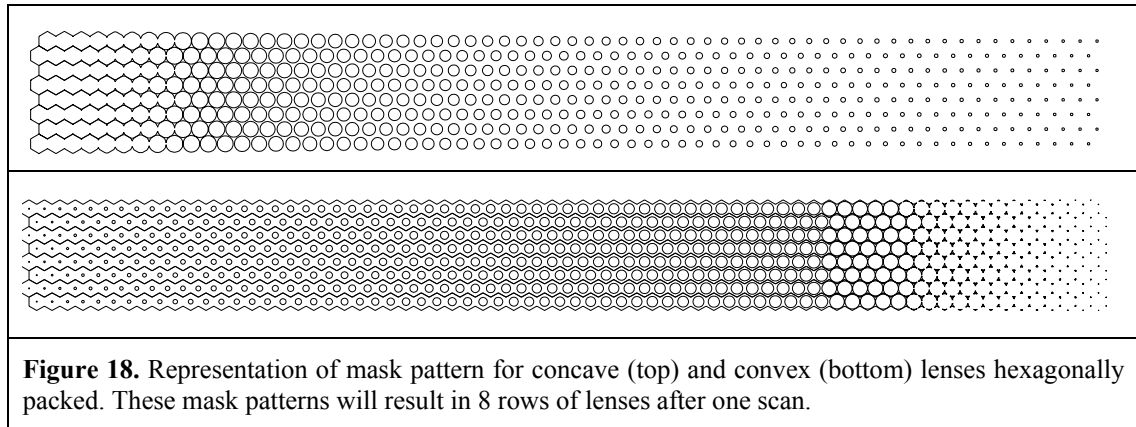
After this discussion it should be clear that it is possible to automate the drawing of the mask pattern array for a wide variety of features and types of packaging.

2.3.4.3   *Installing and aligning the mask*

As explained above a chrome-on-quartz mask with an appropriately designed SIS pattern is needed to be able to machine high quality SIS features. The mask, and especially the relevant pattern in the mask, has to be clean and free from any debris or residue since this would affect the transmittance of the fused silica in places and thus distort the feature to be machined.

The pulse energy for direct laser machining can be magnitudes higher than in photolithography, nevertheless the same type of binary mask is used. Hence some additional precautions need to be taken: for instance the mask is to be used upside-down, i.e. the fused silica and chrome side has to face the incoming laser beam. It is advisable to mask off as much as possible of the beam that is not actually illuminating the object pattern as the chrome on the mask is highly reflective and the reflected energy can in certain circumstances cause damage to the mask.

The mask needs not only to be positioned so that the laser beam can illuminate the whole aperture array, but also rotated to run exactly parallel to the image scan direction. To do this is particularly critical for the SIS process since the first and the last aperture are superimposed on the workpiece and must end up in exactly the right position on top of each other. Alternatively, the angle of the mask relative to the workpiece stages could be calculated and compensated for in the stage movement, but for accuracy reasons ideally only one axis moves during the scanning process. If there are only manual mask stages on the tool, the alignment of the mask has to happen with the mask object that is later used to machine the micro-structure. To get it right, information about the micro-structure to be machined is needed, particularly the position of the last aperture relative to the first one, e.g. if they are concentric or not. Some mask patterns are simpler to align than others: an array corresponding to a square packed convex spherical lens array is easier than one corresponding to an eccentric negative cone structure for instance. This is because the lens pattern has a rectangular frame while the cone pattern has circular apertures off the centre line. The procedure remains the same, though, as the mask pattern is always designed in such a way that the first and the last aperture are in a straight line. This means that by moving the workpiece only it is possible to adjust the
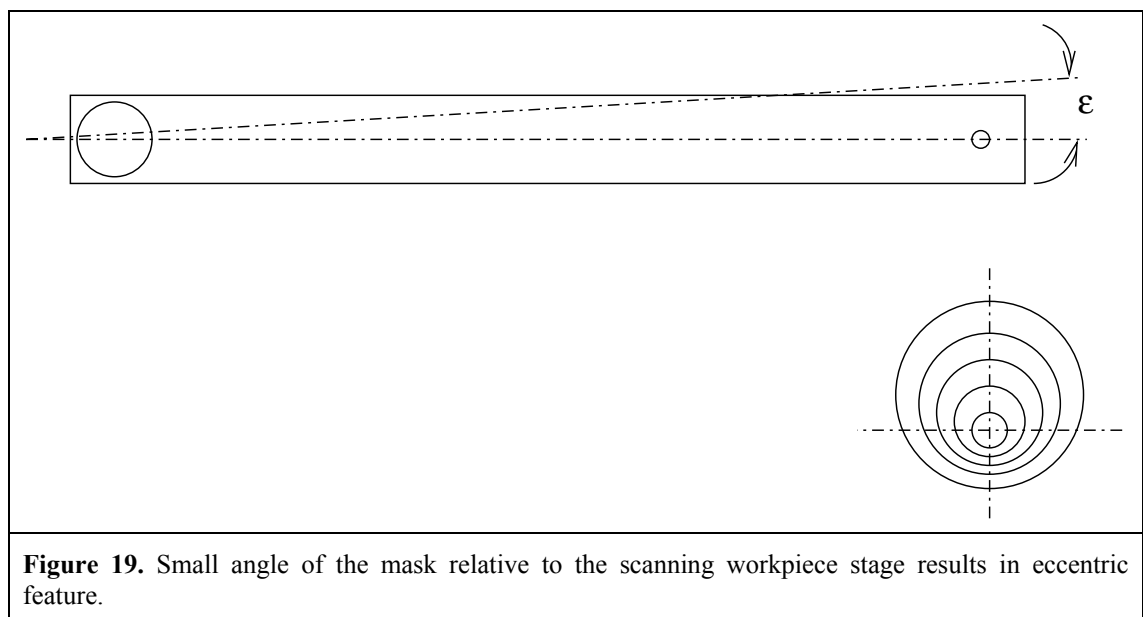

Figure 19. Small angle of the mask relative to the scanning workpiece stage results in eccentric feature.

rotation of the mask so that the first and the last aperture in the image are positioned correctly relative to each other as illustrated by Figure 19.

Angular misalignment between the mask object and the scanning workpiece axis will result in features where the offset is perpendicular to the scan direction. The rotation of the mask determines to which side they are offset, but it will be to the opposite side from the mask because of the inversion by the projection lens.

An offset parallel to the scan direction happens if the stage travel between the trigger pulses for the laser does not exactly match the pitch of the apertures in the image (cf. Figure 20). Every error in the travel distance is multiplied by the number of apertures, so again high resolution stages are needed and multiple pitch measurements over the whole image on the machine itself are necessary to give good results.

Figure 20. If the pitch given by the mask does not match the laser firing distance, an offset parallel to the scan direction occurs.
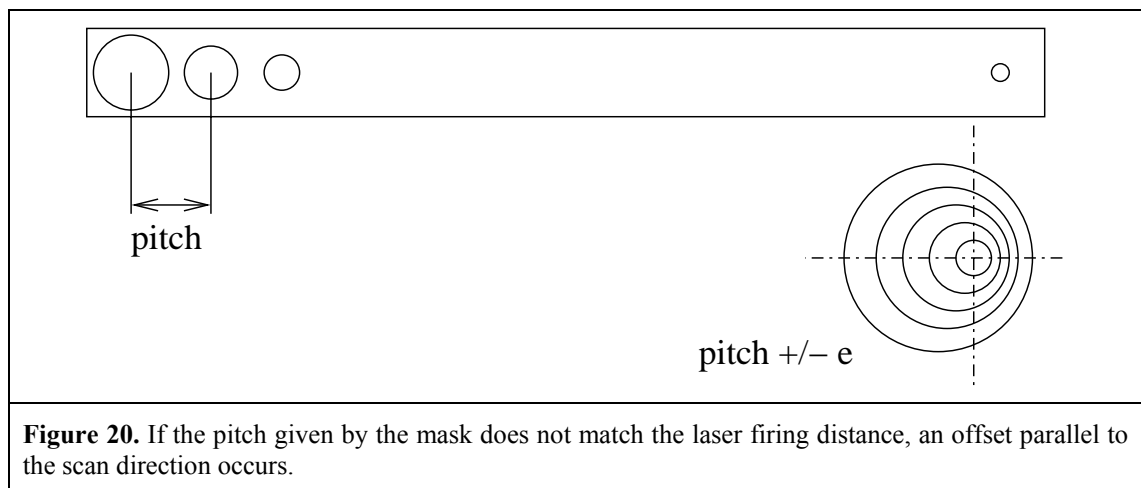
The fact that the mask needs to be aligned parallel to the scanning axis of the workpiece and that the pitch has to be matched exactly to produce well centred features implies that it is possible to machine several different feature geometries with the same mask. For instance a mask that is designed to machine a centred four-sided pyramid can also be used to machine any pyramid with its tip anywhere inside its footprint as Figure 21 illustrates. Here A is the designed feature, B one that can be achieved by slightly reducing the pitch, C by rotating the mask and D by a combination of both.

Figure 21. Sketch A represents the designed feature, B one that can be achieved by slightly reducing the pitch, C by rotating the mask and D by a combination of both.
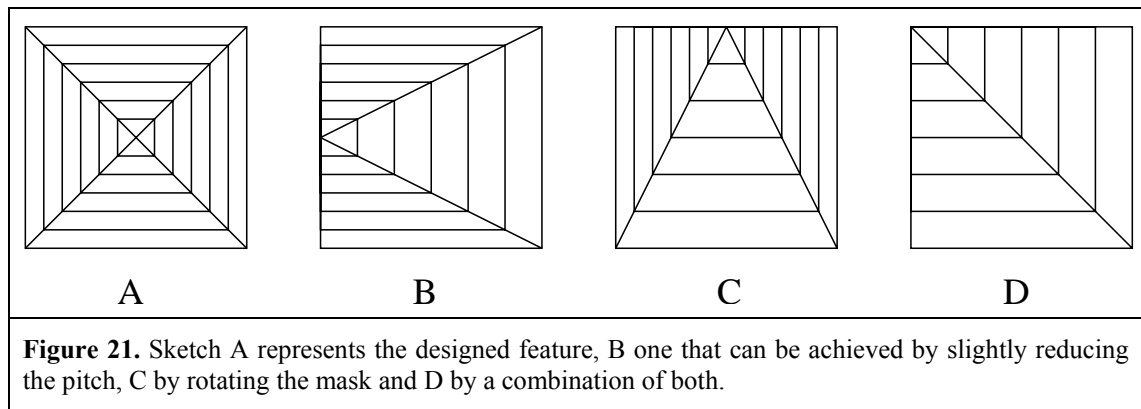
1 C. Abbott, R. Allott, B. Bann, K. Boehlen, M. Gower, P. Rumsby, I. Stassen Boehlen, N. Sykes, SPIE Vol. 4760, 281 (2001)

2. D. Lidzey, M. Voigt, C. Giebeler, A. Buckley, J. Wright, K. Boehlen, J. Fieret, R. Allott, Organic Elec. 6, 221 (2005)

3. J.E. Andrew, P.E. Dyer, R.D. Greenough, P.H. Key, Appl. Phys. Lett. 43(11), 1076 (1983)

4. X. Zhang, S.S. Chu, J.R. Ho, C.P. Grigoropoulos, Appl. Phys. A 64, 545 (1997)

5. W. Pfleging, A. Ludwig, K. Seemann, R. Preu, H. Maeckel, S.W. Glunz, Appl Surf. Sci. 154–155, 633 (2000)

6. S. Lazare, J. Lopez, F. Weisbuch, Appl. Phys. A 69 [Suppl.], S1–S6 (1999)

7. Patent: WO9726137, Method of and apparatus for forming nozzles, Xaar ltd (GB)

8. R Srinivasan, Science, 234, Issue 4776, 559, Oct 1986

9. PE. Dyer ; CD. Walton, Appl. Phys. A, 79, 721 (2003)

10. W. Pfleging, A. Ludwig, K. Seemann, R. Preu, H. Mackel, S.W. Glunz, Appl. Surf. Sci. 154–155, 633 (2000)

11. C. Paterson, A.S. Holmes, R.W. Smith, Appl. Phys. 86, 11 (1999)

12. K. Boehlen, I. Stassen Boehlen, SPIE Vol. 5339 (2004)

13. K. Boehlen, I. Stassen Boehlen, R. Allott, SPIE Vol. 5720 (2005)
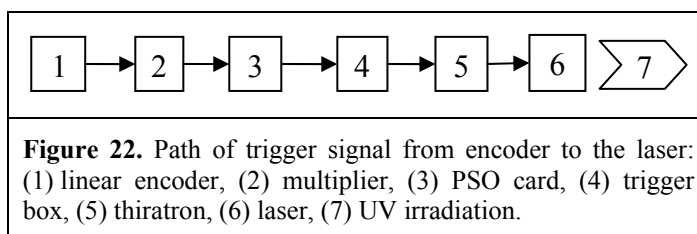
3   The potential of SIS

3.1   Comparison of SIS and Step & Repeat

A common method for laser patterning an area with repeating micro-structures using mask imaging is Step & Repeat as described in subsection 1.2.3. The present section explores the advantages and disadvantages of SIS over this classic technique.

The Step & Repeat technique is mainly suitable for the case where the mask contains an array of identical apertures (e.g. for a hole drilling application) and hence the length of one "step" is equal to the length of the image. Therefore we focus in this section on this particular case when comparing the two methods. Subsection 3.2.2 will then give an impression of the great variety of 3D micro-structures that can be created by SIS using a mask containing an array of different apertures. These structures could also be machined using Step & Repeat, but as the length of one "step" is then reduced to the feature pitch, processing times for Step & Repeat are a multiple of the processing times for SIS.

3.1.1   Tighter hardware specs

With Step & Repeat the stages are stationary during the burst, and as long as they are settled, the feature quality depends on the imaging quality only. The assumption is that the imaging quality is equal to the lens specification of e.g. ±0.5 μm on a 25 μm hole. The feature quality is basically independent of the stage accuracy as long as the stages do not move or oscillate during exposure; in principle the stages do not even need to be numerically controlled.
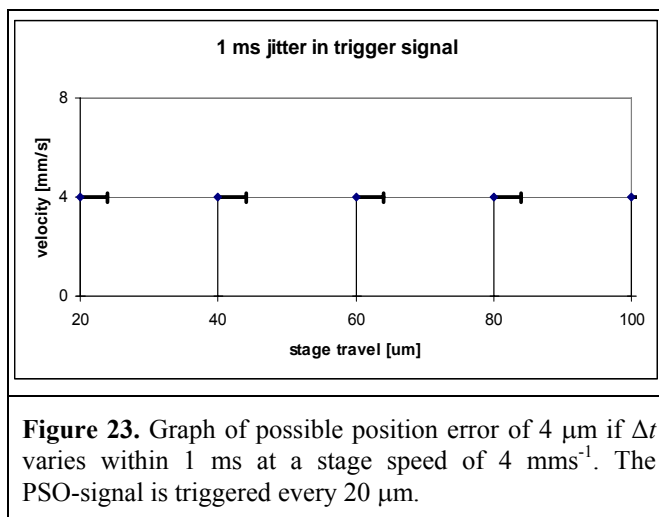

Figure 22. Path of trigger signal from encoder to the laser: (1) linear encoder, (2) multiplier, (3) PSO card, (4) trigger box, (5) thiratron, (6) laser, (7) UV irradiation.

This is different for SIS as the firing of the laser needs to be synchronised with the move-ment of the stages. The trigger signal from the stage encoders to laser has to go

through a chain of elements and delay time influences the pattern quality. Figure 22 shows a schematic of the signal path from the main stage encoders to the laser. An optical sensor reads the grating of an etched glass ruler (1). The signal is then multiplied to enhance the resolution (2). The multiplied signal is fed into the PSO card (Aerotech) (3), where it is processed to give an output according to the chosen firing distance from pulse to pulse. To raise the voltage level the signal is amplified in the trigger box (4) before reaching the thyratron (5), which switches the high voltage supply to excite the KrF gas mixture in the laser cavity (6) and finally generates UV irradiation (7). For SIS it is crucial that the time delay Δt between (1) and (7) is constant and as short as possible. Fluctuation in Δt results directly in a mismatch of the images, which should exactly overlap. Figure 23 shows that the possible position error of superimposing images from pulse to pulse can be up to 4 μm when Δt varies by 1 ms at a stage speed of 4 mms^{-1}. This is obviously not acceptable as the target is likely to be around 0.5 μm position accuracy and the stages usually move much faster. For a stage velocity of 50 mms^{-1} the maximum jitter in the trigger signal between the stages and the laser must be < 10 μs to stay within the target of a 0.5 μm position error. All these calculations assume a perfectly constant velocity. This is unlikely, but the resulting error can easily be taken into account as a relative error (in %). If Δt is significant but constant, the alignment of new structures to existing ones is more difficult but can be compensated for with an offset.

Figure 23. Graph of possible position error of 4 μm if Δt varies within 1 ms at a stage speed of 4 mms^{-1}. The PSO-signal is triggered every 20 μm.

Keeping the jitter in Δt and Δt itself as small as possible is only one demand on the hardware for SIS. SIS also requires higher position accuracy of the translation stages than Step & Repeat. This is due to the fact that in most cases one laser pulse provides less than the amount of illumination necessary to completely ablate a structure in a substrate. Consequently the substrate and/or image are then translated by a distance less than the image field to provide an additional level of illumination. This relative translation between the substrate and the image continues until the structures are fully ablated. This procedure introduces two further sources of errors that influence feature quality.

The first is absolute stage accuracy. If for instance 10 shots per area are required, this means that one position on the workpiece is built up from 10 different apertures in the image; hence the edge of an individual feature can be blurred by the position error.

Second, the firing distance needs to match the required multiple of the aperture pitch in the image. Otherwise any offset will accumulate over the image scan length (cf. subsection 2.3.4.3). This puts high demand on the resolution of the encoder signal as flexibility in the pitch width is essential.

To summarise: employing SIS introduces three sources of possible errors on the individual feature. The first is the jitter in the signal path from the encoder to the laser firing; the second is the absolute position accuracy of the stages; and the third is the resolution of the encoder signal. These three points together demand high quality hardware which has only become affordable in recent years.

3.1.2 Higher quality and consistency

The impact of SIS on quality and consistency is best explained using the simple example of producing a filter with thousands of holes in a 5 µm thick polymer coating. It is reasonable to assume that the polymer film is penetrated with 16 shots per area and
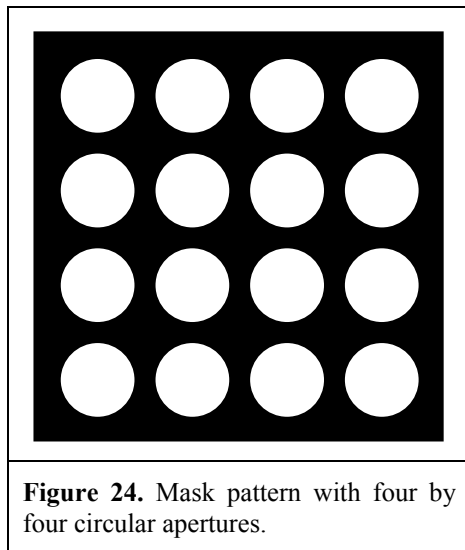
Figure 24. Mask pattern with four by four circular apertures.

that 16 apertures can be fitted into the area illuminated by a laser beam carrying enough energy for the required ablation rate. For simplicity the mask pattern will consist of a four by four matrix of circular apertures. Traditionally a simple Step & Repeat approach would be employed where the mask is imaged onto the workpiece and a burst of 16 shots fired to drill all 16 holes simultaneously, then the stages are moved by the image pitch and the next set of holes is ablated. As discussed in subsection 3.1.4 there is a considerable waste of time for each move between positions. Furthermore, a static drilling method has an impact on the quality and consistency of the holes. As hole drilling is a well studied application, it is known that a hole drilled with a burst of pulses using the same aperture at the mask, the same portion of the beam and the same position in the pressure and debris zone of the image can vary in depth, shape and wall angle from a hole drilled simultaneously in a different part of the image [1]. Any variation of a certain percentage over the illuminated area of the beam, the mask or the pressure and debris zone on the workpiece surface will show up as a variation of the holes drilled. This becomes obvious if we assume that one of the apertures at the mask is blocked; then static drilling will produce only 15 holes. In practice the variation within the feature array is often more critical than the deviation from the specification as long as the deviation is the same for all the features. This indicates that a satisfactory solution could be to average the conditions for each hole through the drilling process even if the conditions are not ideal.

By employing a dynamic drilling process like SIS a lot of averaging can be done, which results in more consistent holes. In the following it is explained why the issues

discussed above are far less critical if SIS is employed. To get the best averaging effect the strategy of SIS is to drill an individual hole with all 16 apertures and not just with one. This automatically uses 16 different parts of the laser beam and image zone. In other words every hole on the workpiece is scanned by the entire image, hence the sum of the energy is the same for each hole as long as the energy is constant from pulse to pulse. This is achieved by scanning the image in one axis over the workpiece while firing the laser at the pulse repetition rate corresponding to the hole separation, stepping in the axis perpendicular to the scan direction by one hole pitch and repeating this scan and step as many times as needed to cover a given area.
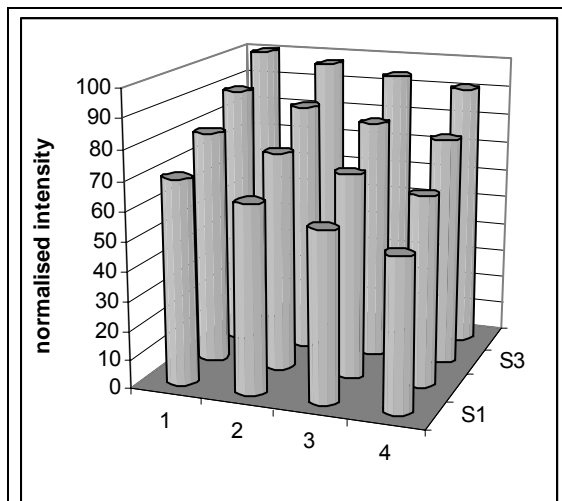

Figure 25. Illustration of a normalised intensity profile after a 4 x 4 hole mask illuminated with a strong gradient in the laser beam.

Using an illustrative example of a strong gradient in the intensity of the laser beam illuminating the mask pattern the advantages of SIS can be further discussed. Figure 25 shows a possible normalised intensity profile after the mask. As the ablation depth per shot is directly dependent on the applied energy density, statically drilling holes with this configuration would result in holes of different depth. Coming back to the practical example of machining a filter, it is likely that with static drilling the strong intensity gradient in the beam would result in only drilling through half of the holes even though the average fluence is high enough to theoretically drill through the holes. Employing SIS on the other hand will drill through all the holes as they are all exposed to the same total amount of energy. It is important to note that not only the intensity variation in the beam but also a non-uniform transmission of the mask, differences in absorption of the incoming beam caused by uneven debris distribution within the image and rising

pressure gradient from the edge to the centre of the image are averaged out for each hole when the image is synchronously scanned.

3.1.3 Frame of partially machined features

When scanning every hole at the workpiece with every aperture at the mask a frame of unfinished holes surrounds the finished ones. They may only be virtual as masking them off (explained later in this subsection) can protect the workpiece; nevertheless a loss in efficiency is unavoidable. In the case of drilling a matrix of 4 x 4 holes without masking off a frame three holes wide will surround the finished holes; the surrounding holes differ in depth depending on their position. Figure 26 shows the minimum area to be scanned to produce a 4 x 4 hole matrix if every hole position sees every aperture at the mask. The numbers in the top left han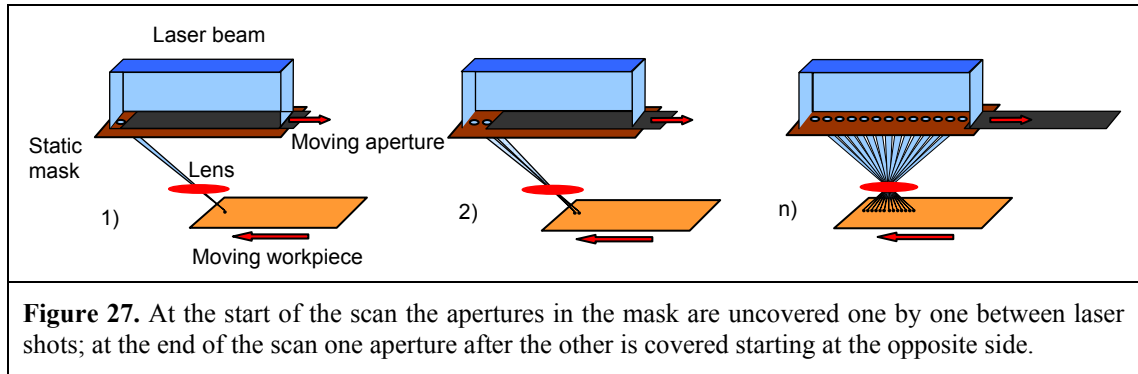d corner stand for the number of shots per area. This is an extreme example which makes it clear that SIS is not efficient for machining

Figure 26. Minimum number of holes to produce a 4 x 4 hole matrix with SIS.
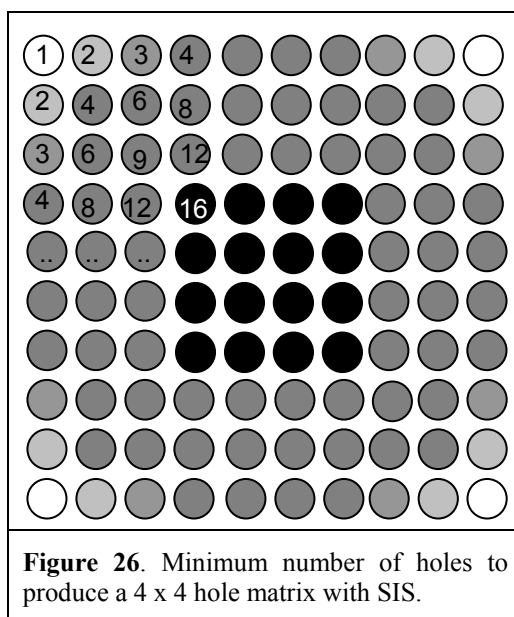
an area only a few times the image size. Nevertheless SIS exceeds a Step & Repeat process in efficiency very quickly as soon as the process area is a multiple of the image size. For one dimensional arrays an area of only two or three times the image size is needed to make SIS more efficient than Step & Repeat (cf. Subsection 3.1.4).

In order to avoid additional holes around the actual process area there are two ways of masking these holes off. One can either use a static contact mask on the workpiece or dynamically move the mask or a shutter to progressively reduce the numbers of apertures being illuminated by the laser beam. The contact mask is easily applied but needs to be accurately aligned and precisely cut to the size of the required process area.

The option to either move the mask synchronously in and out of the beam or use a shutter to cover and uncover the apertures in the mask requires a mask or shutter stage synchronised with the workpiece stages. Figure 27 shows the principle of a synchronised moving shutter to eliminate unwanted holes at the beginning and the end

Figure 27. At the start of the scan the apertures in the mask are uncovered one by one between laser shots; at the end of the scan one aperture after the other is covered starting at the opposite side.

of a scan of a one dimensional array. At the start of the scan the apertures in the mask are uncovered one by one between laser shots; at the end of the scan one aperture after the other is covered starting at the opposite side of the array, thus leaving only completely drilled holes in a well defined area. Using precision stages this technique even allows drilling only part of a hole at the edge of the process area.

3.1.4 Efficiency

Figure 28. Graph of laser on/off and stage velocity for Step & Repeat top and SIS bottom.
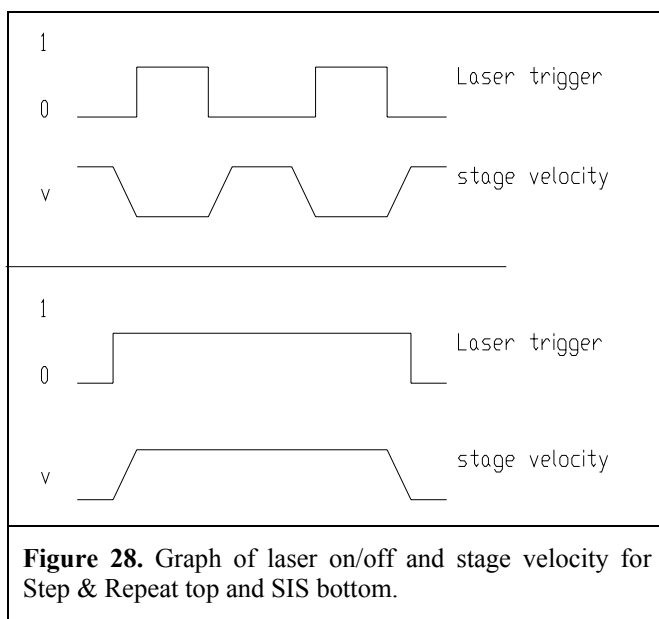
The question arises why to invest in expensive hardware and to put up with a frame of partially machined features if it can all be done with the less demanding Step & Repeat method. The answer is that there is a significant difference in process speed. Figure 28 shows a qualitative graph of

laser on/off and stage velocity for Step & Repeat (top) and SIS (bottom). This illustrates

that for Step & Repeat the laser has to stop while the stages are on the move from position to position regardless how fast this move might be. This is in contrast to SIS where the laser starts firing as soon as the stages accelerate and only stops at the end of the scan. No calculations are needed to recognise that with SIS more laser pulses expose the workpiece in the same time interval. It is also obvious that the process is less efficient if the laser and the stages have to go through a sequence of on/offs instead of constantly firing and running respectively (not to mention that the energy of the first pulse of a burst is usually higher than the rest, which may affect the process quality).

As explained in subsection 3.1.2, for a multi shot per area process SIS has some losses on either side of each scan as the total amount of shots is accumulated through a full or part scan of the image (the number of shots ramps up either side of a scan). Hence SIS is only more efficient if a process unit is a few times the image size. For many applications, e.g. displays and photovoltaics, the process area is usually large and the image size only a small fraction of it [2]. This leaves SIS as the preferred technique thanks to higher process speed.

In order to be able to determine which of the two techniques – Step & Repeat or SIS – is more efficient for a given application, we will now proceed to calculate the average machining time per feature for both options (still focussing on the case where all the apertures in the mask are identical, i.e. the "step" for Step & Repeat is equal to the length of the image).

The following parameters come into the equation:

R_{max} maximum laser pulse repetition rate

a stage acceleration

v_{max} maximum stage velocity

n_f number of features per row

n_{ax} number of apertures in each row (parallel to the scan direction) on the mask

n_{ay} number of apertures in each column (perpendicular to the scan direction) on the mask

n_s number of shots per area required

p feature pitch

For the sake of simplicity, these (not unreasonable) assumptions are made:

1) The same mask is used for both techniques. In practice different criteria determine the layout of the mask: for Step & Repeat n_{ax} is chosen to be a factor of n_f (as great as possible), while for SIS the choice of n_{ax} is dominated by the aim to minimise the number of scans required, which is given by n_s / n_{ax}. But it is well possible that the same mask meets both criteria.

2) The stages accelerate and decelerate at the constant rate $\pm a$; the maximum stage velocity is reached during each "step" of Step & Repeat as well as during each "scan" of SIS (for $a = 1$ ms^{-2}, a velocity of $v_{max} = 100$ mms^{-1} is reached after $x_{ramp} = v_{max}^2 / 2a = 5$ mm).

3) For SIS the firing distance equals the feature pitch.

4) For SIS the limiting factor for the stage velocity is the laser pulse repetition rate rather than the stage specifications, i.e. $v \leq R_{max} \cdot p$ (a pulse repetition rate R_{max} of 200 Hz and a pitch p of 500 μm limits the velocity to 100 mms^{-1}; usually the pitch is rather smaller than this).

5) For SIS laser triggering is linked to the stage position, enabling machining during the ramp time.

Average machining time per feature for Step & Repeat

The "step" distance is the length of the image, i.e. $n_{ax} \cdot p$. Over a distance $x_{ramp} = v_{max}^2 /$ $2a$ the stages accelerate until they reach the maximum stage velocity v_{max}; this takes $t_{ramp} = v_{max} / a$. The same distance and time is needed at the end of each step for deceleration. Hence the time needed for one "step" is given by:

$$2 \cdot t_{ramp} + \frac{n_{ax} \cdot p - 2 \cdot x_{ramp}}{v_{max}} = \frac{v_{max}}{a} + \frac{n_{ax} \cdot p}{v_{max}} \qquad \textbf{Equation 11.}$$

Thus we find:

Total "step" time per scan:
$$\left(\frac{n_f}{n_{ax}} - 1\right) \cdot \left(\frac{v_{max}}{a} + \frac{n_{ax} \cdot p}{v_{max}}\right) \qquad \textbf{Equation 12.}$$

Total drill time per scan:
$$\frac{n_f}{n_{ax}} \cdot n_s \cdot \frac{1}{R_{max}} \qquad \textbf{Equation 13.}$$

The average machining time per feature is the sum of the total "step" time and the total drill time per scan divided by the number of features produced: $n_{ay} \cdot n_f$.

$$\left(\left(\frac{n_f}{n_{ax}} - 1\right) \cdot \left(\frac{v_{max}}{a} + \frac{n_{ax} \cdot p}{v_{max}}\right) + \frac{n_f}{n_{ax}} \cdot n_s \cdot \frac{1}{R_{max}}\right) \cdot \frac{1}{n_{ay} \cdot n_f} \qquad \textbf{Equation 14.}$$

Average machining time per feature for SIS

Due to the ramping effect at the beginning and the end of each scan (see subsection 3.1.2), there are $n_f + n_{ax} - 1$ imaging positions for each scan. Hence the total distance travelled for one scan equals $d = (n_f + n_{ax} - 2) \cdot p$. As above, we have to take into account the time for acceleration and deceleration; only this time the maximum velocity is given by $R_{max} \cdot p$. Hence the total time for one scan is given by:

$$\frac{R_{max} \cdot p}{a} + \frac{(n_f + n_{ax} - 2)}{R_{max}} \qquad \textbf{Equation 15.}$$

With SIS, several scans are needed if the number of shots per area required exceeds the number of apertures in the mask (cf. Section 3.2). Hence the total time per scan needs to

be multiplied by the number of scans and then divided by the number of features completed to obtain the average machining time per feature:

$$\left(\frac{R_{max} \cdot p}{a} + \frac{(n_f + n_{ax} - 2)}{R_{max}} \right) \cdot \frac{n_s}{n_{ax}} \cdot \frac{1}{n_{ay} \cdot n_f}$$
Equation 16.

The following graphs show the differences in machining time for a typical example of a drilling application where all the apertures in the mask are identical:
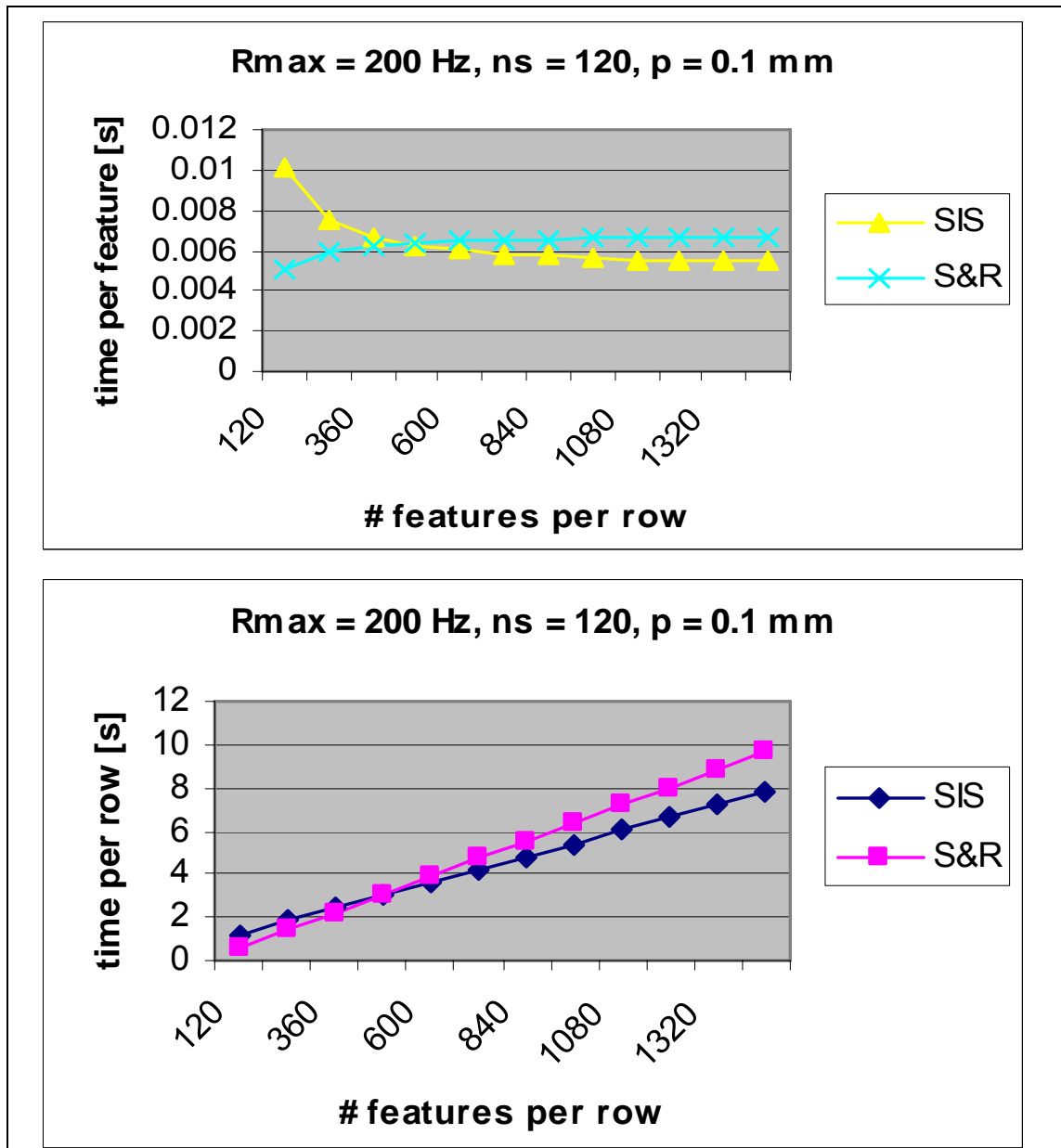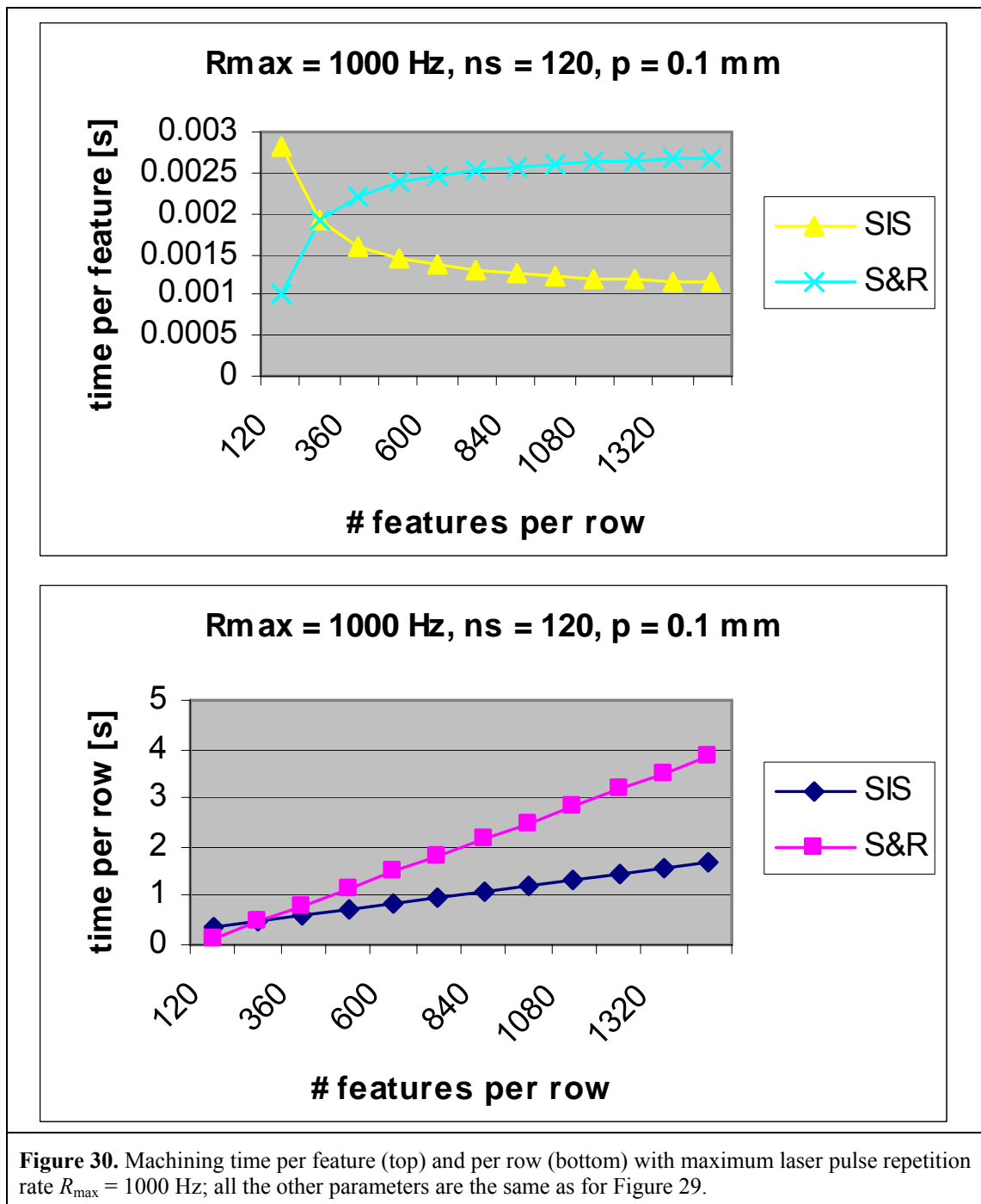

Figure 29. Machining time per feature (top) and per row (bottom) with maximum laser pulse repetition rate R_{max} = 200 Hz, stage acceleration a = 1 ms^{-2}, maximum stage velocity v_{max} = 100 mms^{-1}, number of apertures in x n_{ax} = 120, number of apertures in y n_{ay} = 1, number of shots per area n_s = 120, feature pitch p = 100 µm in a drilling application with identical mask apertures.

Note that the machining time per feature is considerably smaller for Step & Repeat when the number of features per row is the same as the number of apertures on the mask for the obvious reason that no "step", i.e. no stage movement, is required. SIS does, however, become more efficient as soon as the number of features per row is three times the number of apertures on the mask. The difference in machining time per feature converges very quickly to a constant value as the number of features per row increases.

Figure 30. Machining time per feature (top) and per row (bottom) with maximum laser pulse repetition rate R_{max} = 1000 Hz; all the other parameters are the same as for Figure 29.

The effect of an increase in the laser pulse repetition rate is interesting (see Figure 30): the impact on the machining time for Step & Repeat is not nearly as dramatic as for SIS, where the laser pulse repetition is the limiting factor for the stage velocity. Hence if the repetition rate is increased, the productivity of SIS goes up significantly.

So far the assumption has been that the "step" distance for Step & Repeat is equal to the length of the image, i.e. each feature on the workpiece is machined using one aperture only. If 3D features were to be machined by Step & Repeat using an array of different apertures, the same extra imaging positions as for SIS would be required and the step distance would be reduced to the feature pitch with devastating impact on the machining time. To give only one example: with the same parameters as for Figure 29, a row of 1200 features would take 32.96 s; this corresponds to a machining time per feature of 0.027 s. Hence it would take just about 11 hours to cover an area of 120 mm x 120 mm with features on a 100 μm pitch, while the same can be done in around 2.2 hours when machining on the flight.

3.1.5 Creating a controlled taper

There are many applications of laser drilled nozzles [3,4,5] but what we have in mind here are inkjet printer nozzles. It is indeed possible to create a controlled taper with a mask containing an array of identical apertures, i.e. suitable for Step & Repeat. However, this requires a special technique. One possibility is 'wobbling' of the image; this can be done by mask or stage movement or by positioning rotating plates or PZT oscillating mirrors in the beam line between mask and image. The hole apertures (d times imaging magnification) at the mask are all of the same diameter, which is determined by the following equations:

$$2 \cdot d = in + ou \qquad \text{Equation 17.}$$

$$in = d + x \qquad \text{Equation 18.}$$

where *in* = input diameter , *ou* = output diameter, *d* = diameter of imaged aperture, *x* = circle guide line diameter. However, wobbling of the image to create a high taper angle leads to a significant increase in the number of laser pulses needed to drill through the film, and a highly sophisticated image wobbling unit is required in order to achieve submicron accuracy.

An alternative technique that can be employed with Step & Repeat is to image the hole from the side where the ink exits using high Numerical Aperture (NA) optics, rotating beam and high fluence to drill a negative taper [6].

With SIS, however, there is no need for a special technique. The only difference when drilling tapered rather than cylindrical holes is in the mask design – instead of an array of identical apertures, the diameter of the apertures decreases linearly as explained in subsection 2.3.3.

3.2   A selection of results

3.2.1   Inkjet printer nozzles

Inkjet printer nozzle drilling is a good example for demonstrating that the advantages of the SIS technique can indeed be exploited for industrial application.

Historically inkjet printer nozzle drilling is a field where direct laser machining with excimer laser mask projection is well established [7]. Polyimide (PI) is a material well suited for inkjet nozzle plates and shows high absorption in the UV [8]; hence excimer lasers are the first choice for machining it. Inkjet nozzle drilling is often used as a prime example for the industrial use of excimer lasers for direct ablation. All the advantages of this technique can be exploited. Thanks to the short wavelength and high quality optics a high resolution is achieved, hence small and precise holes can be drilled [9].

A state-of-the-art inkjet nozzle has typically an ink exit diameter of 20 – 30 μm and an entrance diameter of 40 – 50 μm, with tolerances on these dimensions of ±0.5 μm. The PI film is usually 50 μm thick with a hydrophobic layer at the exit hole side. Telecentricity of the entrance and the exit is very critical as it determines the direction of the ink droplet ejected from the nozzle. Table 6 gives an overview over the nozzle parameters important for achieving high quality printing. Although a nozzle seems to be a fairly simple feature to produce, tight tolerances on various parameters make it a challenge.

Diameter tolerance (entrance and exit) ±μm	Telecentricity angle of the holes		Taper tolerance ± degrees
Hole diameter (μm)	Can be defined as ± μm from entrance to exit	Can be defined as ± degrees from entrance to exit	
Position tolerance ±μm	**Hole pitch** (μm)		**Ellipticity** Difference between axes (μm)

Table 6. Overview over all important parameters of an inkjet printer nozzle.

Hence all the points about stage accuracy and minimal jitter discussed in subsection 3.1.1 as well as the averaging of power when creating the holes (cf. subsection 3.1.2) are relevant for inkjet nozzle drilling, especially the latter as a significant amount of shots is needed to drill through the PI film.

Using SIS to fabricate inkjet printer nozzles has several major advantages compared to the Step & Repeat methods currently used. Since each nozzle is no longer subjected to an individual unchanging illumination pattern and is created by the superposition of images from all areas of the mask pattern, all nozzle telecentricity errors (due e.g. to lens non-telecentricity) and exit nozzle diameter size errors (due e.g. to non-uniformity of mask illumination or ablation plume shielding) are dramatically reduced.

Figure 31 gives a good idea of the quality that can be achieved for nozzles drilled by SIS. It shows two sections of a long nozzle array. The entrance and exit holes are well-defined circles of ±0.5 µm roundness and the nozzle wall is very smooth. Figure 32

Figure 31. SEM picture of a nozzle array drilled by the SIS technique.
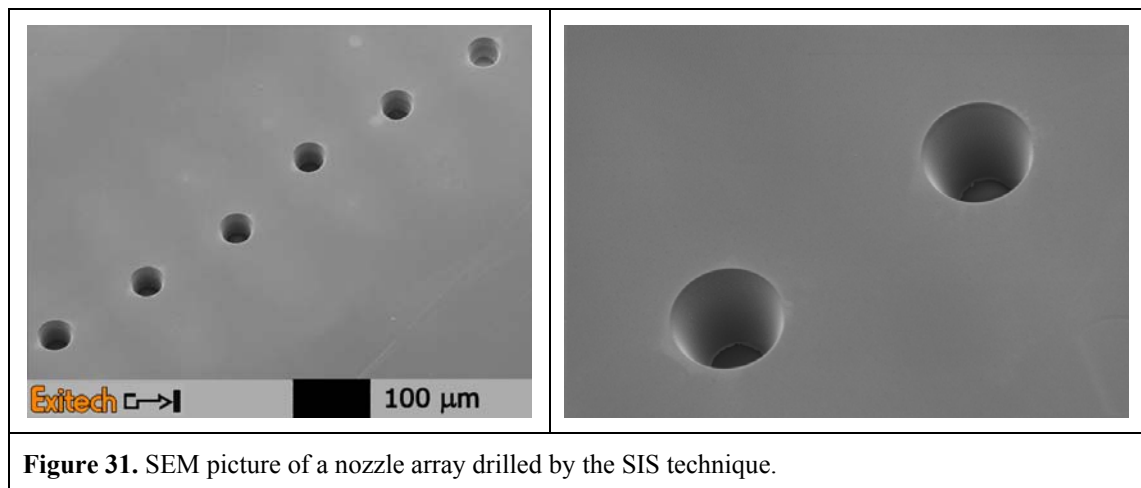
plots the exit diameter of 250 holes of a nozzle array where for more than 98% of the holes the diameter is within 1 µm. Note that this has been achieved without spending much time on process optimisation using assist gas, scan speed or other kinds of tuning. It is reasonable to assume that by optimising the process parameters all of the exit holes can easily be machined within 1 µm.
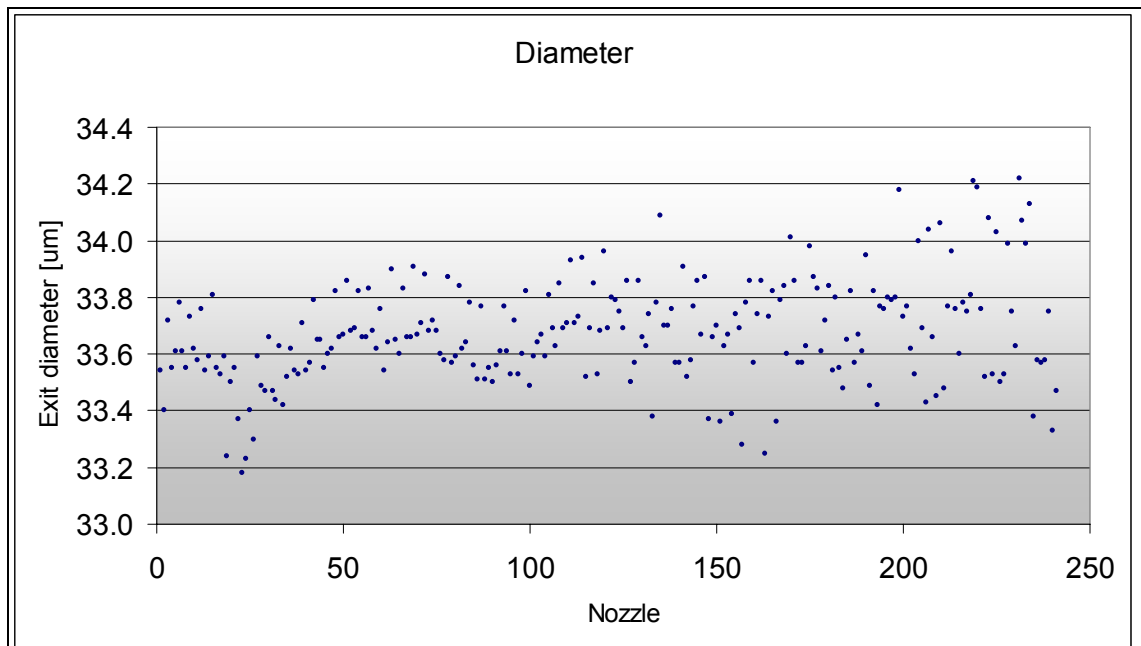
Figure 32. Nozzle array exit diameter measurements; more than 98% of the holes are within 1 μm.

3.2.2 3D micro-structuring

Moving on from relative simple nozzle structures we present now a portfolio of different 3D feature arrays direct laser machined by SIS. The purpose of this subsection is to show how powerful SIS is in creating a wide variety of geometrical structures in the micrometer range and that the theoretical ideas result indeed in a reasonable agreement between design and realisation. The results are presented in the form of SEM pictures thus giving a qualitative impression rather than a quantitative analysis. A more in-depth discussion will follow in the next chapters focussing on micro-lens arrays as one significant type of optical arrays.

Please note that as arrays are machined, not only the feature design is relevant but also the packaging and fill factor. Table 7 gives an overview over the types of feature arrays that are presented. What follows is for each feature array a drawing with dimensions, an SEM picture of the result and the most influential machining and mask parameters. The machining parameters given are the fluence value during processing and the scan

direction chosen. The fluence determines the ablation depth per shot, i.e. Δz for each

aperture, and is thus finally responsible for the correct depth and shape of the feature.

The scan direction seems to make a visible difference to the surface quality. Concerning

the mask parameter, 'number of linear arrays in image' means how many features are

machined in parallel during one scan; this can influence the result as we will see later.

The results represented by SEM pictures are each discussed briefly. Note that this is not

a detailed discussion as it would surpass the frame of this work to investigate every

possible feature array but as mentioned above the following chapters will concentrate on

lenses as representative 3D features and thoroughly discuss the issues arising here. All

results shown have been machined with the same optical components and the

micromachining system introduced in section 2.2. The sample material used was

Polycarbonate film.

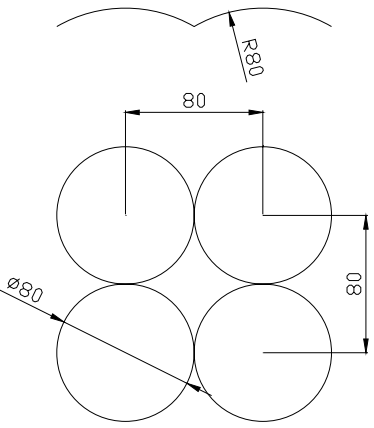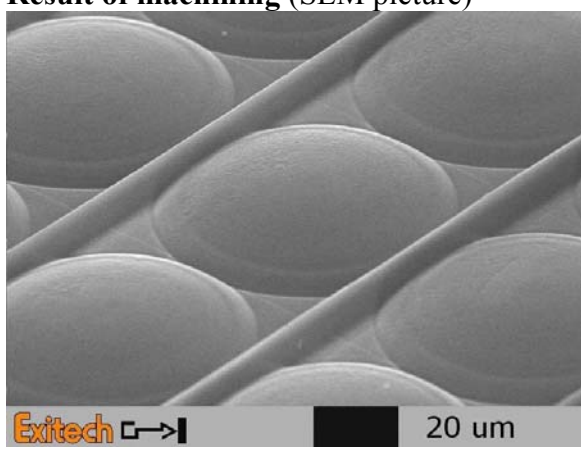| Lenses	Pyramids / Corner cubes	Others
Convex, spherical; square packaging	Down-pointing pyramids, square packaging	Zig-zag profile
Concave, spherical; hexagonal packaging	Free upstanding pyramids, square packaging	Ramps
Fresnel; square packaging	Down-pointing corner cubes	Sinusoidal profile
Table 7. Three important categories of features that can be machined by SIS.		

3.2.2.1 Lenses

Micro-lens arrays are undoubtedly the most widely spread micro-optical elements used

in all sorts of applications [10,11,12,13]. The following three different lenses machined

by SIS are a small collection of the design variations possible for the lens shape as well
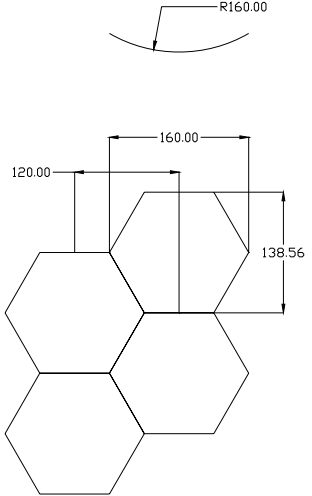
as the packaging of the lenses in the array.

Convex spherical lens (cf. Table 8)

The first qualitative look at the SEM picture shows that there is definitely a lens-type

structure machined. The surface seems relatively smooth although a ring-like artefact

appears about 1/3 up the lens. It is not understood what has caused this. An obvious deviation from the designed lens shape is not visible. Nevertheless a not designed feature appears in the array: a ridge along every lens row. The ridge runs in the direction of the main scan and is as high as the lenses themselves.

Feature parameters Radius of curvature (ROC): 80 μm Aperture diameter (d_a): 80 μm Square packaging: 80 μm x 80 μm	**Machining parameters** Fluence: 200 mJcm^{-2} Number of linear arrays in image: 1 Scan direction: negative
	Result of machining (SEM picture)

Table 8. Parameters and SEM picture for convex spherical lens machined by SIS.

Concave spherical lens (cf. Table 9)

Feature parameters Radius of curvature (ROC): 160 μm Aperture diameter (d_a): 160 μm Hexagonal packaging	**Machining parameters** Fluence: 200 mJcm^{-2} Number of linear arrays in image: 6 Scan direction: positive
	Result of machining (SEM picture)
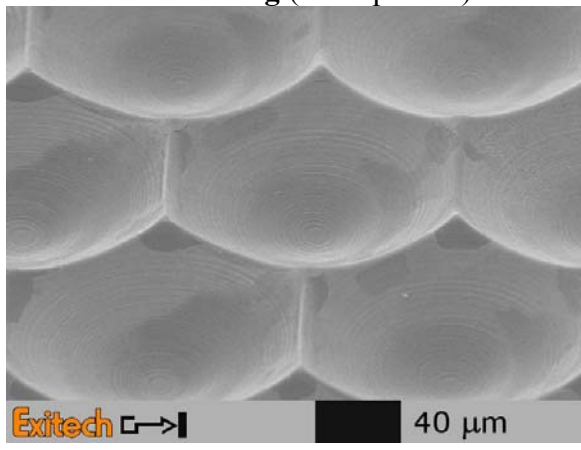
Table 9. Parameters and SEM picture for concave spherical lens machined by SIS.

This is an example of a 100% fill factor design of a concave lens, and the result is in good agreement with it. The edges where the lenses meet have only a small radius and are clearly defined. There is no ridge over the whole array visible (also if zoomed out) but a ring structure on the lens surface and darker patches on the peaks where the lenses meet. A closer investigation reveals that the whole structure is coated with a thin debris layer and the dark patches are areas where the debris layer is broken off. The main scan direction is in the long axis of the image. The ring structure is possibly caused by the diffraction effects on the sharp contrast edges of the apertures.

Convex Fresnel lens (cf. Table 10)

Feature parameters	Machining parameters
Radius of curvature (ROC): 80 µm Aperture diameter (d_a): 80 µm Square packaging: 80 µm x 80 µm	Fluence: 200 mJcm^{-2} Number of linear arrays in image: 2 Scan direction: negative
	Result of machining (SEM picture)

Table 10. Parameters and SEM picture for convex Fresnel lens machined by SIS.

This simple Fresnel lens is an example of the design options available with SIS. Qualitatively the result is in good agreement with the design, nevertheless there is again a ridge visible parallel to the scan direction, although only every second row. Note that there are two linear arrays in the scanning image. The surface seems smooth on both the lens and the ablated area between the lenses. The deviation from the step design in the
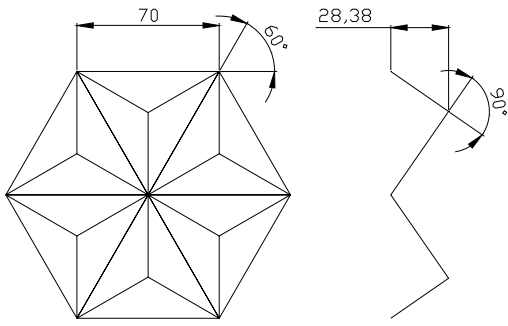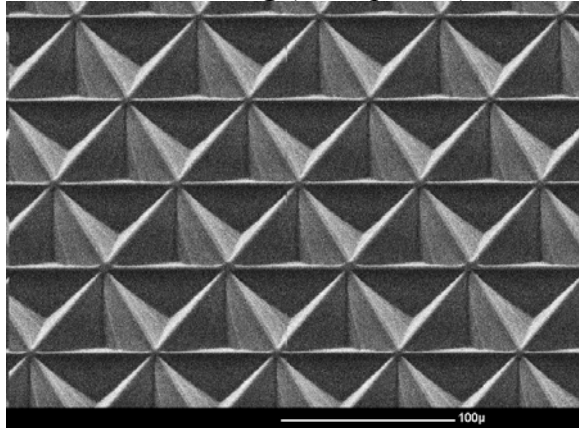
lens is significant as the wall angle is obviously not 90° and the edge that should be sharp is rounded. Both these errors will have significant influence on the optical performance. As the optical resolution is limited and the fluence relatively low, these errors can be regarded as typical for direct laser ablation.
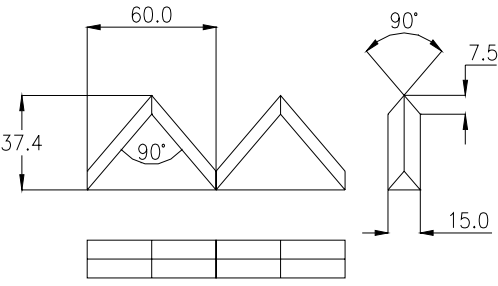
3.2.2.2 Corner cubes

The following examples demonstrate that SIS is not restricted to lenses as such; the features here have flat surfaces instead of curved ones.

Down-pointing corner cube (cf. Table 11)

Corner cubes are another very important type of optical feature hence chosen here as a demonstrator [14]. The result is a well represented structure with remarkably well-defined edges; no ridge is visible on the sample. Note the sharp pointing at the bottom where the planes meet. The walls look straight and the surface roughness seems low. There is a small radius along the top ridge. The scan started with maximum mask transmission.

Feature parameters	Machining parameters
Side length: 70 µm Vertex angle: 90°	Fluence: 400 mJcm^{-2} Number of linear arrays in image: 6 Scan direction: positive
	Result of machining (SEM picture)

Table 11. Parameters and SEM picture for down-pointing corner cube machined by SIS.

**Zigzag profile** (cf. Table 12)
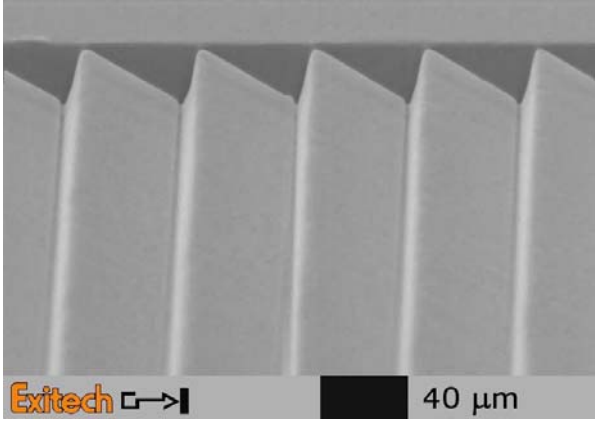
Feature parameters Pitch: 60/15 μm Depth: 37.4 μm	Machining parameters Fluence: 400 mJcm^{-2} Number of linear arrays in image: 20 Scan direction: positive
	Result of machining (SEM picture)
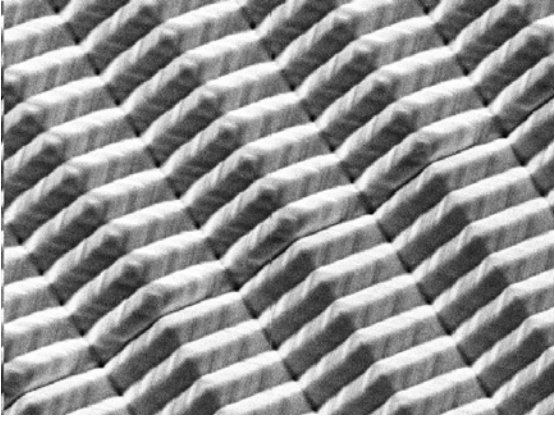
Table 12. Parameters and SEM picture for zigzag profile machined by SIS.

This zigzag profile represents a rather complex structure and makes the point that there is a high degree of freedom in feature design when using SIS. While the surface is qualitatively structured with the designed geometry, the surface quality is not very high. Steps and irregularities can be seen. The main scan direction was in the long axis of the prisms.

3.2.2.3 Geometrical 1D arrays

Dropping one dimension in the array opens up the option to choose the main scan direction relative to the feature array. This choice will determine the mask pattern: while for the scan perpendicular to the features the mask pattern consists typically of rectangular apertures arrayed parallel to each other and spaced by the array pitch, the mask pattern for the case of a parallel scan looks rather like a strongly elongated cross-section of the feature itself. The following two examples demonstrate both options. It can be argued that 1D arrays may as well be machined by the well-known mask dragging technique [15], but so far cutting speed and surface quality have not been good enough for industrial applications.

Ramp, 1D array (cf. Table 13)

Feature parameters	Machining parameters
Pitch: 50 μm Depth: 80 μm	Fluence: 200 mJcm^{-2} Number of linear arrays in image: 1 Scan direction: negative and perpendicular to the array
28.87 60° 50.00	**Result of machining** (SEM picture) Exitech □→│ 40 μm
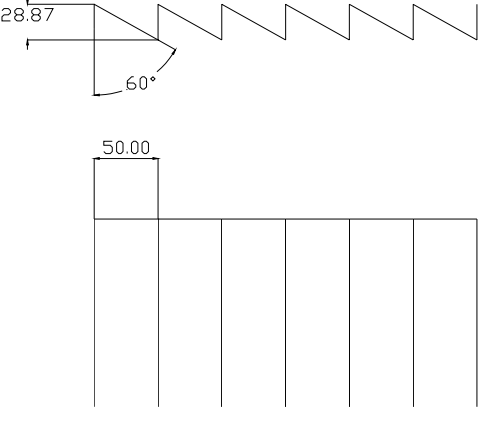
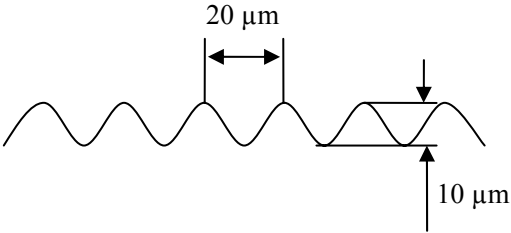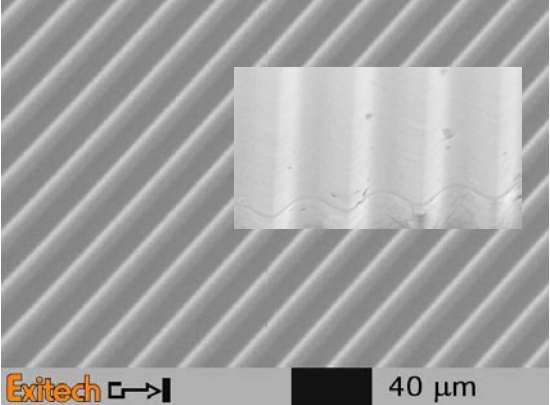**Table 13.** Parameters and SEM picture for ramps machined by SIS.

As expected from the results of the pyramids above the ramp slope looks straight although the result deviates from the saw tooth profile as the vertical edge is not achieved. It is the same phenomenon as seen in the Fresnel lens. A careful look reveals that in the lower corner a small grove is etched; this is most likely caused by diffraction at the mask and reflection effects on the workpiece. No stepping can be seen on the ramp surface. Using a mask design to scan perpendicularly to the grating structure as shown here will create a ridge when scans are stitched together to cover a bigger area. As 1D arrays allow the freedom to choose the main scan direction, the alternative option is to design the mask such that the scan is parallel to the grating. This has the advantage that the edge of the image can be made to coincide with the top edge of the saw tooth profile and thus nearly eliminate the ridge between stitched scans.

Sinusoidal profile, 1D array (cf. Table 14)

The sinusoidal profile is well carved into the polymer representing yet another optical structure realised by SIS. There is some distortion as the wave is rounder on the top than

at the bottom as can be seen in the inset picture. The continuous surface looks smooth.

Here the profile was cut in a parallel fashion.

Feature parameters Pitch: 20 μm Depth: 10 μm	Machining parameters Fluence: 200 mJcm^{-2} Number of linear arrays in image: 1 Scan direction: negative and parallel to the array
	Result of machining (SEM picture)

Table 14. Parameters and SEM picture for sinusoidal profile machined by SIS.

3.3 Conclusions

Even in the simple case where all the apertures on the mask are identical SIS is superior to the classic Step & Repeat technique in that higher quality and consistency can be achieved due to averaging effects. Furthermore, it will be more efficient in many situations. If a controlled taper is to be created, this is achieved much more easily with SIS than with Step & Repeat. And when it comes to patterning areas with 3D micro-structures, SIS is the only viable option. The examples shown in this chapter give an impression of the variety of 3D micro-feature arrays that can be realised with this technique.

The focus will now shift from what is possible to how well it is possible. The next few chapters will concentrate on quantitative evaluation of achievable tolerances on shape representation, artefact elimination and surface quality. Further we will explore if the

direct laser cutting of 3D micro-feature arrays can be expanded to materials other than Polycarbonate.

---

1. B. Burghardt, S. Scheede, R. Senczuk, H.-J. Kahlert, Appl. Phys. A 69, 137 (1999)

2. D. Lidzey, M. Voigt, C. Giebeler, A. Buckley, J. Wright, K. Boehlen, J. Fieret, R. Allott, Organic Elec. 6, 221 (2005)

3. G. Kamlage, T. Bauer, A. Ostendorf, B. Chichkov, Appl. Phys. A 77, 307 (2003)

4. K. Boehlen, P. Rumsby, A. Cerezo, M. Huang, SPIE Vol. 4557, 129 (2001)

5. S. Lazare, J. Lopez, F. Weisbuch, Appl. Phys. A 69, 1 (1999)

6. Patent: WO9726137, Method of and apparatus for forming nozzles, Xaar ltd (GB)

7. Patent: US 5305015, Laser ablated nozzle member for inkjet printhead, Hewlett-Packard Company (US)

8. J. Lankard, G. Wolbold: Appl. Phys. A 54, 355 (1992)

9. C. Rowan: Laser Focus World 31, 23 (1995)

10. M.C. Hutley, Phys. Educ. 29 (1994)

11. D. Daly, R. Stevens, M.C. Hutley and N. Davies, Meas. Sci. Technol. 1, 759 (1990)

12. Ph. Nussbaum, R. Volkel, H. Herzig, M. Eisner and S. Haselbeck, Pure Appl. Opt. 6, 617 (1997)

13. C. Hembd-Soelner, R.F. Stevens and M.C. Hutley, Pure Appl. Opt. 1, 94 (1999)

14. S. Wang, D. Zhao, F. Huang, Opt. Eng. 41, 1396 (2002)

15. N. Rizvi, J. Greuters, J. Dallimore, K. Hamilton, R. Clabburn, B. Ebsworth, SPIE Vol. 4274, 278 (2001)

4 Reproduction of design by SIS and various metrological approaches

4.1 Introduction

The experiments described here are designed to give some more quantitative data about how well a 3D shape is reproduced in the SIS process. In chapter 3 a wide variety of different shapes and profiles have been presented. Here an array of a spherical micro-lenses is used to investigate within what tolerances it is realistic to direct-cut a given lens design to a convex as well as concave profile. A spherical lens shape has been chosen because it represents a very important optical element [1]. Furthermore, one may assume that if it is possible to control the profile of an arc precisely, then the same will be true for ramps or free-form profiles.

4.2 Theoretical or pre-experimental considerations

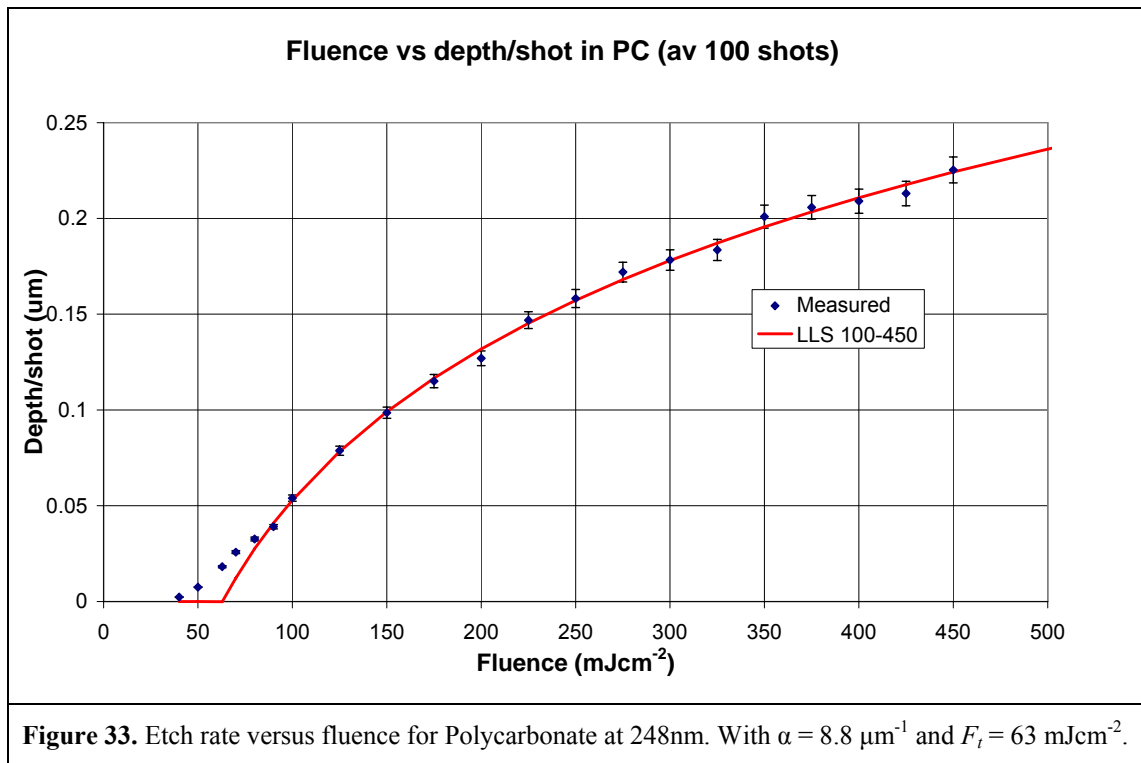The procedure for the experiment presented consists of seven steps:

1. Define the micro-lens array.

2. Find the ablation curve for the given material.

3. Determine a suitable fluence.

4. Find the number of apertures required based on the slice thickness (i.e. the ablation depth per shot).

5. Design the aperture array.

6. Etch the lenses in a fluence range somewhat above and below the chosen fluence, testing positive and negative scan directions.

7. Evaluate the resulting lenses.

These seven steps can be generally applied if SIS is used to etch micro-features. Hence they are described in more detail while focusing on a specific micro-lens array etched into Polycarbonate.

1. Define the micro-lens array:

The lens is spherical and has a radius of curvature of 60 μm and a full aperture width of 100 μm diameter; it is arrayed on a rectangular grid with a 100 x 100 μm pitch.

2. Find the ablation curve for the given material:

Figure 33. Etch rate versus fluence for Polycarbonate at 248nm. With α = 8.8 μm^{-1} and F_t = 63 $mJcm^{-2}$.

Polycarbonate was etched at a fluence range from 10 – 450 $mJcm^{-2}$ and 10 or 100 shots per area at 30 Hz. The resulting depth was measured with an Ambios XP2 stylus profiler and then divided by the number of shots; 100 below 100 $mJcm^{-2}$ and 10 above it. Experimental etch rates were analysed by fitting the curve to the ideal form of the equation:

$$d = \frac{1}{\alpha} \cdot \ln\left(\frac{F}{F_t}\right)$$
Equation 19.

where *d* is the etch depth per pulse, α is the effective absorption coefficient and f_i is the ablation threshold fluence. Because of the strong deviation from the ideal curve below ~100 $mJcm^{-2}$ these value were ignored when fitting the curve. Nevertheless this

tailoring off is a well known phenomena [2]. The values found for $\alpha = 8.8$ μm^{-1} and $F_t = 63$ mJcm^{-2}. The error bars for the measurements are set at 3%.

3.   Determine a suitable fluence:

There is a certain degree of freedom in selecting the process fluence. In theory any fluence above the nominal threshold will work as long as each pulse results in the same ablation depth. However, this is questionable at low fluences (< 100 mJcm^{-2}) where an incubation effect can be observed: a single shot ablation depth is significantly less (if at all measurable) than a multi-pulse exposure divided by the number of pulses [3]. As SIS is suitable for large area machining, it is important to find an efficient fluence if possible. A plot of the data for ablated volume per Joule versus fluence for Polycarbonate is shown in Figure 34. It can be seen that the most efficient etch fluence for Polycarbonate is at $F = eF_t$ and in this case at 171 mJcm^{-2}. Hence this should be a good choice for the process fluence for SIS.

Figure 34. Ablated volume per Joule versus fluence for Polycarbonate.
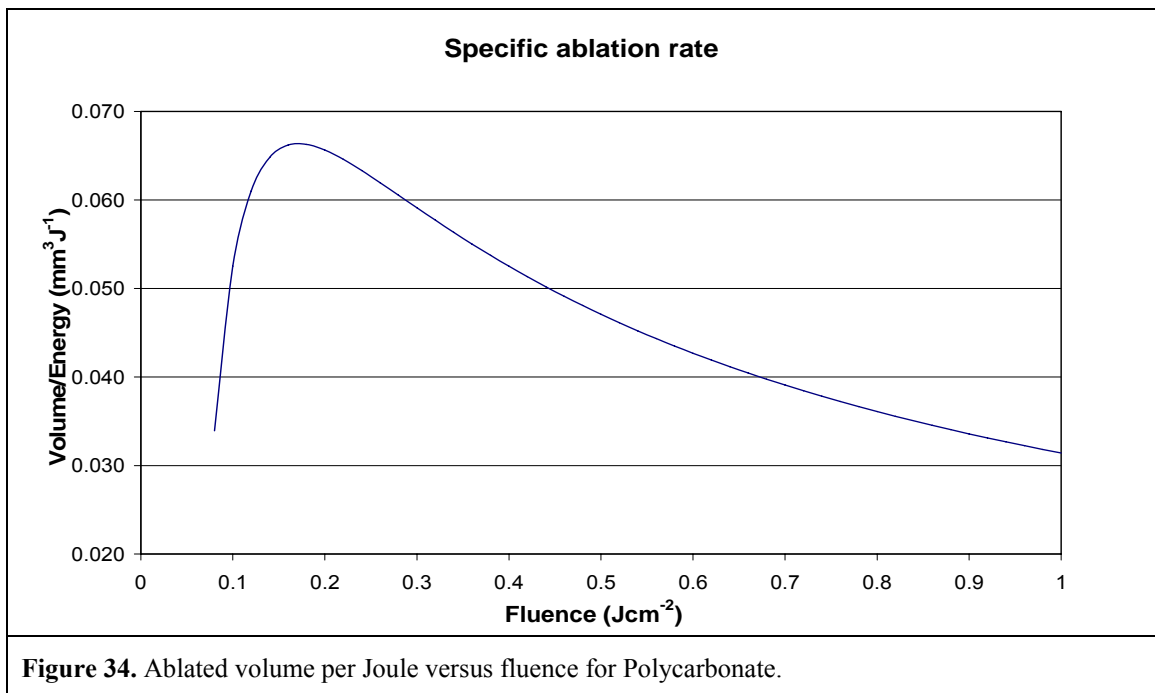
Unfortunately there are at least two other important issues to consider. One is that at low fluences debris or other particles on the surface can more easily cause micro-cones

to develop [4]. The other is that the achievable slope angle and hence the maximal wall steepness on features is also reduced at low fluences [5].

Thus the process fluence will be a compromise between efficiency and maximal feature wall angle (measured with the horizontal). For shallow features it could be advantageous to reduce the ablation per shot to say 50 nm to be able to increase the number of apertures and therefore reach a higher resolution to resolve the feature profile. For this specific experiment the sag height is 26.8 μm and the maximal angle at the lens is 57°. Here a nominal process fluence of ~400 mJcm^{-2} was chosen.

4.   Find the number of apertures required based on the slice thickness:

The next step is to determine the number of apertures for the mask pattern. The number of apertures n_a is:

$$n_a = \frac{h_s}{d}$$

Equation 20.

where h_s is the sag or feature height and d the ablation depth per pulse or slice thickness. It is clear that n_a needs to be an integer. As the target for the process fluence is at 400 mJcm^{-2} and $\alpha = 8.8$ μm^{-1} and $F_t = 63$ mJcm^{-2}, we find $d = 0.210$ μm and thus $n_a = 128$. Note that the actual mask used in the experiment has 129 apertures resulting in $d = 0.207$ μm and a nominal process fluence of 392 mJcm^{-2}.

5.   Design the aperture array:

Using the sag equation and the slice thickness it is now possible to determine the diameter for each of the 129 (circular) apertures. These apertures are arrayed linearly starting with the biggest and ending with the smallest aperture with the pitch between them equal to the pitch of the micro-lens array (in this case 100 μm) divided by the demagnification of the projection lens. For the experiments in consideration the

apertures were used to create mask patterns for concave and convex lenses. The basic array was then repeated to create 2 and 10 rows of lenses, respectively, in one scan.

6. Etch the lenses:

Install the mask in the imaging system and scan through a fluence window of ±20% of the nominal process fluence, which should give a good chance of machining the target design of the lens. Testing both scan directions, positive and negative, will give further knowledge about the ablation process and the accuracy of the ablation model applied.

7. Evaluate the resulting lenses:

To analyse the lenses, measurements with a Dektak M6 holding a stylus with a tip angle of 40° and tip radius of 0.7 μm are made. Furthermore, optical and electron beam microscopy plus white light interferometry are employed. Additionally the optical performance of the lenses is tested.

4.3 Design of experiment

The experimental arrangement used to etch lenses into Polycarbonate is the same as the one described in chapter 2. The Polycarbonate film used is 0.5 mm thick Lexan 8010. The energy in the laser beam, after passing through a rectangular mask aperture and imaging lens, is measured with a calibrated Gentec Solo PE energy monitor and a Gentec QE50 head. The image size is 14 mm x 1.275 mm. The energy is recorded for a range of attenuator positions between 60–90 % transmission corresponding to a fluence window between ~300 and 500 mJcm^{-2}. Typical variations in the power measurements are in the range of 1–3%.

A chrome-on-quartz mask with aperture arrays as described above is used for a series of SIS scans in the positive and negative scan direction at different fluences and for static ablation of Polycarbonate around the nominal fluence. The scan through a fluence range

has two purposes: one is to find the best process fluence and the other to find out how big the process window is. The laser repetition rate is chosen to be 30 Hz.

4.4 Analysis of results

The question of how to test micro-structure arrays in general and lenses in particular deserves a far more detailed consideration than it is possible to give here; it will probably require the development of new procedures and specially designed equipment. However, in the interim a variety of simple techniques have been applied enabling us to obtain a good impression of the overall quality of the micro-lens arrays etched as described above. In this section we will discuss the sample results and at the same time make some comments on the metrology used in each case and its strengths and weaknesses.

The following techniques are employed for the analysis of the results:

For inspection of geometry and surface roughness:

    A. Optical microscopy

    B. Scanning Electron Microscopy (SEM)

    C. White-Light Interferometry (WLI)

    D. Stylus profiling (Dektak M6)

For inspection of optical performance:

    E. Optical microscopy with point source illumination

    F. Refraction of individual lens at 532 nm

4.4.1 Inspection of geometry and surface roughness

A. Optical microscope

The inspection with an optical microscope is in most cases the fastest and easiest way to look at the micro-features produced. With a good microscope and high magnification optics it is possible to analyse micro-structures qualitatively to a satisfactory degree.

Figure 35 shows a 200 times magnification of the top view of convex lenses machined in positive scan direction.

Figure 35. Top view of convex lenses machined in positive scan direction.	**Figure 36.** Top view of convex lenses machined in negative scan direction.	**Figure 37.** Cross-sectional view of convex lenses machined in positive scan direction.
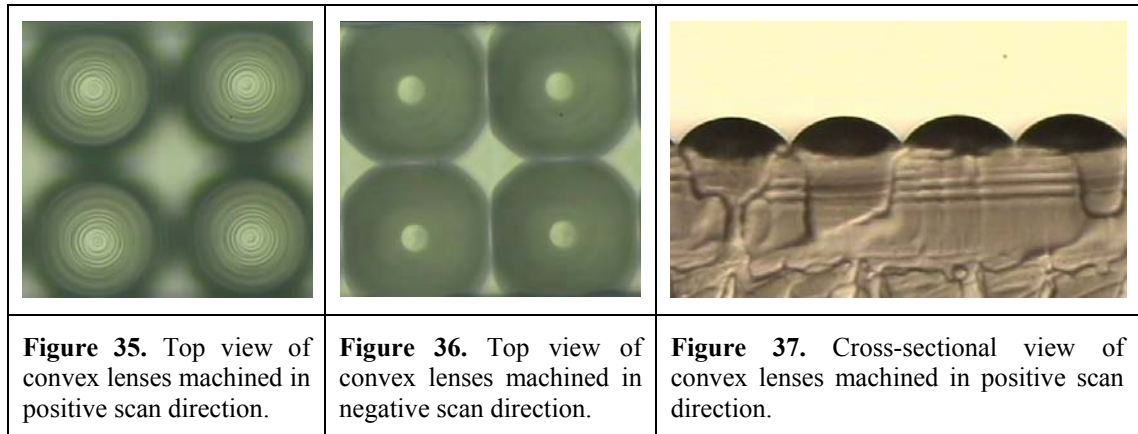
There are ring structures clearly visible on the lens. By scanning the focal plane of the microscope from top to bottom a lens structure can be discerned. To get a better impression of the profile of the lens it is necessary to cross-section the sample and look at it from the side. Figure 37 is a picture of a cross-sectional view of convex lenses machined in positive scan direction. The lenses appear black as the light is not reflected back into the microscope lens; the structures in the material below the lenses are a result of snapping the Polycarbonate film.

A top view of convex lenses machined in negative scan direction (Figure 36) reveals a bright dot at the top of the lenses but no rings; the lenses also seem to melt together at the bottom. Further investigation reveals that the bright dot is actually a flat area at the lens top and that the ring structures appearing in the positive scan are much weaker or not visible at all.

From the observations by microscope it can be concluded that the etched structures are indeed well-defined micro-lenses. The lenses produced in a positive scan compared with those produced in a negative scan appear to have a rougher surface but match the target geometry better as their counter-parts have most likely a flat top of ~10 μm diameter.

As the microscope employed is equipped with an encoder of submicron resolution on the *z*-axis, it is possible to measure the depth of the structures down to ~1 μm accuracy. Hence it is possible to measure the depth range resulting from the fluence range, and it was found to be between 25 μm and 29 μm.

It proves very difficult to quantitatively determine the profile of the micro-lenses by microscopy. As the lenses are only 100 μm in diameter, it is a challenge on its own to achieve a cross-section exactly through the centres of the lenses, and if this is not the case, then the depth of field or the magnification of the microscope lens limits the chance to get a sharp cross-sectional image of the lens; but this is the key to get a meaningful measurement of the micro-lens profile.

B. Scanning Electron Microscope (SEM)

The SEM is a very useful tool to get an impression of the quality of micro-structures. High resolution images with a respectable depth of focus are obtainable. Nevertheless it has the well-known drawbacks that the samples need to be coated with gold and often diced, i.e. destroyed, to get them into the vacuum chamber. The tip-tilt and rotary table inside the vacuum chamber is helpful for analysing the laser-etched structures. Figure 38 demonstrates that several aspects of a micro-feature can be investigated with a single
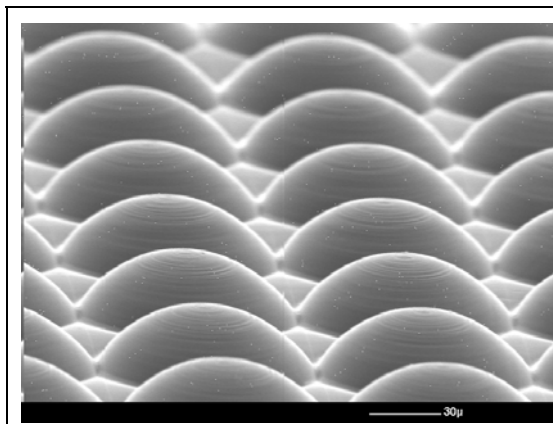

Figure 38. Convex lenses machined in positive scan direction.
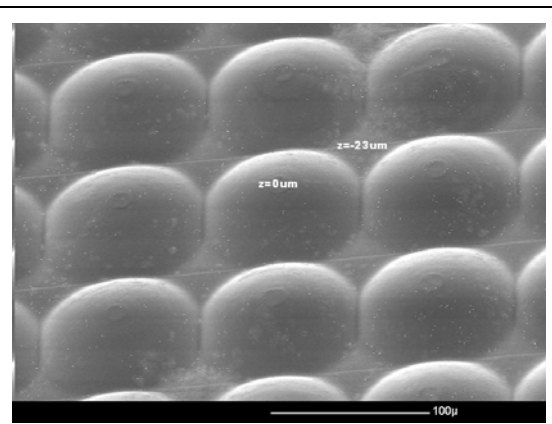
Figure 39. Convex lenses machined in negative scan direction.

SEM picture. While on the optical microscope it was necessary to cross-section the sample in order to see the lens shape, in the SEM it is sufficient to tilt the sample. The findings from the optical microscope are confirmed. The lens shape looks reasonable and there are ring like structures on the lens surface for the positive scan. The negatively scanned lenses (Figure 39) look much smoother but show again a circle on top that could indicate the edge of a flat area. Note that the light grey spots on the lenses are caused by the cleaning agent which has been left on the surface for too long a time.

Figure 40 and Figure 41 show concave lenses machined in positive and negative scan direction respectively. By the nature of the hollow structures the contrast is here less pronounced and it is not possible to see the profile of the lens as such. It can even be difficult to see that it is a concave lens, hence the introduction of the z-levels with $z = 0$ representing the top surface and $z = -26$ μm and $z = -25$ μm respectively the deepest point of the machined lens. What has been observed on the convex lenses does also appear here: the positive scan direction leaves ring-like structures on the surface while the negative scan makes the surface smooth. In this case it looks very smooth and nothing indicates a flat area. What can be seen in both cases is that some ablation happens where the lenses meet.
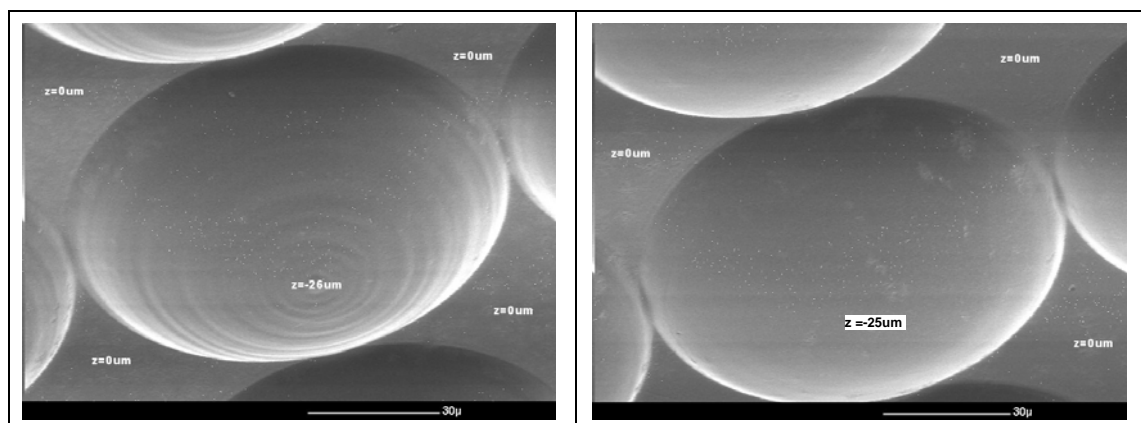

Figure 40. Concave lenses machined in positive scan direction.

Figure 41. Concave lenses machined in negative scan direction.

As mentioned before the SEM is particularly helpful to get a good impression of the overall quality of the micro-structure and its array, but it cannot produce the quantitative data like radius of curvature or surface roughness necessary to qualify a micro-lens.

C. White-Light Interferometer (WLI)

After the more visual inspections fail to result in accurate data sets the hope is that a WLI can deliver on this point. The WLI promises fast and accurate measurements of 3D structures, and one would expect it to be an ideal inspection tool for the micro-lenses in question.

The lens structures are inspected with a NT1100 (Veeco) with different magnification and NA lenses. It is discovered that the WLI has severe limitations in measuring slopes steeper than 20°, especially if the surface is smooth. There is simply not enough light reflected back into the microscope lens. Hence only the centre part of the laser etched lenses of about 40 µm diameter can be measured. This offers some information about the lens but it can obviously not been regarded as a full inspection of a micro-structure.
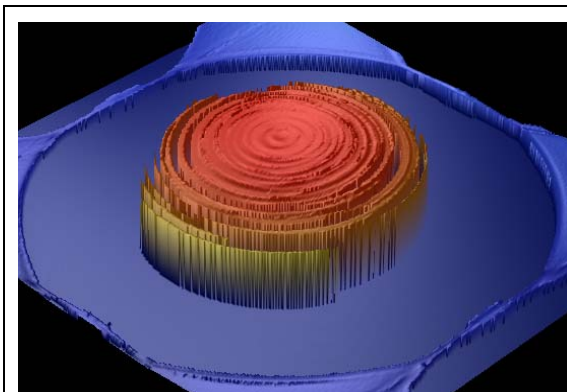
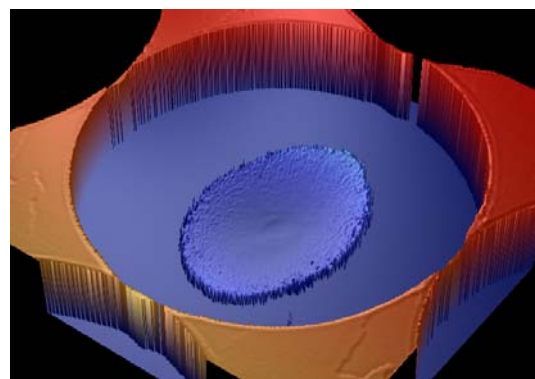|	
Figure 42. White-light interferometer plot of convex lens machined in positive scan direction. Darkest blue represents no data. $Ra = 38$ nm, $Rq = 51$ nm and $Rt = 300$ nm**.**	**Figure 43.** White-light interferometer plot of concave lens machined in negative scan direction. Darkest blue represents no data. $Ra = 7$ nm, $Rq = 12$ nm and $Rt = 60$ nm.

What is found is nevertheless interesting and confirms the findings from before. There are definitely ring-like structures on the surface of the positively scanned lens while

these structures are absent or only very weak in the negatively scanned lens (Figure 42 and Figure 43).

Although the ring-like structures on the lens surface look very severe, the measured roughness is surprisingly low with Ra = 38 nm, Rq = 51 nm and clearly below λ/4 for visible light. Nevertheless Rt is relatively high at ~300 nm (Ra: average roughness, Rq: root-mean-squared roughness, Rt: peak-to-valley difference) and the pitch of the rings is between 1 µm and 3 µm. The negative scan shows a different picture as the rings are absent and the surface looks smooth. The data confirm this. There is a small difference in roughness for convex and concave negative scans with Ra = 7 nm, Rq = 12 nm and Rt = 60 nm for the concave lens and Ra = 12 nm, Rq = 20 nm and Rt = 64 nm for the convex lens. The data are obviously only obtained in the centre part of the lens and hence not necessarily representative for the whole lens. Equally it is difficult to obtain accurate data to determine the ROC as only a relatively small part of the lens is measured.
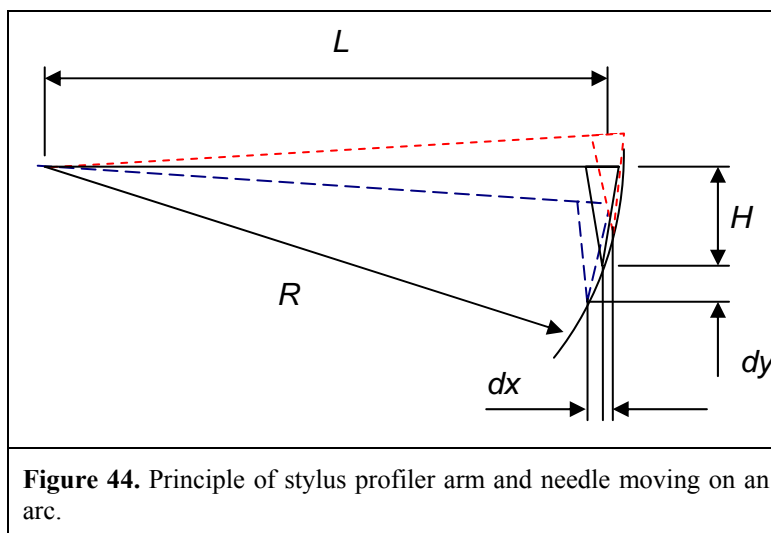
Although it is possible to measure parts of the lenses with the WLI, it can not be regarded as a sufficient metrology system to measure fast micro-lenses or indeed any micro-structures with smooth surfaces steeper than 20°.

D. Stylus profiler

As the optical inspection carried out cannot deliver the data needed to measure the full profile of the micro-lenses, a mechanical approach is taken next. It is understood that surface profilers can obtain line scans of a 3D topography. Historically surface profilers are mainly used to measure step heights, surface roughness, and film stress on wafers. The standard stylus needles have a tip angle of 60° and a sphere radius of several µm. Often the needle is slightly tilted thus restricting the maximal angle (with the horizontal) that can be measured to as little as 50°. Trying to measure a steeper slope results in

measuring the needle angle rather than the slope [6]. When looking at lens geometries with slope angles up to 54.4° and small gaps between lenses, it is paramount to get tighter specifications for the stylus needle. The needle chosen for the measurements here has an angle of 40° and a sphere radius of 0.7 µm, and the profiler employed is a Dektak M6 (Veeco). Unfortunately an XP-2 (Ambios) profiler with a custom-made needle of 20° and a sphere radius of < 200 nm is not able to measure the lens structure as the needle gets stuck in the lens array.

Surprisingly the Dektak M6 software has no function implemented that compensates for the distortion of the measured profile that results from the fact that the tip of the needle moves along an arc. The reason for this is that the needle is mounted on an arm pivoted on one end and that the scan axis *x* and the *z*-axis are being tracked completely independently and then merged in the data plot. Hence when the needle moves up from the zero position the slope will be plotted flatter, and when it moves down, the slope will be plotted steeper than it actually is. Figure 44 shows the principle of the arc movement of the needle in a Dektak M6 profiler. From the length of the pivot arm *L* and the total needle height *H*, the

Figure 44. Principle of stylus profiler arm and needle moving on an arc.

arc radius *R* can be determined. For each *dy*, the corresponding *dx* can then be calculated as

$$dx = L - \sqrt{R^2 - (H + dy)^2}$$

<div style="text-align: right">**Equation 21.**</div>

An Excel spread sheet and a Visual Basic program have been generated to be able to process the raw data and compensate for the arc movement of the stylus needle. The data presented below are all plots processed with the arc compensation.

The Dektak M6 used here is not equipped with a motorised *x/y*-table; hence it is not possible to scan an area but only a single line at the time. To obtain the lens profile it is therefore important that the stylus scan runs through the centre of the lens. To be able to achieve this a higher magnification alignment camera has been installed on the Dektak M6. It is then possible to align the sample parallel to the scan axis and to position the stylus in the centre of the lens.

With all these measures in place it is possible to collect meaningful data from the laser-etched lenses. Because measuring is slow and processing the data laborious, only individual lenses have been measured. It is clear that these few measurements do not represent a statistical average; nevertheless the results shown are typical and the variation from lens to lens in the same array machined under the same conditions is not dramatic; otherwise this would have been revealed by visual observation.

Figure 45–Figure 47 show plots of the lens profile obtained from lenses processed at 449, 463 and 477 mJcm^{-2}. It is found that the lens processed at 463 mJcm^{-2} matches the target profile best with an average deviation over the whole lens of 207 nm. Although the fluence change to the other two scans is only ± 3%, the average deviation increases to 228 nm and 251 nm respectively. Note that the pulse to pulse fluctuation is also around 3%, but as 129 pulses are needed to etch a lens, it is the average fluence that is relevant. A further increase or decrease in fluence automatically distorts the lens even more. Inspecting the deviation a bit more closely it can be seen that the average deviation within 90% of the aperture diameter is down at 138 nm with a maximal deviation of 460 nm. At the foot of the lens the deviation from the target profile increases to 1.2 µm.

The linear least square fit gives a radius of curvature of 60.7 µm at 463 mJcm^{-2} compared to 61.4 µm at 449 mJcm^{-2} and 60.8µm at 477 mJcm^{-2}.

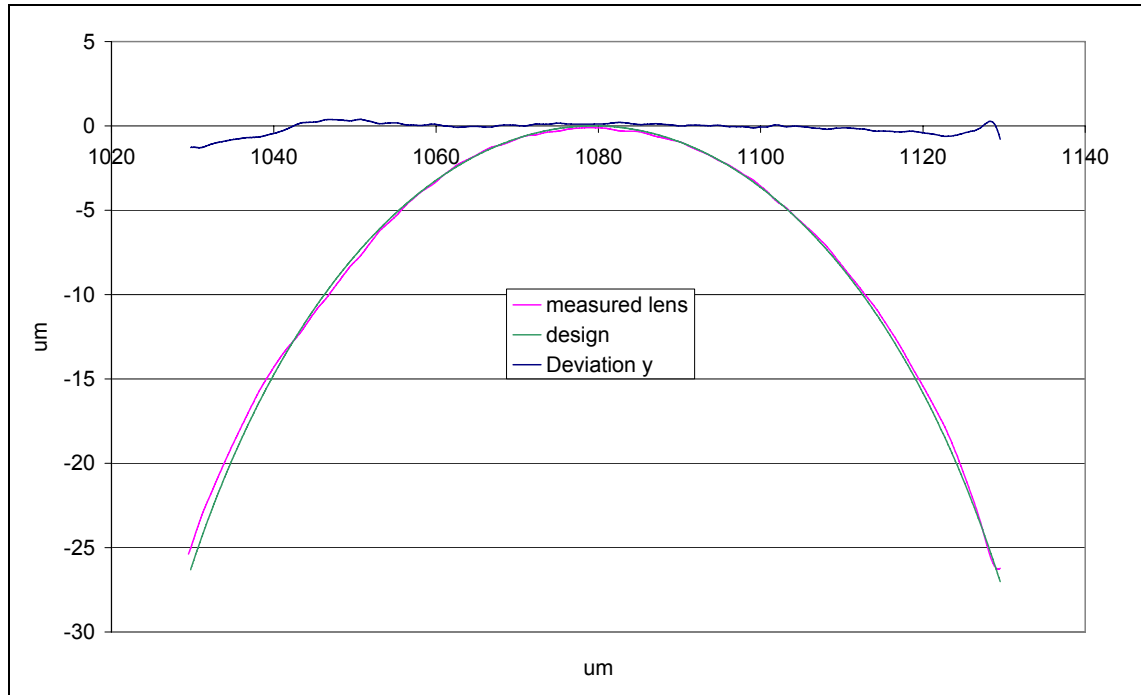**Figure 45.** Positively scanned lens etched at a fluence of 449 mJcm-2 resulting in an average deviation of 251 nm and Rq = 43 nm, Ra = 33 nm, Rt = 240 nm. Best fit ROC 61.4 µm.
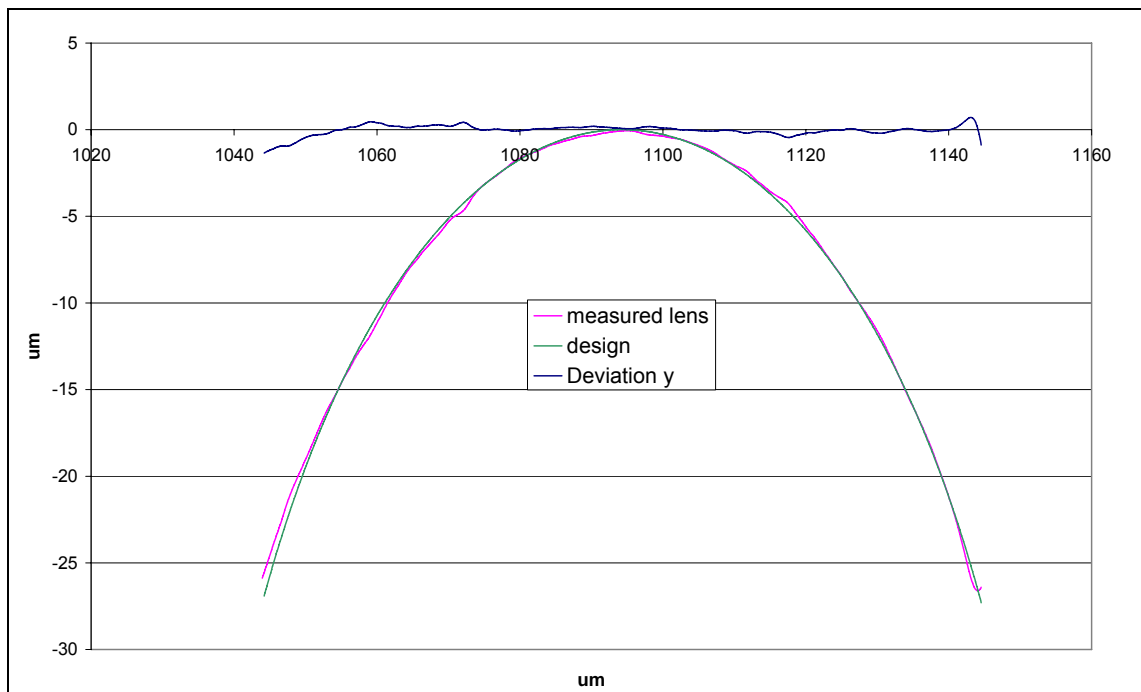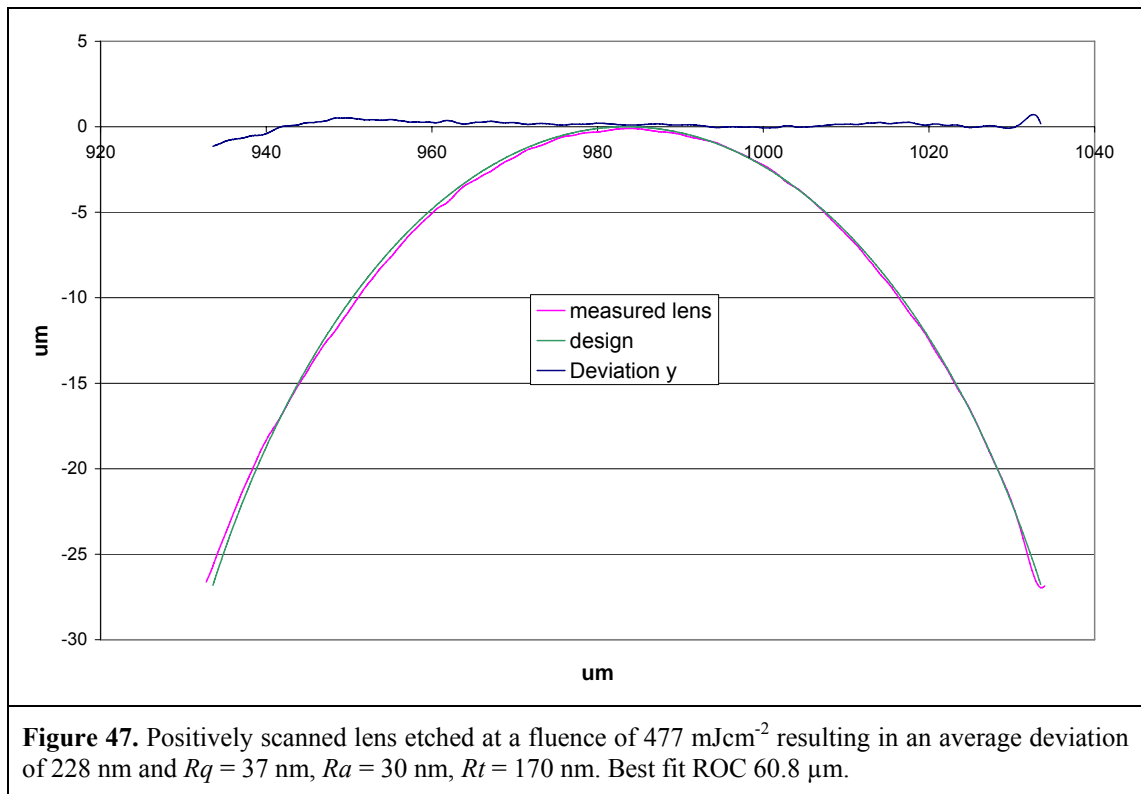

Figure 46. Positively scanned lens etched at a fluence of 463 mJcm^{-2} resulting in an average deviation of 207 nm and *Rq* = 55 nm, *Ra* = 42 nm, *Rt* = 293 nm. Best fit ROC 60.7 µm.

Figure 47. Positively scanned lens etched at a fluence of 477 mJcm^{-2} resulting in an average deviation of 228 nm and Rq = 37 nm, Ra = 30 nm, Rt = 170 nm. Best fit ROC 60.8 μm.

The surface roughness values in Figure 45-Figure 47 suggest that the higher or lower fluence result in a better surface quality. Measuring lenses processed at significantly higher or lower fluence does not confirm this tendency but reveals very similar Rq, Ra and Rt values. Without analysing many more lenses it is reasonable to assume that for positively scanned lenses roughness values do not get much bigger than Rq = 55 nm, Ra = 42 nm, Rt = 293 nm. The values of the WLI measurement are very slightly higher, which can problably be explained by the fact that with the WLI only the centre part of the lens is measured, which tends to be rougher than the rest of the lens.

The data of the same experiment but machined in the negative SIS scan direction shows a quite different picture. First of all with the fluence range applied it has not been possible to achieve the full depth of 26.8 μm. At the maximum fluence of 506 mJcm^{-2} only 23.3 μm have been reached. Note that for the positive scan direction a depth of 28.7 μm has been etched at this fluence. The insufficient total sag height indicates that the target profile has not been achieved. Indeed, the average deviation is 0.866 μm and,

more seriously, the measured data do not follow the designed profile at all. The top of the lens is flat (as concluded from the optical inspections), the sides are over-etched and the depth is not reached. Note that the best fit results in a ROC of 59.6 µm which seems very close to the target value of 60 µm but is completely meaningless in this case. Figure 49 shows the deviation plot on top of the measured and designed lens profile. Together they look like a bull's head with the deviation getting negative and then rising significantly towards the perimeter of the lens. This seems to be a typical appearance for negatively scanned lenses as Figure 48 shows the same pattern even though the lens was etched at a much lower fluence.

Considering the two plots it can be concluded that increasing the fluence further to reach the right depth will adversely affect the profile of the lens. The lower process fluence matches the lens profile at least for the top half better than the higher fluence. This finding is also confirmed by the fact that the average deviation for both fluences is very similar at around 860 nm although the maximum error for the lower fluence is nearly 8 µm while for the higher fluence it is 3.3 µm.

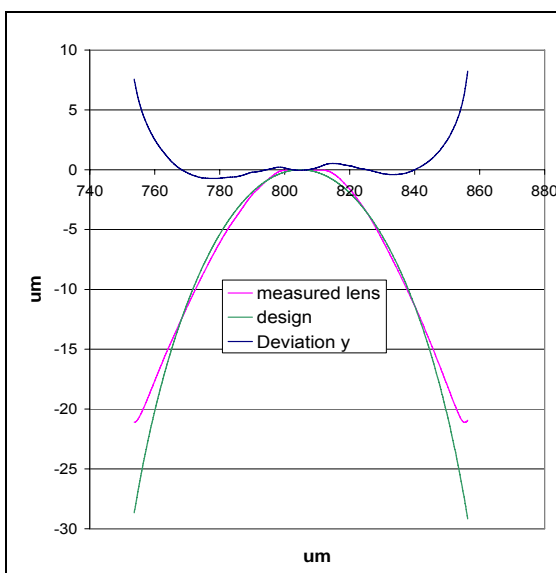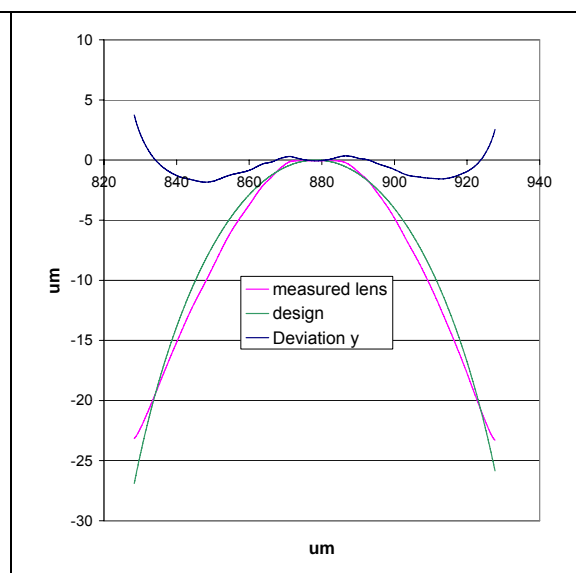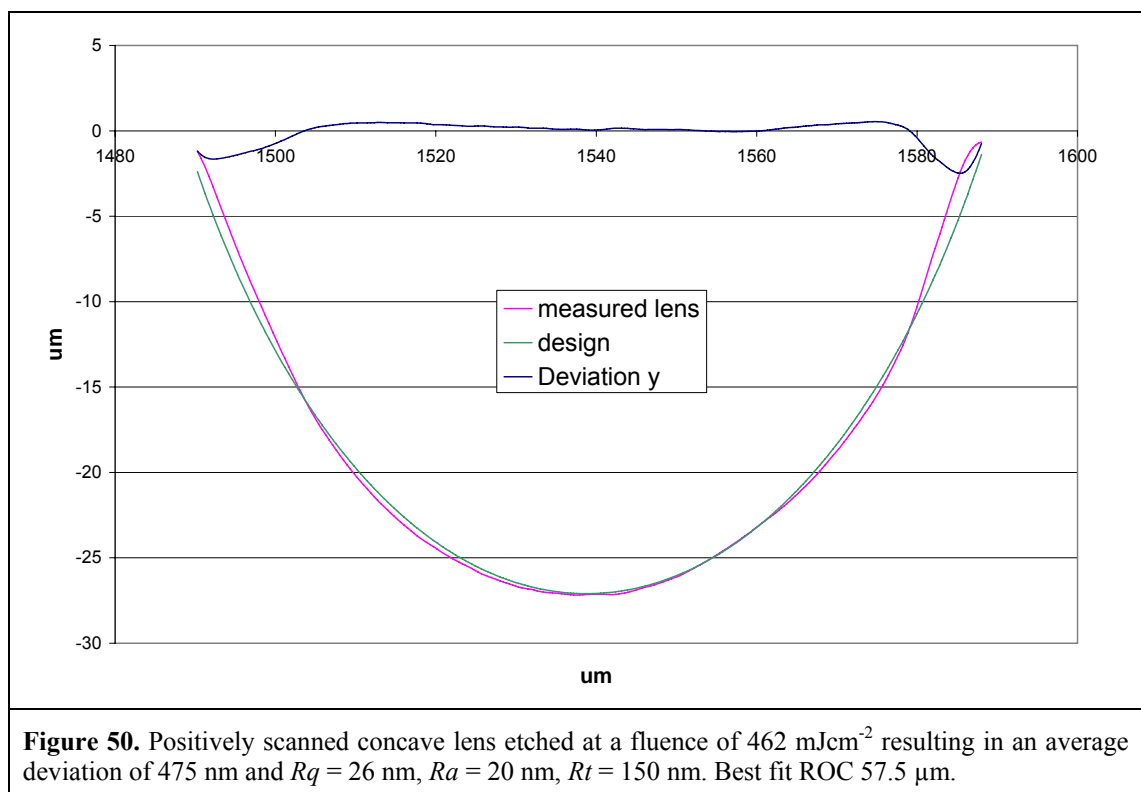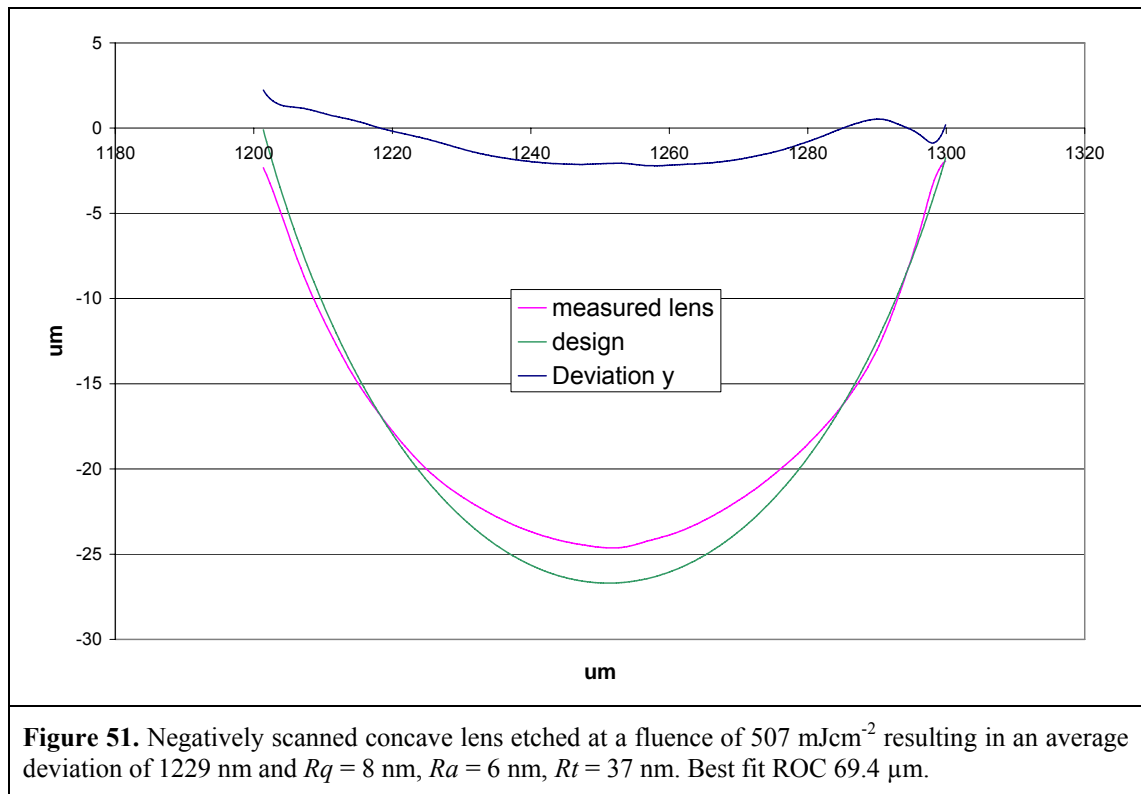|	
Figure 48. Negatively scanned lens etched at a fluence of 420 mJcm^{-2} resulting in an average deviation of 0.869 µm and max depth 21 µm, *Rq* = 12 nm, *Ra* = 9 nm, *Rt* = 64 nm. Best fit ROC 65.6 µm.	**Figure 49.** Negatively scanned lens etched at a fluence of 506 mJcm^{-2} resulting in an average deviation of 0.866 µm and max depth 23 µm, *Rq* = 13 nm, *Ra* = 10 nm, *Rt* = 45 nm. Best fit ROC 59.6 µm.

What has been observed optically and at least for the centre of the lens confirmed by the WLI is now proven: the surface roughness is much smaller for negatively scanned lenses. The values are with $Rq \approx 15$ nm, $Ra \approx 12$ nm, $Rt \approx 65$ nm less than one quarter of the corresponding values from the positively scanned lenses.

Having evaluated the convex lens the focus is now on the concave lens. It has been processed very much in the same way as the convex lens just changing the pattern on the mask from the convex to the concave design. The results are generally speaking the same as in the convex case. The positive scan direction etches close to the lens design with ring-like gratings on the surface while the negative scan produces a distorted lens with good surface quality. Figure 50 shows that the overall deviation is with 475 nm significantly greater than in the case of the convex lens. However the deviation within 80% of the lens diameter is lower: 258 nm; this shows that serious deviation happens towards the usually less critical rim of the lens. The roughness values are slightly down compared to the convex lens with $Rq = 26$ nm, $Ra = 20$ nm, $Rt = 150$ nm. The result of

Figure 50. Positively scanned concave lens etched at a fluence of 462 mJcm^{-2} resulting in an average deviation of 475 nm and $Rq = 26$ nm, $Ra = 20$ nm, $Rt = 150$ nm. Best fit ROC 57.5 µm.

the negatively scanned lens (Figure 51) confirms the findings from before as higher fluence still results in a shallower lens while parts of it are already over-etched. The overall deviation is with 1229 nm more than a micron. The surface quality is high with Rq = 8 nm, Ra = 6 nm, Rt = 37 nm.

Figure 51. Negatively scanned concave lens etched at a fluence of 507 mJcm^{-2} resulting in an average deviation of 1229 nm and Rq = 8 nm, Ra = 6 nm, Rt = 37 nm. Best fit ROC 69.4 μm.

With the modification to the surface profiler mentioned above it turns out to be a useful instrument to obtain quantitative data on the micro-lenses of interest. Taking the visual observations into account it is reasonable to trust the profiler data. Nevertheless it is recommended to make several scans with the profiler to ensure the needle tip runs through the centres of the lenses.

Now that we have been able to actually measure the lens profile and surface roughness, it can be said that the scan direction is critical in the SIS process. While the positive scan leads to a reasonably good match with the target profile, the negative scan cannot be qualified. It is interesting to see that the negative scan results in a much better surface

quality; this gives hope that the issue of the ring-like grating occurring in the positive scan can be resolved. Although the roughness of the lenses measured is relatively low, it is assumed that the ring grating is not acceptable for many applications; hence it will be given more attention below (cf. section 4.5).

4.4.2 Optical behaviour

Having analysed the lenses mainly geometrically the focus in now on their optical behaviour – after all it would be interesting to know if these structures actually do act as lenses!

Note that only the lenses that closely match the design are analysed regarding their optical behaviour.

E. Optical microscope with point source

The set-up for the initial test of the optical behaviour of the micro-lenses is relatively simple. A multimode optical fiber is installed more than 50 mm below the array and illuminated with white light. It may be considered as being effectively at infinity in an imaging sense and therefore considered as a point source. A Leica microscope is used and the lens sample with the convex lenses processed at 463 mJcm^{-2} is put onto a glass plate with the lenses facing upwards. The focal length is measured at ~100 μm above the lens confirming the radius of curvature as being ~60 μm since Polycarbonate has a refractive index of 1.58. Figure 52 shows 70 lenses and their foci looking at the focal plane through the microscope objective.

The spot sizes look the same for all 70 lenses in the image. The cross-like illumination between the lenses is non refracted light as the area between the lenses is more or less flat. Otherwise there is high contrast with little stray light. This is confirmed by inspecting the focal spot closer with a high magnification lens (20x) as shown in Figure 53. The figure shows a screen shot of in-house measuring software determining the spot

size. As the focal spots are small they nearly disappear beside the yellow lines of the measuring tool. The software measures a spot size of 1.72 µm and proves the high contrast with the sharp intensity rises in the measuring plots for the *x*- and *y*-axis underneath the picture.

Although this is a simple test, it shows that the lens is refracting the light and is able to concentrate the wave front into a small spot.
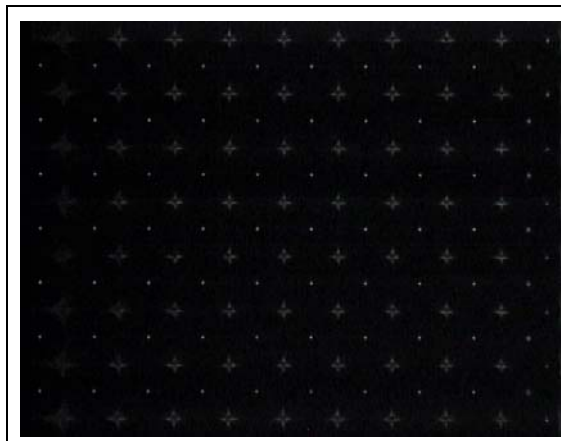

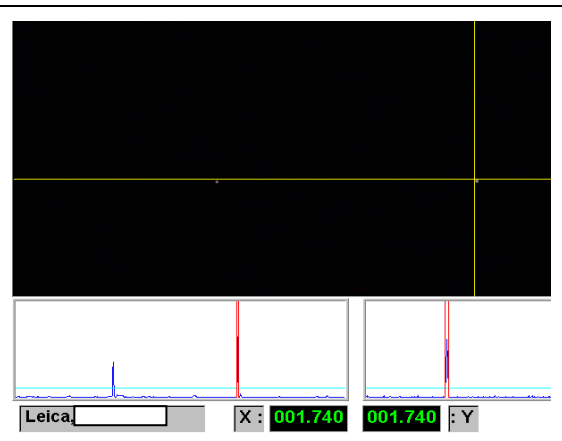| **Figure 52.** Image at focal plane of array. Note the cross-like illumination; this is the area between the lenses. Spot pitch is 100 µm. | **Figure 53.** Image at focal plane with two foci with a spot size of 1.74 µm. Distance between spots is 100 µm. |

The same set-up with a point source and a microscope is used to test the imaging capability of the lenses. A chrome-on-quartz mask with resolution patterns with line spacing of 1, 2, 5 µm dark and bright field was put underneath the lens array. Figure 54 shows the dark field mask without the lens array on top. Figure 55 shows the same mask
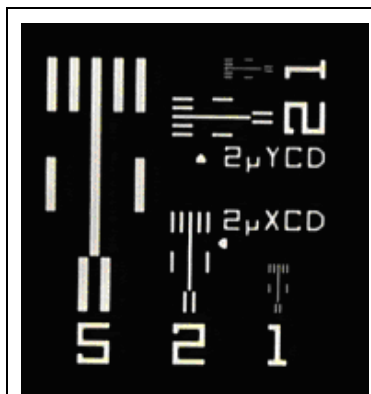

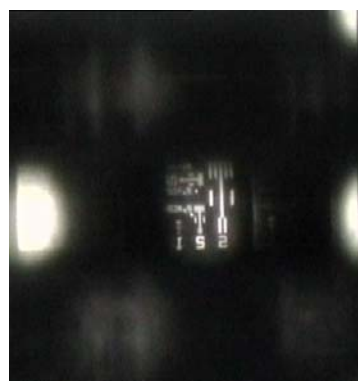| **Figure 54.** Line spacing object with line spacing of 1, 2, 5 µm. | **Figure 55.** Image at focal plane of micro-lens. Object, lens, image ratio results in a magnification of 0.4. | **Figure 56.** Image at the focal plane of the micro-lens shows that the micro-lens can resolve 1 µm line spacing. |

but 0.4 times magnified through one of the laser-etched micro-lenses. The image looks good and 5 µm line spacing de-magnified to 2 µm are still clearly resolved. The same is true for the image in Figure 56 where the imaged 1 µm line spacing pattern is nicely resolved, too. Even though this does not provide quantitative information it does provide visual confirmation that the micro-lenses produce excellent image quality and are capable of resolving at least 1 µm line spacing.

G. Refraction test of an individual lens with a 532 nm laser

It is striking that the ring gratings are strongly visible even though only 300 nm deep and that at the same time they do not seem to have a major influence on the imaging quality nor do they result in high Ra and Rq values. It can be said that the Ra and Rq values of not more than 60 nm are acceptable for direct laser-cut lenses. Nevertheless the strong visual appearance of the ring grating requires further investigation.

A special set-up with a low power green laser was rigged up to help better understanding of the optical effect of these gratings. Figure 57 shows the set-up to test the refraction behaviour of an individual lens. What is basically done here is focusing the Gaussian beam of a 532 nm laser with a spot size of 1.25 mm (HWHM, 80 mm after the laser exit) down to < 8 µm. The focus is centred on the back of one of the micro-
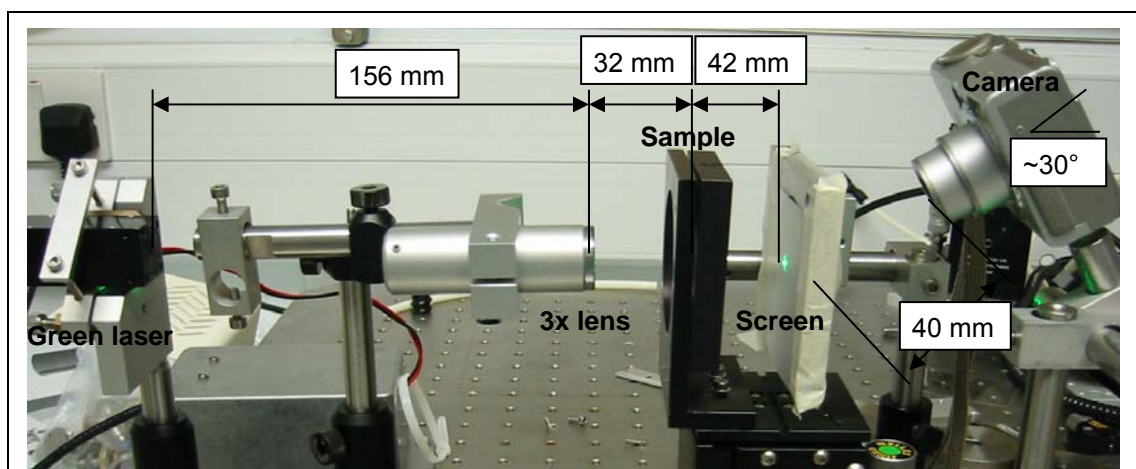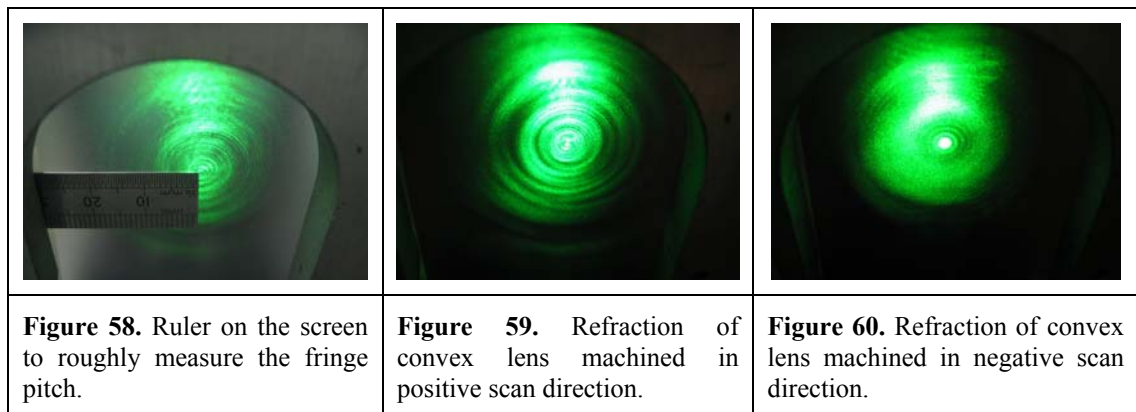

Figure 57. Set-up for refraction test of individual lens with laser emitting at λ = 532 nm.

lenses. A diffuser screen is placed at a distance of 42 mm from the lens array. To record the refraction pattern created by the tested lenses a photo camera is positioned 40 mm away from the screen under an angle of ~30°.

The main interest of this test is to investigate the influence of the ring grating, which is much more pronounced when the lens is scanned in positive rather than negative direction. Hence positively and negatively scanned lenses are put into the test rig. To give an idea of the size of the refraction pattern and the pitch distance between rings a photo with a ruler in front of the screen was taken (Figure 58). It can be seen that the smaller pitches are around 1 mm on the screen. Figure 59 and Figure 60 show the refraction of convex lenses machined in positive and negative scan direction, respectively. The difference between the two is obvious and confirms that the lens surface of the negative scan is smoother and has ring gratings only in the centre of the lens. However, the flat centre created in the negative scan generates a bright spot in the refraction pattern.

Figure 58. Ruler on the screen to roughly measure the fringe pitch.	**Figure 59.** Refraction of convex lens machined in positive scan direction.	**Figure 60.** Refraction of convex lens machined in negative scan direction.

With the positively scanned lens the ring grating causes intensity ripples on the screen; it looks like a magnified image of the lens itself. Although the surface roughness values are low, the ring grating is probably also causing the light to diffract, which is not good news especially if the lens array is used as an advanced diffuser film for rear projector screens or the like.

With this especially designed test it is possible to quickly verify if a micro-lens array has roughly the surface quality expected or not. Making the test more sophisticated by adding a device to accurately measure the intensity anywhere on the diffuser screen would allow getting quantitative data of the scattering losses of the lens and hence giving information about the overall surface quality and efficiency of the lens.

4.4.3 Interpretation of experimental results

How can the significant difference between a positive and a negative scan be explained? In section 2.3.3.4 the principle of the main SIS scan directions has been introduced and the topographical differences the pulse trains face have been explained. The assumption made here is that this is exactly what is responsible for the different results. While for the positive scan direction each subsequent aperture is imaged onto a previously ablated horizontal area, for the negative scan direction each subsequent aperture is imaged onto a more and more evolving 3D topography. This means ablation in one pulse happens on various z-levels (for this lens design, for the last pulse over 26.8 μm) and under various surface angles (here between 0° and 56° with the horizontal). From pulse to pulse the surface of a particular feature grows steeper and thus the illuminated area increases. Looking at the last pulse for a particular lens in a negative scan (biggest aperture) for instance, the surface it exposes is theoretically spherical (area: $2\pi Rh = 0.0101$ mm^2) and not a disc as in the positive scan (area: $r^2\pi = 0.0079$ mm^2, which is about 78 % of the former). And as the surface area increases, the fluence the surface is exposed to decreases from the first to the last pulse.

In addition to the loss in fluence the increase in wall angle with the horizontal will result in some energy being reflected, although previous results suggest that this effect does not have much influence with wall angles below ~50° [7]. Hence it should not influence the shape of the lens in question here. However, the decrease in fluence through the

increase of the surface area is a plausible explanation for the fact that the same process fluence does not result in the same structure depth for the positive and negative scan. Looking at the distortion of the lens machined in negative scan direction raises two other issues, which cannot be explained by the fluence drop. One is the flat top of the convex lens and the other the over-cutting of the spherical profile flattening it to a cone-like structure. For the flat top of the convex lens it is believed that debris accumulation during the lens etch process may be responsible. In the SIS process a lens is etched by scanning the whole image length over one position on the substrate. Hence while one lens is etched, it is exposed to the ablation debris caused by all other apertures in the mask pattern. In this specific case and considering only one row of apertures, each pulse that contributes to the formation of one particular lens ablates material for 128 other lenses at various stages at the same time and debris is generated at all the sites. When scanning in the negative direction, the top of the lens is ablated last but exposed to debris for the longest (128 pulses in this case). The top of the lens is naturally the area where the debris lands first; thus what happens is that debris coats the not-yet-machined top of the lens, the energy of the last few pulses is absorbed by the debris coat and leaves the Polycarbonate untouched. This hypothesis is confirmed by the result of an experiment where multiple rows of lenses are scanned at the same time and a high-pressure air jet is applied from one side of the ablation area. The air jet will carry the debris generated in the first row across the entire ablation area and naturally some of it will redeposit on the surface over which it travels. As the air jet blows across the surface, more and more debris is gathered and hence more debris will coat the surface. The more debris is deposited, the more energy is absorbed and the larger gets the flat area at the top of the lens. This can be clearly observed in Figure 61. The spots at the top of the lenses increase from the bottom of the picture to the top as indicated by the
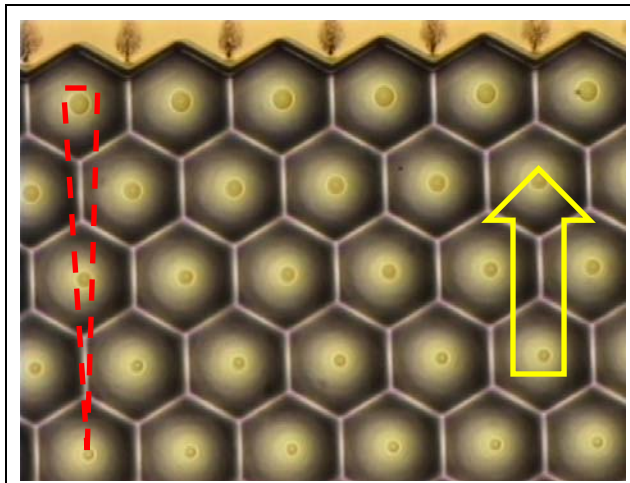
Figure 61. Influence of debris on flat area on top of convex lens. The yellow arrow shows the air jet direction, red wedge symbolises the increase of the flat area at the lens top. The flat area increases the further away the lens is from the air jet nozzle.

red dashed wedge, and the air jet was applied from the side where the small spots are as indicated by the yellow arrow.

The over-cut of the lens observed when scanning the lens in the negative scan direction can possibly be explained by the fact that every laser pulse has to embed the already etched structure deeper into the substrate; hence the profile is loosing shape in the process.

A puzzling feature is the appearance of the ring grating on the lens surface. As it seriously affects the quality of the optical structure, further tests were carried out to be able to investigate and understand the cause of the grating. These tests are presented in the following section.

4.5   Investigations into the ring grating

Although the geometry, the surface roughness and the optical quality of the lenses processed in the positive scan direction are relatively good, the ring grating on the lens surface clearly presents a problem. The following is an investigation into why and how the ring grating is created at the lens surface.

The expectation is that the grating is directly linked to the sizes of the aperture in the mask. A look at the 3D data plot of the WLI of the central part of the lens in Figure 62 seems to confirm this assumption, but the *x*- and *y*-profile in Figure 63 does not show clear evidence for it as the grating is rather periodical.

Figure 62. 3D data plot of the WLI of the central part of the lens processed in positive scan direction.	**Figure 63.** Profile measurement of central part of the lens processed in positive scan direction.
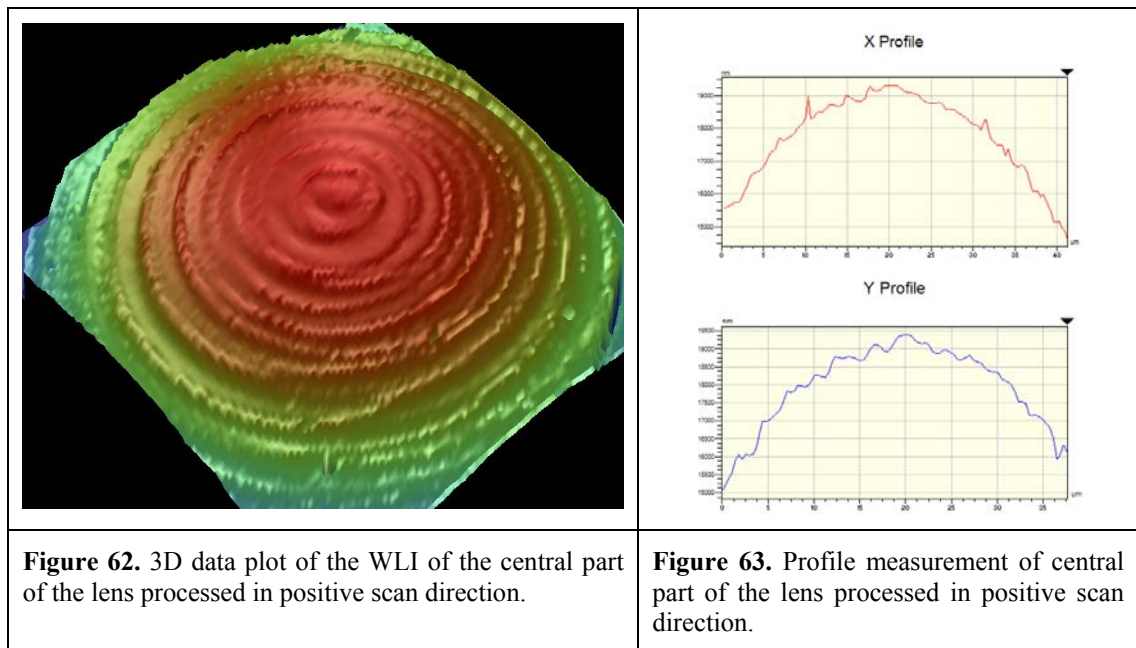
To get a better understanding of what is happening an additional test is carried out. In this test a series of apertures is scanned as when creating the lens itself, but with bigger differences in the aperture diameters between subsequent apertures and with far fewer shots.

4.5.1 Discussion of the steps

Figure 64 shows a WLI data plot of a positive scan with 6 pulses at 0.4 Jcm^{-2}. Figure 65 shows the *x*- and *y*-profile plot of the structure. What is striking is that although a step profile with constant step height and constant ablation depth over most of the ablation area is achieved, there are relatively deep grooves and high burs on every edge of the ablation area (see Figure 64 and Figure 65). This is something not anticipated in the ablation model applied so far, where the assumption was that each laser pulse would ablate a shallow cylindrical volume with diameter equal to that of the imaged apertures and height corresponding to the fluence applied everywhere within the exposed area.

Zooming in on the steps reveals that at 0.4 Jcm^{-2} the grooves and the burs both are around 100 nm high or deep respectively. This is 50% of the nominal step height in this case.
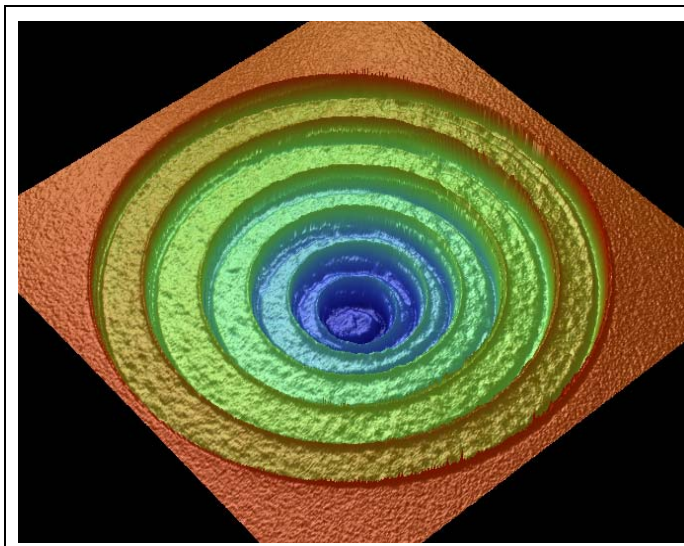
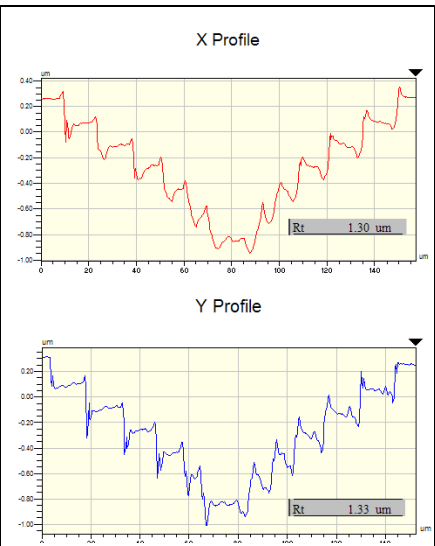**Figure 64.** Ablation of 6 apertures at 0.4 Jcm^{-2}.

Figure 65. x- and y-profile of structure.

There are suggestions that the groove is caused by diffraction effects at the binary aperture, the so-called dog ears. In order to explain the grooves with this theory the intensity raise at the edge of the beam would need to go up to 1 Jcm^{-2}, which is 2.5 times the nominal fluence of the rest of the beam. The same experiment carried out at 1 Jcm^{-2} results in grooves of 260 nm depth, while the step height is 290 nm; this corresponds to 90% of the step. To explain this depth with an intensity rise at the aperture edge would suggest that the fluence at that point is ~8 Jcm^{-2}.

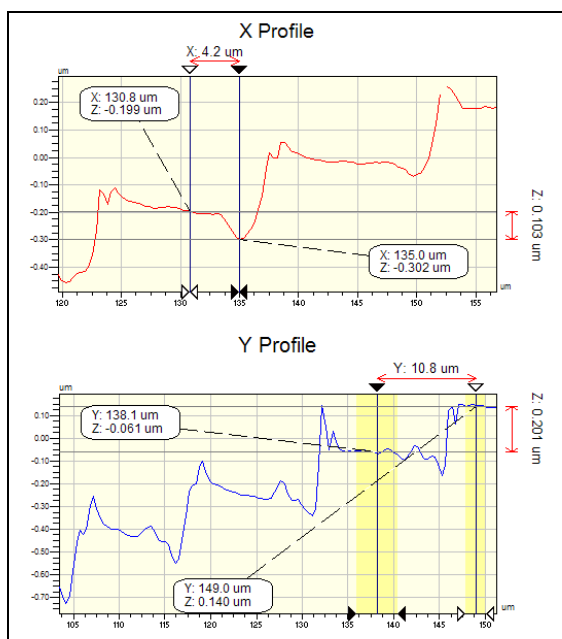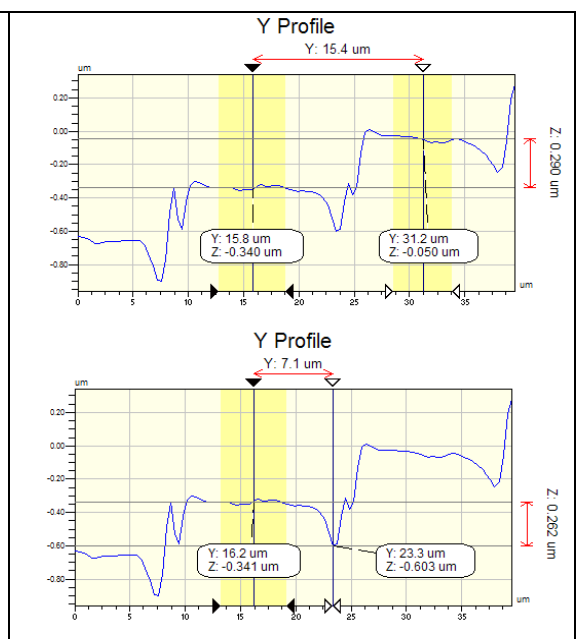**Figure 66.** Step – groove ratio at 0.4 Jcm^{-2}.

Figure 67. Step – groove ratio at 1 Jcm^{-2}.

Beam profiles taken at the image plane did not reveal a higher intensity at the edge of the aperture; but as the region is relatively small, this could also be due to the limited resolution of the beam profiler. To be certain more measurements would be needed. However, the findings here point rather to a cause other than the diffraction effects at the edges of the binary apertures although these may play a part in it.

Assuming that the ablation process is mostly thermal the groove could be explained by a rise in pressure as the expansion of the vaporised and liquidised material is stopped at the edge of the exposed area. That the increased pressure has a bigger effect perpendicularly than laterally could be explained by the fact that the energy in the pulse is absorbed beyond the ablation depth and weakens the molecular bonds, hence higher pressure and heat in this region could be responsible for the groove.

The fact that a bur is created, too, supports the hypothesis that the nature of the ablation is rather photo-thermal than photo-chemical. It is difficult to think of another process which would result in such a sharp pointing ridge built up on the edge of the previous step. Unfortunately it is beyond the scope of this investigation to get high speed images of the ablation process to prove that the bur crown is created by quasi-liquidised material pushed up by the expelled material. Nonetheless this seems a plausible explanation for the creation of the bur around the edge of the previous ablation step.

Instead of a simple step at the ablation edge a close look reveals rather a zigzag profile.

A simplified parameterisation of the groove is shown in Figure 68: a is the step height, b the groove depth, α is the step slope angle and β the groove slope angle. When applying a fluence of 0.4 Jcm^{-2}, the following values are determined

Figure 68. Simplified parameterisation of the etch profile.
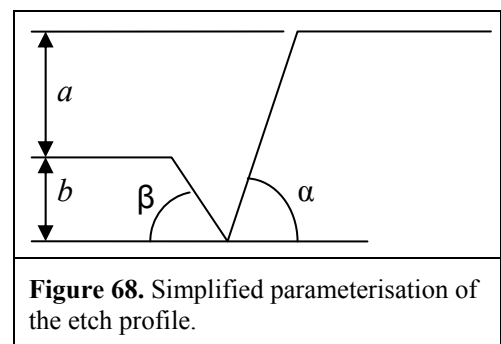
for these parameters: $a = 200$ nm, $b = 100$ nm, $\alpha = 12°$, $\beta = 4°$; for a fluence of 1 Jcm^{-2}

we find a = 290 nm, b = 260 nm, α = 15°, β = 10°. The bur, which is not included in this parameterisation, is typically 140 nm high and 2 μm wide.

These findings show that instead of a nicely defined cutting edge there is a groove-like undercut and a ridge-like elevation for every aperture imaged. This seriously affects the quality of the etched 3D micro-structures. Going back to Figure 62 with this in mind and looking carefully it is possible to actually see some of the burs on the lens surface. The grooves are more difficult to identify, but the waviness is obvious. Looking at the ablation edge it is in a way surprising that despite the grooves and burs it is still possible to achieve a reasonable structure profile. Nonetheless if it is taken into account that grooves and burs are both small compared with the lens and that they do occur consistently and even cancel each other out under certain circumstances, the close profile match can be explained.

4.5.2 Comparison between the positive and the negative scan

Repeating the same experiment but with a few more apertures and scanning in both, positive and negative, scan directions does further confirm that the ablation is most likely governed by a photo-thermal process. While a typical result of a positive scan as shown in Figure 69 reveals a step structure from top to bottom, the sequentially growing ablation area in the negative scan is washing out the previously ablated steps more and
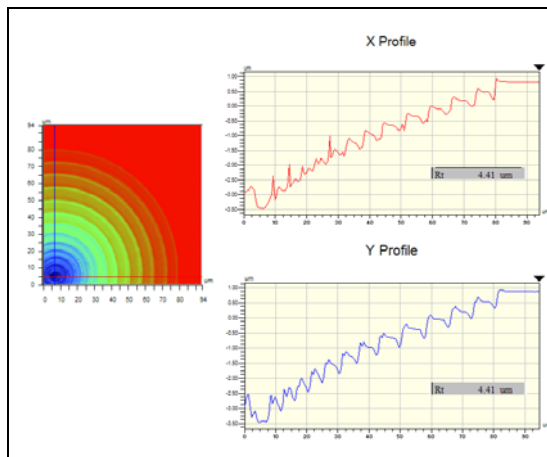

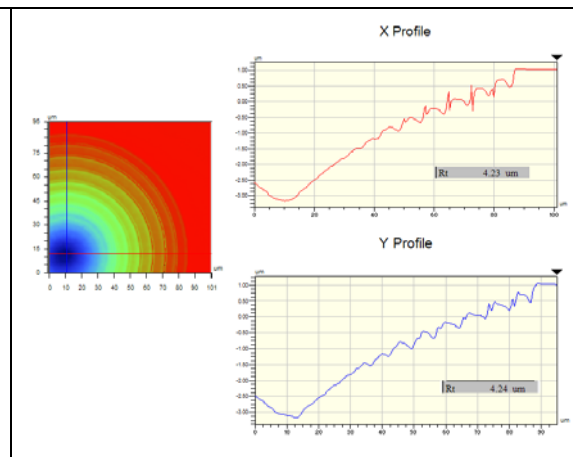|	
Figure 69. Few shot positive scan.	**Figure 70.** Few shot negative scan.

more, resulting in a rather smooth surface (see Figure 70). The fact that the laser pulses exposing the already structured surface act like a low pass filter is pointing strongly towards a thermal process; the high frequency peaks and valleys basically reflow to a straight surface. In Figure 70 it can be seen that already after 8 pulses at 1 Jcm^{-2} the steps are completely flattened.

In other words we have observed that away from a step edge laser ablation of Polycarbonate at 248 nm wavelength results in itself in a low surface roughness and even has a polishing effect. From this we may conclude that rough Polycarbonate surfaces can be made smooth by exposure to a few pulses at 248 nm. This is obviously very interesting as this chapter has revealed that it is possible to laser etch 3D structures that match their target profile quite well but disappoint in the surface quality. The prospect that with a post-process exposure the surface quality can be enhanced is very attractive as it promises the capability of producing high-quality micro-features meeting industrial requirements in respect to geometry as well as surface roughness. As this is critical for the overall quality of micro-structures, chapter 6 will further investigate this matter.

4.6 Conclusions

The well-known ablation curve (ablation depth versus fluence) and some considerations about ablation efficiency determine the slice thickness as the basis for the SIS mask design. The designed micro-lens is sliced accordingly and the cross-sections thus obtained define the apertures. These apertures are linearly arrayed at the pitch of the micro-lens array starting with the biggest and ending with the smallest to give the option of two main scan directions as defined before (positive if scanned from big to small and negative if scanned in the opposite direction). The whole array of apertures is then magnified to account for the demagnification of the projection lens.

Exactly this has been done in the experiments described above. The results are clear: while the positive scan direction results in a reproduction of the target shape within an average lens distortion of less than 300 nm, the negative scan does not really etch a lens as the deviation is too big; nevertheless it results in a better surface finish. Although the *Ra* and *Rq* values for the positive scan are around $\lambda/10$, a clear ring grating is visible and the *Rt* value of around 300 nm is relatively high.

In this study it was discovered that it is as big a challenge to evaluate the micro-lens as it is to create it. Having employed many different techniques to measure and analyse the lens structure, we can conclude that there is no single technique that gives all the answers. To analyse the structure as well as possible a combination of metrology techniques is required. Whilst visible observation with a standard optical microscope and the use of an SEM provide a good sense of the general quality of the micro-lens array, these cannot give quantitative data. The white light interferometer fails to measure the whole lens as not enough light is reflected off the steeper slopes of its profile. It is therefore not a qualified means of measuring this type of micro-structure. If equipped with the right stylus, camera and compensation for arc movement of the needle, the stylus profiler can deliver and produce a useful set of quantitative data. Testing the optical behaviour of the micro-lens array by simply measuring the focal length and spot size plus observing the quality of an imaged resolution pattern provides a good indication of the performance of the lens but it is not fully conclusive.

As our analysis of the laser-etched micro-lenses in this chapter has shown, the conventional methods give reasonable values for the surface and imaging quality and only a customised set-up with the refraction analysis can highlight the seriousness of the ring grating. As the range of micro-structures that can be created by SIS is so wide, it may be beneficial and is often necessary to find a customised way of analysing a

specific behaviour of the structure under consideration. Nonetheless the modified surface profiler qualifies itself as the most versatile metrology technique employed here because it can actually quantify the profile of the structure regardless of whether it is an optical structure and whether it is machined into an optical or non-optical material. TWyman-Green interferometry (TWG) and Digital Holographic Microscopy (DHM) are two other optical measurement techniques that are used to test micro-lenses [8] or other 3D micro-structures [9]. Unfortunately this equipment is not available for this work.

---

1. S. Sinzinger, J. Jahns, Microoptics, Wiley-VCH (1999)

2. S. Kuper, J. Brannon, K. Brannon, Appl. Phys. A 56, 43 (1993)

3. S. Kuper, M. Stuke, Appl. Phys. B 44, 199 (1987)

4. B. Hopp, Zs. Bor, E. Homolya, E. Mihalik, Appl. Surf. Sci. 109/110 (1997)

5. C.-R. Yang, Y.-S. Hsieh, G.-Y. Hwang, Y.-D. Lee, J. Micromech. Microeng. 14 (2004)

6. M. Zecchino, Veeco handout, AN526-2-0405

7. A.S. Holmes, J.E.A. Pedder, K.L. Boehlen, Proc. SPIE Vol. 6261 (2006)

8. S. Reichelt, H. Zappe: Appl. Opt. 44, 27 (2005)

9 J. Kühn, E. Cuche, Y. Emery, T. Colomb, F. Charrière, F. Montfort, M. Botkine, N. Aspert, C. Depeursinge, Proc. SPIE Vol. 6188 (2006)

5   Artefacts created when machining positive/convex arrays

5.1   Introduction

As shown before with SIS it is possible to cut positive/convex and negative/concave structures. While machining negative/concave structures the edge of the image can be positioned in such a way that it coincides with the surface top. Hence only minimal ablation happens where two scans join. The opposite is true when machining positive/convex features; here the image edge is often at the foot of the feature where most material is removed. The consequences of this and measures to avoid the resulting unwanted machining artefacts are discussed in this chapter.

5.2   Theoretical and pre-experimental considerations

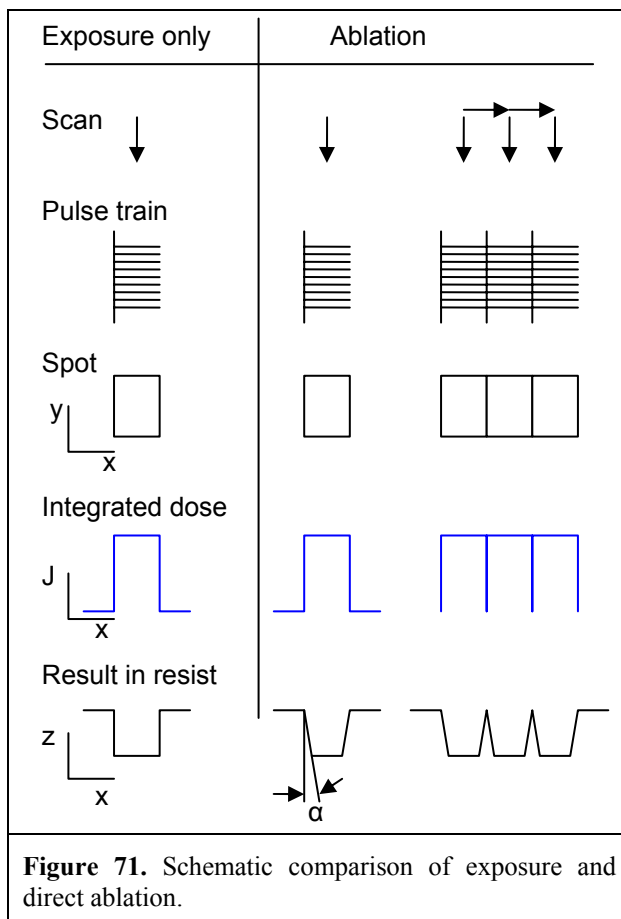### 5.2.1   Wall angle limits by direct ablation with a given optical set up

The minimum wall angle[2] achievable of the ablated site is mainly dependent on the material, the fluence and the NA of the imaging system [1,2]. The optical system used in most of the experiments described here is established and it is not easily changed without significant trade-offs on other parts of the process. Hence it can be assumed that the imaging system stays the same and therefore the NA is fixed. Keeping Polycarbonate as the material of choice the only parameter left to influence the minimum wall angle achievable is the fluence. To achieve vertical walls with an NA of less than 0.1 and using a telecentric lens the fluence would need to be in excess of 1.3 Jcm^{-2}. From an application point of view it is disadvantageous to use such a high fluence: first laser ablation gets less efficient with higher fluence, and second the lifetime of the optics is shortened considerably at this fluence level. Taking this into account it can be said that for industrial use of SIS 1 Jcm^{-2} is a reasonable upper limit

---

[2] Measured with the vertical as defined in subsection 2.3.3.1.

for the fluence. Tests on the system showed that at 1 Jcm^{-2} the steepest wall achievable in Polycarbonate has a positive angle of ~4°. This is a physical limit which cannot be overcome without changing the optical configuration.

 This fact has direct consequences for the machining of 3D features. It is obvious that it imposes restrictions on the possible feature designs as is not possible to machine any parts of an individual feature with a wall steeper than this minimum. Nevertheless it is still possible to produce a large variety of features; and in the case of optical features like refractive lenses and reflectors there are usually no steep walls involved as at these angles most of the light would be internally reflected.

 A more severe issue is observed when machining convex or upstanding structures. As mentioned before SIS cuts the structures in a linear array, line by line. Convex or upstanding features are therefore machined in a groove with a wall to one side rising from the bottom of the feature to the top surface of the substrate, and the angle of this wall is limited to the minimum angle mentioned above. This will become a significant issue when a seamless area larger than one scan is required. There are reports of photolithography laser systems which expose large areas of resist seamless in scan mode [3]. However, those findings cannot be applied to direct ablation of deep features as we discuss it here.

Figure 71 shows the significant difference between exposure only and

Figure 71. Schematic comparison of exposure and direct ablation.

ablation with a wall angle limiting setup when a simple rectangular laser spot is scanned over a resist. The scan direction, pulse train, laser spot, the integrated dose and the result in the resist is shown in Figure 71. The difference between exposure only and direct ablation is that in the case of ablation a wall angle α is created. This wall angle α has severe consequences when a large area should be covered with multiple scans. Instead of ablating the whole scanned area to the same z-level a wedge-like seam remains between scans even though the integrated doses are stitched together nicely.

To further investigate this wall angle issue without being distracted by complex 3D features, we use a prism profile as a basic example. Figure 72 shows the spot geometry (i.e. the shape of the aperture array rather than individual apertures) to cut a prism profile according to standard SIS mask design (top), the integrated dose (middle) and the expected result in resist by direct ablation (bottom); the expected result is shown as a qualitative sketch and derived from the ablation model used before. It can be observed that the profile is accurately represented in the substrate but for two exceptions: the walls that should be vertical show a slight angle and the features next to these walls are not machined down to the same z-level as the others.

Figure 72. Spot geometry (top), the resulting profile in the material (bottom) and the integrated energy dose (middle) are represented. On the left hand side an individual scan is represented, whereas two scans side by side are shown on the right hand side. Although two scans of the integrated doses are stitched together nicely resulting in a continuous profile, the expected ablation result will have a distinct ridge between the scans.

Scanning one line, stepping the image pitch and scanning the next is expected to result in a distinct ridge between the two scans and to distort the features next to it even though nothing in the profile of the integrated dose adverts to this. The ridge will be a wedge-like feature with a full angle equal to twice the maximum wall angle and the same height as the rest of the profile. This unwanted feature is likely to either jeopardise the optical performance of the array or be visible to the human eye as a regular pattern or both.

When tackling this issue, two things have to be considered: one is eliminating the ridge and the other is generating a continuous profile from scan to scan. It could be argued that getting rid of the ridge is all that is needed and that it should not be too difficult to ablate the ridge in a post-process. However, merely removing the ridge does not address the fact that the wall angle issue also distorts the features next to the would-be vertical wall [4]. Hence the way forward is rather not to create a ridge in the first place. In a
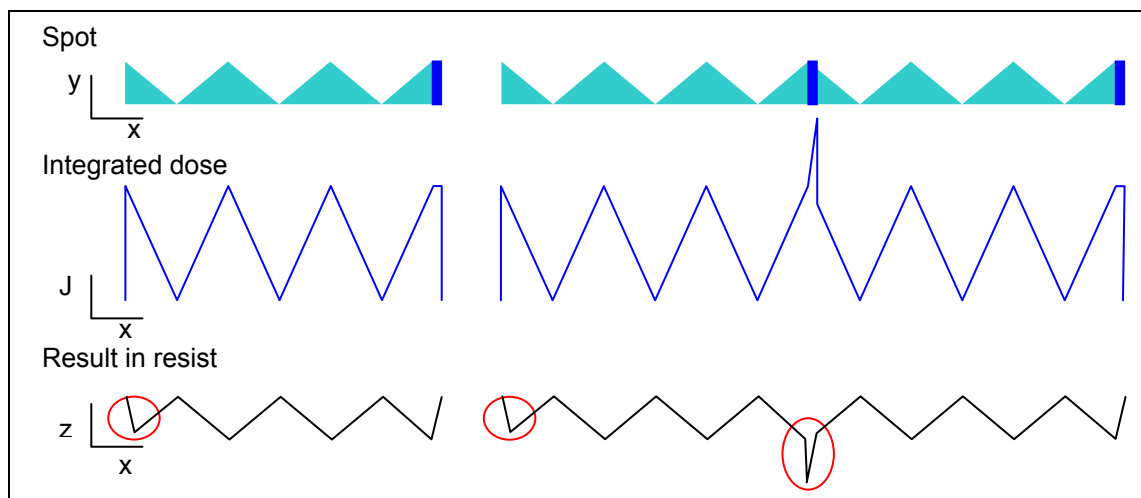

Figure 73. Spot geometry (top), resulting profile in the material (bottom) and the integrated energy dose (middle) are represented. On the left an individual scan is represented; two scans side by side are shown on the right. The spot pattern geometry is extended by a small rectangle (dark). Looking at the integrated dose a peak of excess energy appears where the two scans join. This excess energy is responsible for a relatively deep groove at this position.

first approach a simple rectangular extension of the spot geometry with a width corresponding to the base extension of the side wall slope is considered as illustrated in Figure 73.

The consequence of extending the image but still side stepping an integer multiple of the prism pitch is an excess of energy where the scans are stitched together. This is already obvious when looking at the integrated dose.

The assumed ablation result has indeed no ridge but a groove instead as the excess of energy is expected to remove too much material. In certain applications this is preferable to a ridge but it represents nevertheless a discontinuity in the prism profile. In order to create neither a ridge nor a groove a third approach to the mask pattern design is investigated.

If the goal is to achieve a continuous structure the total amount of energy at the joint between scans should be equal to the equivalent point within the image. This means both edges of the image need to be considered, and one edge of the image must be complementary to the other one. Both image edges need to be designed to match the step-and-scan process and address the wall angle issue at the same time. A continuous profile of the integrated dose alone is not enough. A possible approach is to design the mask pattern in such a way that it etches a slope above the minimum angle on one edge of the scan. This means that one edge of the mask pattern is designed in such a way that
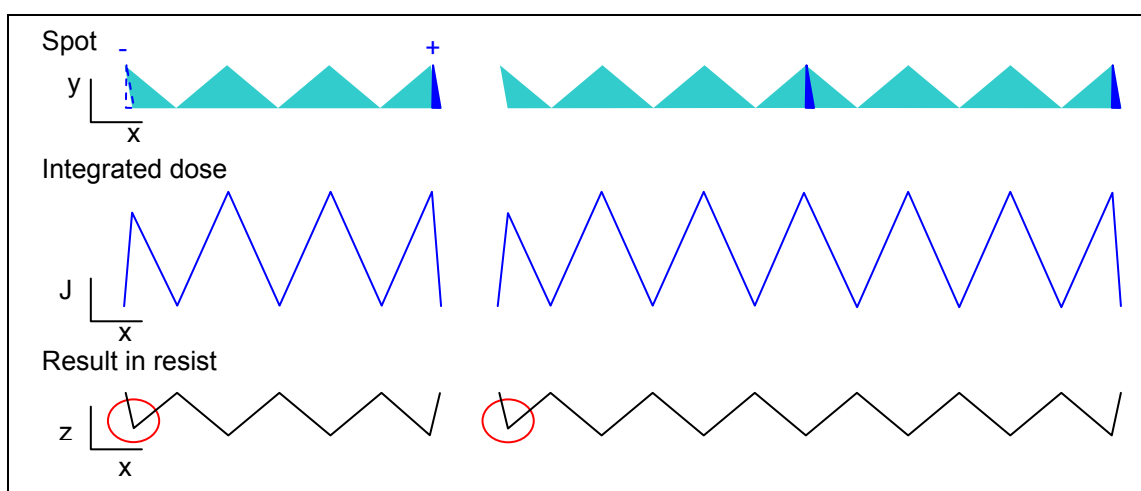

Figure 74. Spot geometry (top), the resulting profile in the material (bottom) and the integrated energy dose (middle) are represented. The spot geometry shows that the wedge added on one side is subtracted on the other. Hereby it is ensured that the integrated energy dose is correct and a seamless profile can be expected as the ablation result. The only expected misrepresentation of the profile will be at the edge of the first scan.

part of the prism that will be completed by the following scan is already machined. In order to avoid excess energy where the scans are stitched together what is added on one side needs to be removed on the other. Figure 74 (top left) shows the laser spot where the energy level is reduced on the left to compensate for the extra energy on the right (indicated by a plus sign). In the scanning process the integrated doses join without gap or peak to achieve a continuous profile. This profile is theoretically seamlessly transferred into the workpiece (bottom right). The trade-off is that the very first feature of a scanned area is not cut to full depth because of the reduction in energy in this mask area.

From these discussions it can be concluded that with the right considerations it should be possible to design SIS mask patterns which compensate for the wall angle limitation of the optical system and its negative consequences on features and artefacts in the scan area.

5.2.2 Influence of exposure sequence on mask pattern design

Above we have considered a difference between exposure only and direct ablation regarding the wall angle; a further difference between these two methods shall be discussed here in respect to the extended and reduced mask edge. As in chapter 4 it is important to acknowledge that the exposure sequence (scan direction relative to the mask geometry) can influence the result even though the point of interest is only located at the mask edge. This is even more critical as often the wall angles considered are in the regime where the angular dependency [5] of ablation can play an important part.

Because of the creation of a physical topography, which influences the ablation of the subsequent pulses, the order of the exposing beam geometry will most likely influence the resulting shape or profile. To illustrate what needs to be considered when designing a mask pattern for seamless scans the zigzag profile from above is simplified again to a
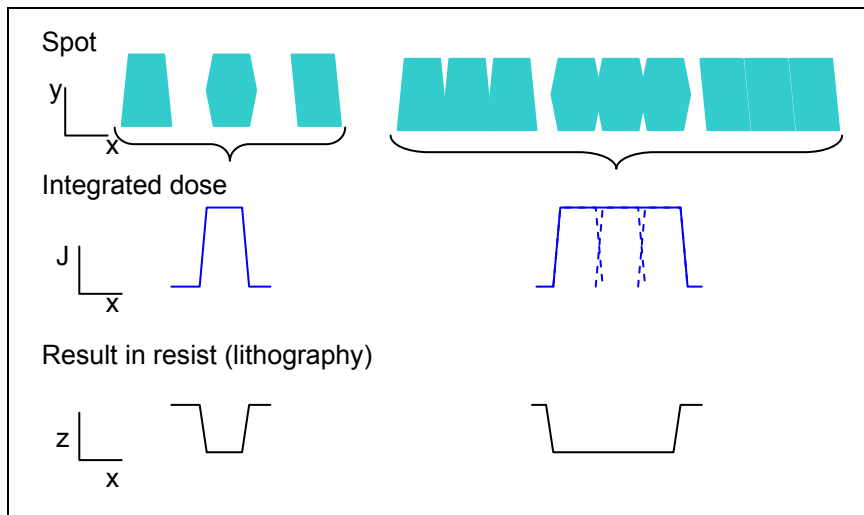
Figure 75. Illustration of resist exposure in thick film lithography followed by development and etching. Exposure spot (top), the resulting profile in the material (bottom) and the integrated energy dose (middle) are represented. It is shown that the geometry of the spot can vary without effect on the result as long as the integrated dose is the same.

channel. The findings from above can in principle be implemented as shown in Figure 75 where three different spot or mask pattern geometries (top) are suggested. All three geometries give the same integrated dose and are expected to yield the same result in resist in a lithography process. But is this also true for direct ablation? To answer this question further investigations on what happens at the mask edge follow.
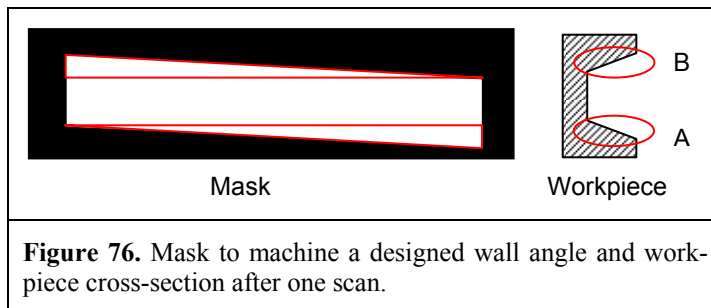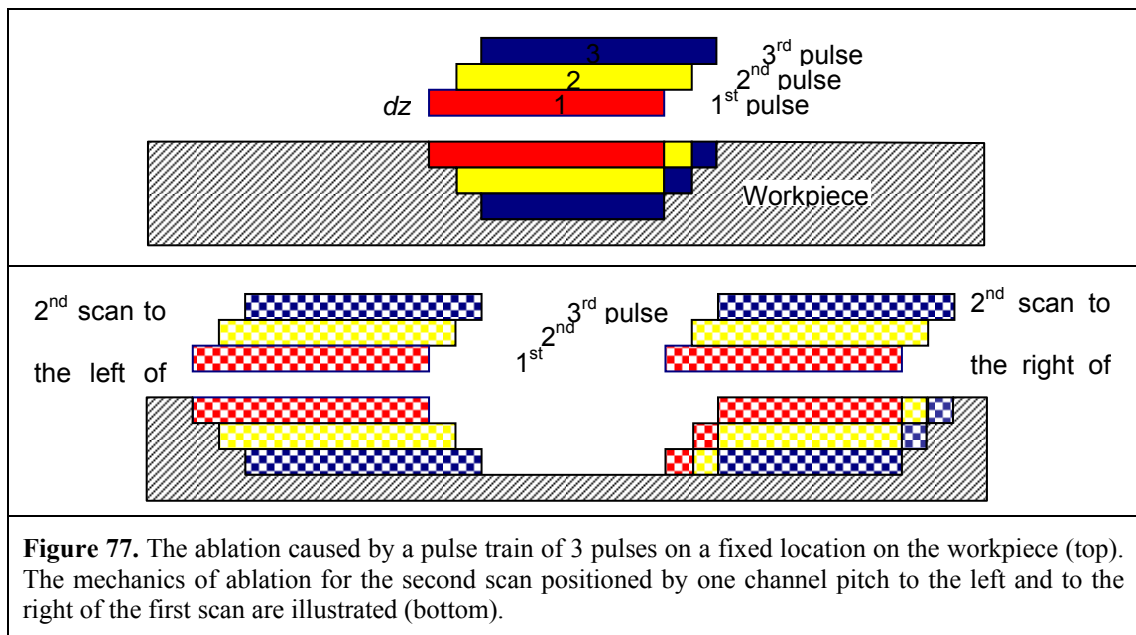

Figure 76. Mask to machine a designed wall angle and workpiece cross-section after one scan.

If the parallelogram like spot is chosen, a suitable mask could look like the one shown in Figure 76. If the resulting image at the workpiece has the same orientation as the mask and is dragged from left to right, for wall (A) of the workpiece the scan direction is positive while for wall (B) it is negative. Figure 77 (top) illustrates in more detail the difference in ablation between the two sloped image edges. It shows the ablation caused by a pulse train of 3 pulses on a fixed location on the workpiece; the pulses are offset with respect to each other because the workpiece is in continuous translation hence is exposed with different parts of the spot geometry. This is a very simplistic view, but it is good enough to understand the basic influence on the sequential ablation. What can be seen is that on the left hand side of the channel

Figure 77. The ablation caused by a pulse train of 3 pulses on a fixed location on the workpiece (top). The mechanics of ablation for the second scan positioned by one channel pitch to the left and to the right of the first scan are illustrated (bottom).

each pulse ablates one step on a constant *z*-level. On the right hand side each pulse ablates material over the *z*-range = $n * dz$ where n = current number of pulses and *dz* is the ablation depth per pulse. This means that the further the structure develops in *z* the more the fluence is reduced as the incoming energy is spread over the entire slope. Hence it can be expected that all the aspects discussed in chapter 4 about the negative scan direction can be applied here. Hence it can be predicted that the slope on the right will be distorted in respect to its design.

The bottom illustration in Figure 77 shows the mechanics of ablation for the second scan positioned by the channel pitch to the left and to the right of the first scan. What can be observed is that by positioning the second scan to the left of the first one ablation happens again on a constant *z*-level, in this case over the full lateral length of the pulse. Therefore the expectation is that the target geometry of the structure to be ablated can be matched. However, placing the second scan to the right of the first scan shows a different picture. In this case both edges of the ablated geometry follow the rule that material is ablated over the *z*-range = $n * dz$. In these circumstances it is again true that it is much more difficult to predict what the resulting structure will look like.

Nevertheless the first case where the second scan is placed to the left of the first one shows theoretically a good prospect to achieve a satisfactory result. This means that not only the scan direction of a mask pattern is determined as established before but also the direction of the step from scan to scan.

It can be concluded that by structuring an area *x* times the image width the very first row will have distorted features and the wall angle will not match the design. In practice this is not of big concern as there are many scans to cover an area, and it is usually possible to trim the edges of a processed area to cut off any distorted features in the first scan.

5.3   Experiments machining channels and prisms

5.3.1   Design of experiments

The plan for the first experiment is to use a simple mask like the one shown in Figure 76 and to drag the image over the workpiece thus machining a channel. The channel was designed to have a wall angle of 24° and a depth of 27 μm. The goal of this first experiment is to inspect the machined walls on the left and right of the channel and to compare the result with the designed geometry. The same mask is then used to machine a channel twice the width of the image to see if the ridge between scans is indeed avoided and the assumptions from above are in agreement with the practical results.

Further a set of experiments is carried out to verify if the propositions made in subsection 5.2.1 regarding the prism patterns are valid or not. A chrome-on-quartz mask without compensation, with rectangular compensation and with slope compensation has been designed and manufactured to demonstrate all three cases. The mask pattern has been designed to produce a profile as above with prisms of 90° on a 60 μm pitch, hence 30 μm deep. The ablation depth per shot is chosen to be 214 nm resulting in 140 shots

to reach the 30 µm depth; the corresponding process fluence is 425 mJcm^{-2}. With a laser trigger pitch of 100 µm the image length is 14 mm.

The mask is installed on the system introduced in chapter 2. Single as well as four scans side by side are carried out with each pattern. The processed samples are then cleaned and cross-sectioned using liquid nitrogen. Additionally the profile is measured with a surface profiler employing a stylus with a 40° tip and a radius at the tip of 0.7 µm.

5.3.2 Results of experiments

5.3.2.1   Channel with sloped walls

The first results are achieved using a simple channel mask and machining a 27 µm deep channel with one scan into Polycarbonate. Figure 78 shows an SEM picture of the cross-section where the scan direction for the triangular image edge is positive (left hand side of the channel). It can be seen that the slope is straight and clearly defined. The wall angle is 24° within one degree. There is a small overcut of ~1.5 µm depth at the bottom of the slope. In contrast Figure 79 shows an ill defined slope with an angle of 30° and a relatively big radius at the bottom. This is the side wall of the channel machined with the triangular image edge scanned in the negative direction.
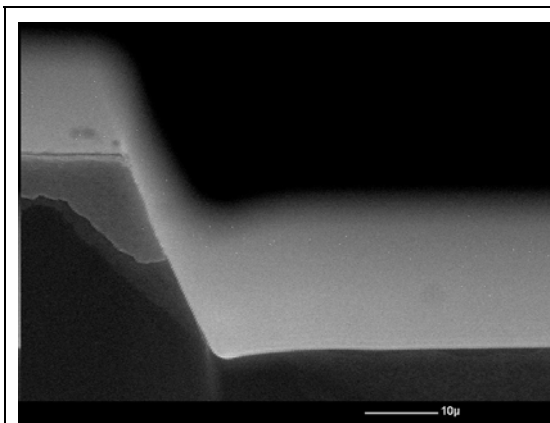

Figure 78. SEM picture of the positive scan direction side wall of a channel (left hand side of channel). The wall angle is within one degree of the design (24°) and the slope is straight. There is a slight overcut visible at the bottom of the slope.
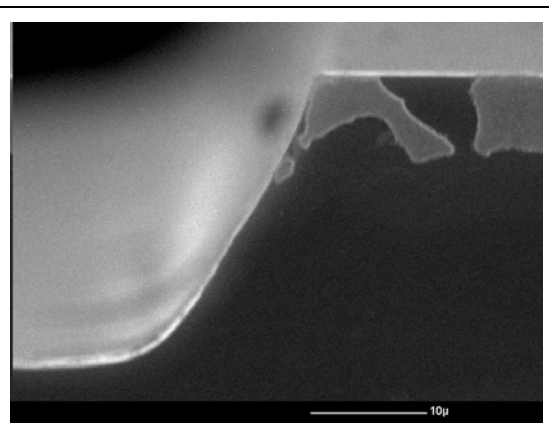
Figure 79. SEM picture of the negative scan direction side wall of a channel (right hand side of channel). The wall angle is 30° instead of 24° and the slope is curved with a big radius at the bottom. There is a strong deviation from the design.

Having looked at the resulting walls of the channel the focus in now on the ultimate question: is it possible to get rid of the ridge or seam issue? To answer this question the same channel mask as before is used to machine another channel but this time twice the width achieved by two scans separated by the image width. The second scan is positioned alongside the well defined wall (the one machined in the positive scan direction of the triangular image edge). Figure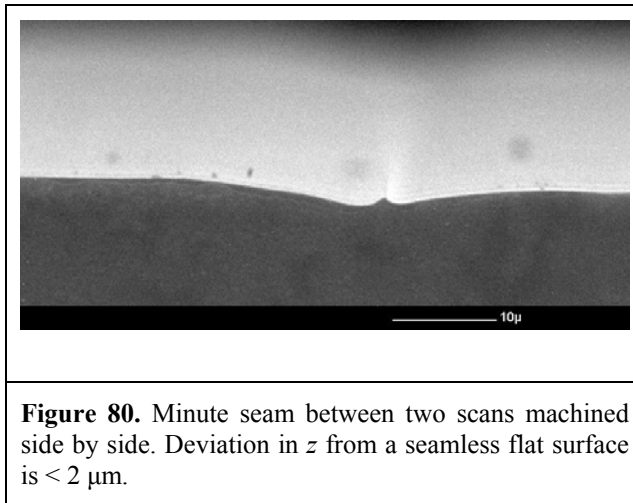 80 is an SEM picture of the region where the two scans join. Although a seam is clearly visible it is minute and the deviation in *z* from a seamless flat surface is < 2 μm. To study the creation and deletion of the seam in more detail and to see what happens to features next to it tests are run with the prism structure design described above.

Figure 80. Minute seam between two scans machined side by side. Deviation in *z* from a seamless flat surface is < 2 μm.

5.3.2.2 *Prism structure without compensation*

The first set of experiments was carried out with a mask pattern without compensation. Figure 82 shows a cross-sectional view of the result of scanning the mask image once over the Polycarbonate surface. Three relatively well-cut prisms can be seen; the resulting depth is 31 μm. Figure 81 shows that the centre prism is close to the design.
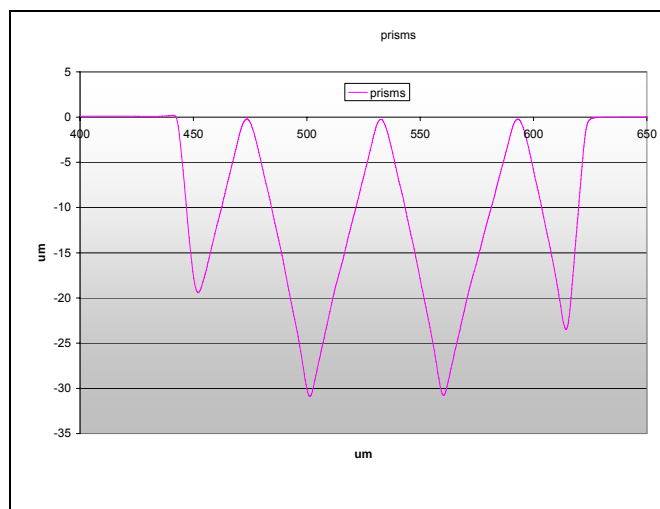
Figure 81. Stylus profiler measurement graph of one scan with no seam compensation. The depth and the wall angle on either edge of the scan are not correctly measured because of the physical dimensions of the stylus.

However, the focus of these experiments is on the seam / ridge and not on the geometrical detail of the prisms themselves. The results are rather qualitative than quantitative, especially as the standard measuring systems used in this thesis (e.g. stylus profiler) are not capable of determining some of the very small details of the ablation result. This is explained by the fact that the same stylus profiler as in chapter 4 is used with a tip angle of 40°; hence it is not possible to measure slope angles less than 20° nor narrow slits. For a better qualitative analysis SEM and optical microscope pictures are taken.
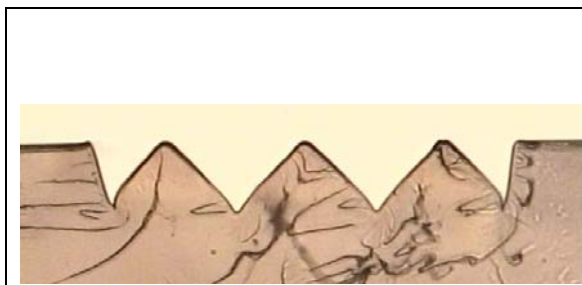

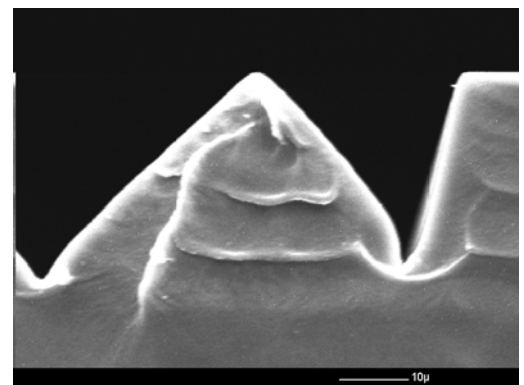|	
Figure 82. Cross-sectional view of the no-compensation pattern machined in one scan into Polycarbonate.	**Figure 83.** Close up of ablation result on one edge of the no-compensation mask design image.

It is clearly visible that as predicted the wall on either edge is not vertical. The wall angle is ~12° and the height is ~27 μm instead of 30 μm. Furthermore, there is an effect not expected shown in a close-up in Figure 83: an excess of ablation at the base of the prism affecting the representation of the designed shape. It is believed that the material in question is ablated by energy reflected by the relatively steep wall acting like a mirror for the incoming energy.

There is a general agreement between the prediction above and the result here and a strong ridge is expected if the replacement for the second scan is the full image width. Figure 84 shows an SEM picture of a cross-sectional view of part of a prism array machined with the mask without compensation. The result shows the expected ridge
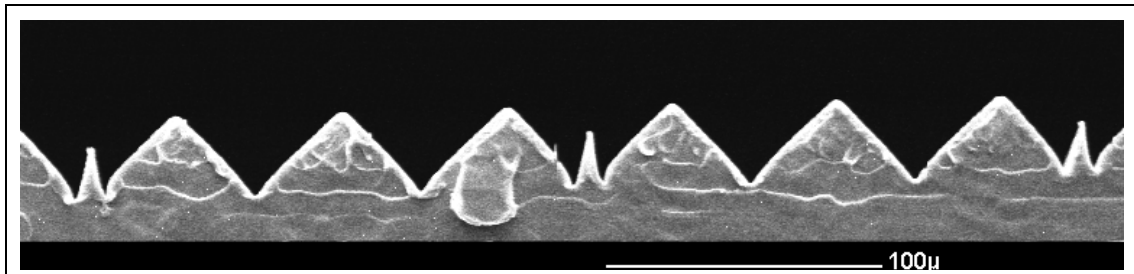
Figure 84. Cross-sectional view of an array machined with the no-compensation pattern. The spike every third prism represents the seam between scans. The pitch between scans is 180 μm.

between the scans. There is a strong qualitative agreement with the theoretical considerations above; nevertheless the fact that the wedge of the seam is not as tall as the prisms is surprising. The height of the ridge is only about 2/3 of the total height of the structure and furthermore at the top appears to be a kink (see Figure 85).
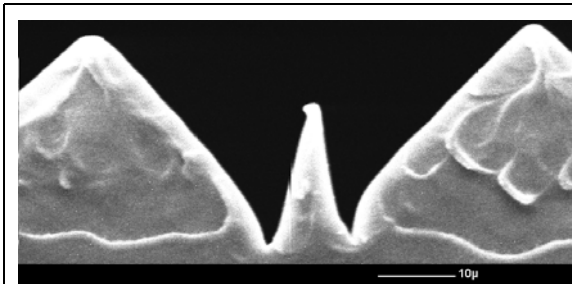

Figure 85. Cross-sectional view of the ridge when the sidewise step distance between scans is equal to the image width.
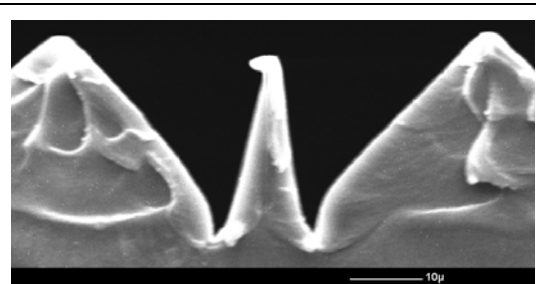
Figure 86. Cross-sectional view of the ridge when the sidewise step distance between scans is 1.5 μm greater than the image width. Note the cranked top pointing in the direction of the air jet.

In order to gain a better understanding of what happens here, the sidewise step between scans is slightly increased. Figure 86 shows the result for a sidewise pitch distance that is 1.5 μm greater than the image width. The ridge height has increased while at the same time its top is clearly kinked. The interpretation of this finding is that because of the thermal element in the ablation process and the heat in the plasma the thin top of the ridge is heated up and then bent to the left as an air jet is applied during the ablation blowing from the right in this instance. In the case where the sidewise step between scans is equal to the image width (Figure 85) the very thin top third of the ridge simply melts away.

5.3.2.3 Prism structure with rectangular compensation

The second set of experiments is carried out with a prism structure with a rectangular extension on one side of the mask pattern; the extension is designed to compensate for a wall angle of 12° and is therefore 6 µm wide at the image plane. Figure 87 shows a cross-sectional view of the result of scanning the mask image once over the Polycarbonate surface. The rectangular extension is in this case on the right hand side of

Figure 87. Cross-sectional view of the rectangular compensation pattern machined in one scan into Polycarbonate. Lower picture compares the centre prism profile with the profiles of the prisms to the left and right. There is strong distortion on the edge without compensation (A) while there is a good match on the compensated side (B) but an excess of material ablation.

Figure 88. Close-up of ablation result of the rectangular compensation mask design. The prism wall is straight and well-defined but running to deep.

the image; on the left hand side the design is the same as the one used in the previous experiment. The lower picture in Figure 87 uses the centre prism as a reference and its profile is copied over the prisms to the right and left respectively (in red). What can be seen is that the prism on the left (A) is strongly distorted due to the wall angle issue. The prism on the right (B) is more or less identical with the centre prism and has not suffered distortion; however, there is an excess of material removal at the base of the prism joining the wall. This points to the issue that the designed angle needs to match the wall angle corresponding to a given fluence, NA and material combination. In this case the resulting wall angle is ~8° instead of the assumed and designed 12°; hence too much material is removed even in one scan. An excess in depth of ~4 µm is measured.

Figure 89 shows an SEM picture of a cross-sectional view of part of a prism array machined with the rectangular compensation mask. The array was machined from left to right with the rectangular compensation on the right hand side. The result shows the expected groove between the scans (every third prism). There is a strong qualitative agreement with the theoretical considerations above. The groove is ~12 μm deep, which is more than 1/3 of the designed structure depth. It can be assumed that by a perfect match between resulting wall angle and the design of the rectangular compensation the resulting groove depth could be reduced by ~4 μm. This would still cut a groove of 8 μm in depth where the scans join.
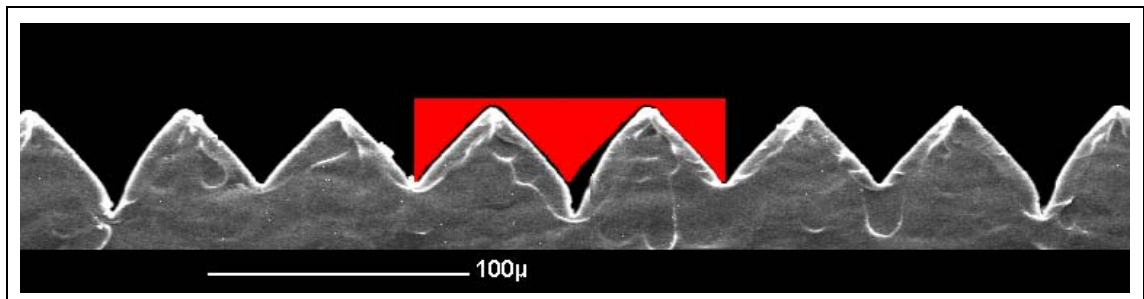

Figure 89. Cross-sectional view of an array machined with the rectangular compensation pattern. The groove after every third prism represents the seam between scans. The pitch between scans is 180 μm. The excess in depth is ~12 μm. The red mask is a copy of the profile of the centre prism in the right hand scan. There is not only a groove but also a strong distortion of the prism face on the left hand side of the groove clearly visible. The array was machined from left to right.

Taking the centre prism profile of an individual scan and using it as a mask on the prisms to the left and right of the scan joint highlights that not only a groove is cut, but that the prism face to the right of the groove is strongly distorted. The distortion is the result of the excess of energy as the laser beam of two scans overlap in this region (Figure 73).

This result proves that with extra-width added onto one side the wedge can be eliminated. The issue is nevertheless that the correction is going too far and that the wedge is replaced with a groove and that the features next to the groove are distorted. This leads to a third approach with a balanced compensation on both edges of the image as introduced above in subsection 5.2.1.

5.3.2.4 *Prism structure with triangular compensation*

Figure 90 shows a cross-sectional view of the result of scanning the mask image representing the balanced slope compensation once over the Polycarbonate surface. An eye-catching effect is that the left hand edge of the scan does not even reach half of the designed depth. This is not surprising as with the slope compensation part of the integrated energy dose is moved from one edge of the tool to the other. Furthermore, this side of the slope compensation is scanned in negative direction resulting in additional misrepresentation of the designed slope. The prism on the right hand side, however, looks well-defined. Figure 91 shows a close-up of the prism and the resulting wall angle where the prism does not seem to suffer any distortion.
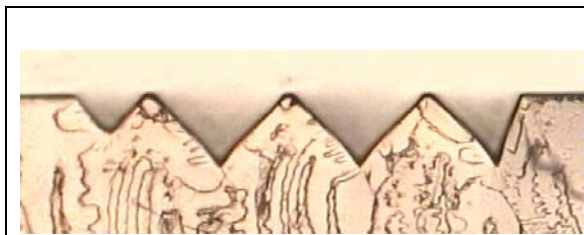

| **Figure 90.** Cross-sectional view of the slope compensation pattern. | **Figure 91.** Close-up of ablation result on the edge of the slope compensation pattern. |
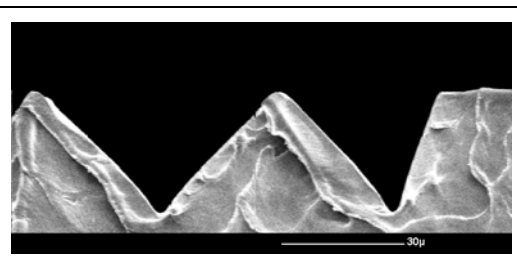
The result of one scan is in good agreement with the theoretical assumptions made above. It is now interesting to see if arraying individual scans will result in a continuous profile where each prism matches the design. Figure 92 shows an SEM picture of an array cut with the slope compensation mask; it is clearly visible that there is neither a wedge nor a significant groove where the scans join.

Figure 92. Cross-sectional view of an array machined with the slope compensation pattern.

Nevertheless there is a small discontinuity at the base of every third prism. Figure 93 is a zoom-in picture of the critical region. It can be seen tha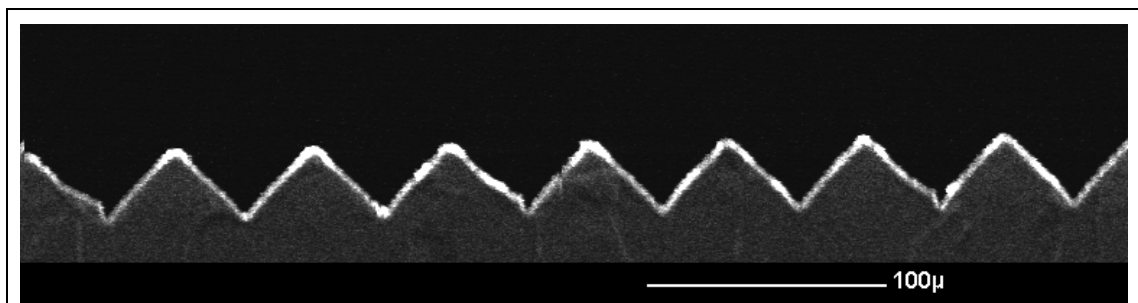t there is a small nudge on the start of the second prism; furthermore, the second prism face is bowed inwards a little. As the error is rather small, it is not easy to explain what has caused it. The reason could be energy reflection off the relatively steep slope at the beginning of the scan but also slight misalignment from one scan to the other could be a reason.
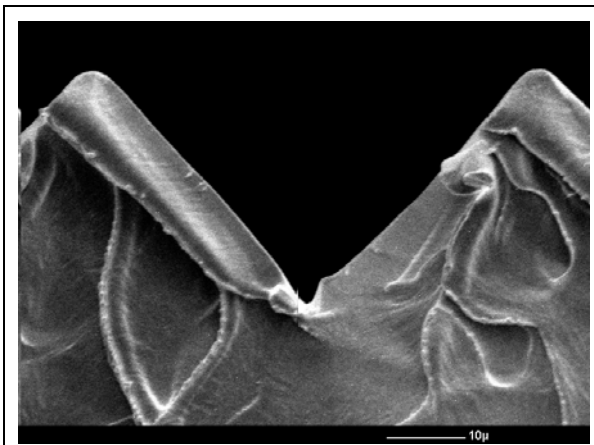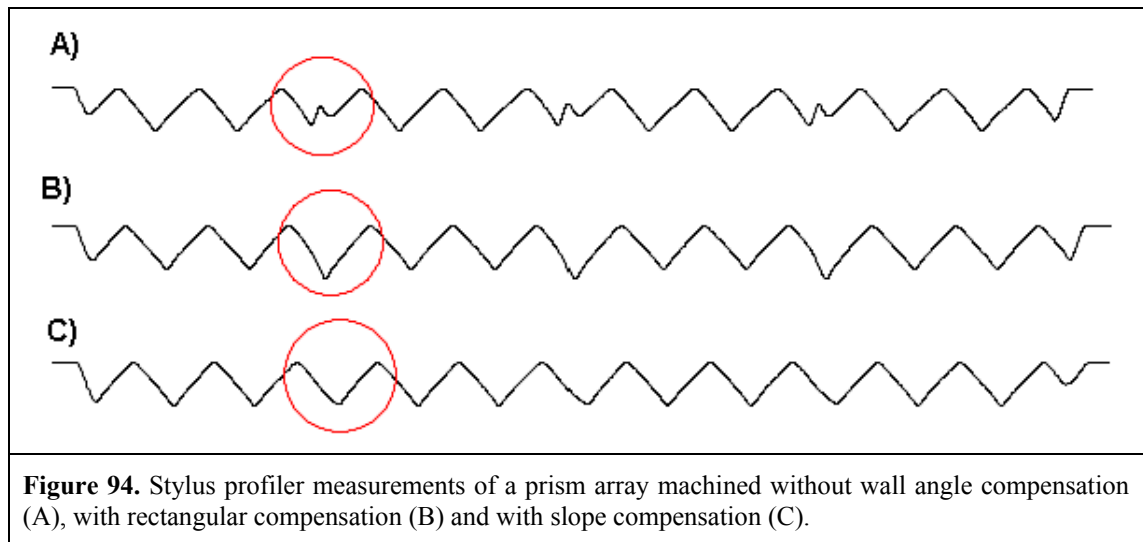

Figure 93. Detail of the joint of two scans with sloped compensation. Only a small error in profile can be seen where the two scans join.

Further experiments would be necessary to fully understand what causes the small discontinuity of the profile in the region where two scans join. Nevertheless it can be said that the suggested and tested slope compensation gives by far the best result of the three investigated approaches to machine a continuous profile. Figure 94 shows the output of stylus profiler measurements of all three cases. While no seam compensation leaves a ridge and a distorted feature running along the scan direction stepping every image width (A), the rectangular compensation leaves a groove instead and still distorts the feature next to it (B). With profile (C) is confirmed that the slope compensation achieves the best result.

Please note that the limits of measuring such structures with a stylus profiler are clearly manifest here. The sharpness of the ridge between scans (A) cannot be represented and the stylus force does actually damage the top of the ridge. Equally the walls at the edges are too steep to be measured with the 40° stylus tip.

Figure 94. Stylus profiler measurements of a prism array machined without wall angle compensation (A), with rectangular compensation (B) and with slope compensation (C).

5.4 Conclusions

It can be concluded that with the right measures it is possible to eliminate unwanted artefacts which can appear when creating positive/convex features. Applying Beer's law as a basic ablation model is enough to predict reasonably closely what will happen if the geometry of the image is modified in certain ways. Three different image patterns have been designed and the results predicted. It has been found that experimental data are generally in good agreement with the predicted results. Nevertheless, at the micron and submicron level the resulting structure still deviates from the design although the result matches the target within a few percent. Further investigations into wall angle reflection, thermal effects and the influence of the high velocity air jet used during the ablation process would help to further improve the process and to be able to tighten the tolerance on the geometrical structure and to make reliable predictions about the result.

1. E. Harvey, P. Rumsby, M. Gower, J. Remnant, SPIE Vol. 2639 (1995)

2. C. Paterson, A.S, Holmes, R.W. Smith, Appl. Phys. 86, 11 (1999)

3. K. Jain, M. Klosner, M. Zemel, S. Raghunandan, IEEE 93, 8 (2005)

4. K.L. Boehlen, I.B. Stassen Boehlen, R. Allott, SPIE Vol. 5720 (2005)

5. J.E.A. Pedder, A.S. Holmes, SPIE Vol. 6106 (2006)

6 Surface finish enhancement

6.1 Introduction

In chapter 4 it was discovered that subsequent UV laser exposure of a rough machined surface enhances the surface quality. In this chapter the focus is on further investigations into this matter. A series of test experiments is carried out to establish if a post-process employing UV laser ablation can in fact enhance the surface quality of laser-etched micro-structures. Laser polishing is otherwise rather done at an IR wavelength [1,2,3]. Nevertheless there are some results reported on laser smoothing of Polycarbonate [4,5].

6.2 Experiments to enhance surface quality

6.2.1 Design of experiment

The basis for the experiment presented here is the MLA introduced in chapter 4. The same mask and the same conditions are used to laser cut an MLA of ~50 mm x 30 mm. The scan direction is positive and the fluence set at around 480 mJcm^{-2}; this slightly higher value is chosen to cut the lenses deeper to compensate for polishing ablation. The sample is cleaned before a fluence-shot matrix with a scanning image is applied.

The fluence range is from 100 mJcm^{-2} to 200 mJcm^{-2} with 20 mJcm^{-2} increments while the shot range is from 20 to 100 shots with increments of 20 shots at 30 Hz resulting in a total of 30 test sites. The scan length is about 30 mm with a 0.25 mm gap between each scan. The object pattern is a rectangular aperture (12 x 0.5 mm^2). The desired number of shots per area is achieved by choosing the corresponding firing pitch in each instance.

After the polishing ablation is done the sample is cleaned again. Each position is then measured with the stylus profiler and the WLI. The sample is thereafter gold-coated and inspected in an SEM.

6.2.2 Results of the experiment at 248 nm wavelength

As found in chapter 4 the stylus profiler delivers a useful set of data; hence it is also chosen here to determine the surface roughness values. Each ablation site in the fluence versus number-of-shots matrix produced is measured with the stylus profiler to find the *Ra, Rq* and *Rt* values. The values represent an average of a line scan across ~85% of the centre part of a lens; Table 15 shows the values of one lens per ablation site. Even

Ra/Rq/Rt [nm]	# Shots	20	40	60	80	100
Fluence [mJcm^{-2}]						
100		39/51/249	25/31/97	24/31/85	27/37/104	23/31/82
120		35/38/203	22/27/124	26/33/81	21/27/93	21/25/51
140		32/44/90	32/30/108	16/22/91	23/27/57	22/26/57
160		27/35/126	21/29/133	20/25/72	15/18/57	11/17/59
180		25/33/117	26/34/137	18/23/96	16/21/47	15/21/56
200		22/30/61	21/26/63	19/18/59	12/15/65	9/12/54

Table 15. Fluence vs shot matrix of polishing scans applied to an MLA with the resulting *Ra*, *Rq* and *Rt* values. Raw lens values are *Ra* 42 nm, *Rq* 55 nm, *Rt* 293 nm with an average deviation of 207 nm.

though only one lens per ablation site is evaluated, these values can be regarded as representative for the specific fluence and number of shots. This has been confirmed by additional measurements without deriving a statistical value.
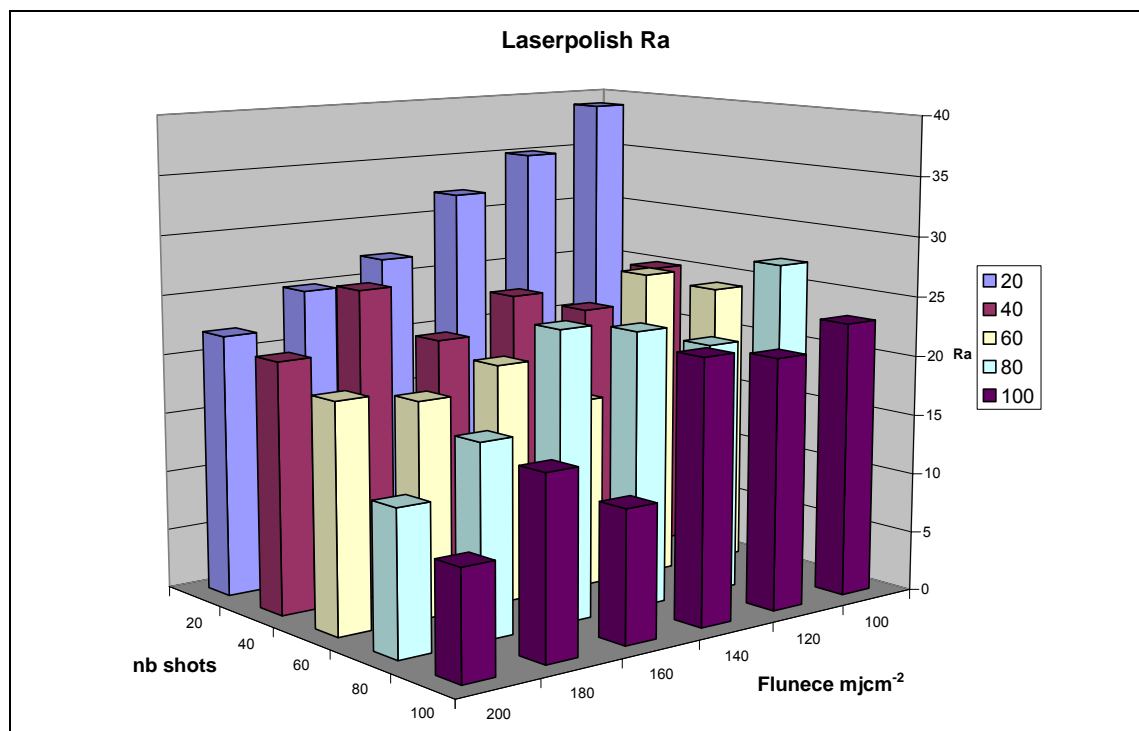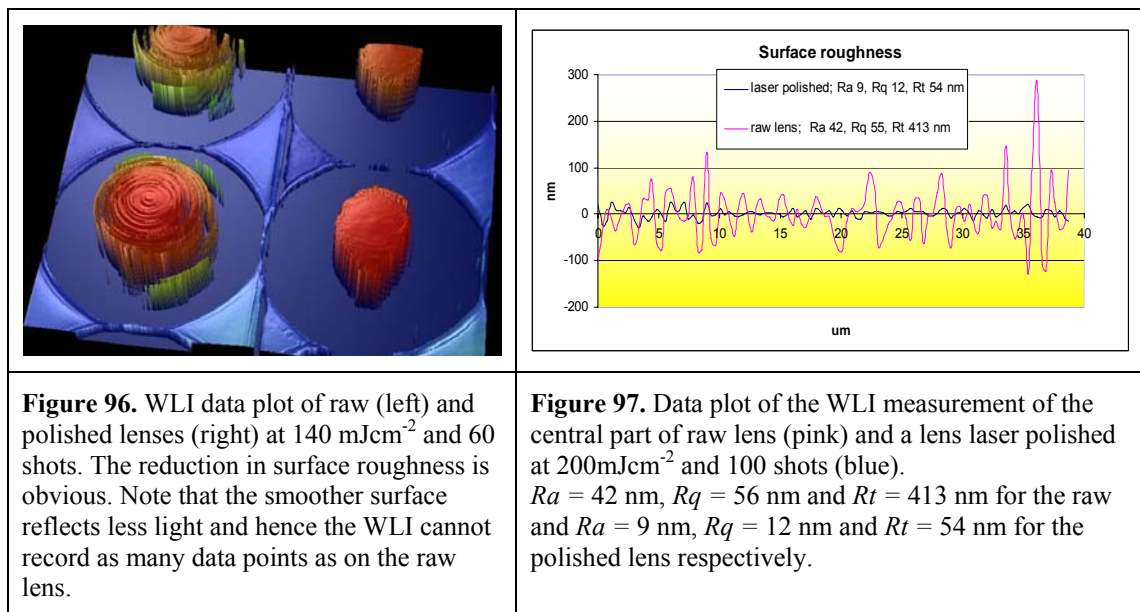

Figure 95. Plot of the *Ra* data from Table 1.

Figure 95 shows a plot of the data of Table 15. It reveals that both an increase in the number of pulses as well as an increase in fluence reduce the surface roughness values. It seems that 20 pulses are not sufficient; only when applying 40 or more pulses the surface roughness is significantly reduced. Although the values are single measurements and the measurement error can be more than 10%, it can be concluded that already a few tens of pulses at a fluence above 100 mJcm^{-2} will have a polishing effect. Especially the peak-to-valley difference is significantly reduced.

Figure 96. WLI data plot of raw (left) and polished lenses (right) at 140 mJcm^{-2} and 60 shots. The reduction in surface roughness is obvious. Note that the smoother surface reflects less light and hence the WLI cannot record as many data points as on the raw lens.	**Figure 97.** Data plot of the WLI measurement of the central part of raw lens (pink) and a lens laser polished at 200mJcm^{-2} and 100 shots (blue). $Ra = 42$ nm, $Rq = 56$ nm and $Rt = 413$ nm for the raw and $Ra = 9$ nm, $Rq = 12$ nm and $Rt = 54$ nm for the polished lens respectively.

After these experiments it can be said that post-processing with a moderate fluence and several tens of pulses can eliminate the high frequency variations on the surface. Figure 96 shows a WLI 3D data plot of a raw (not post-processed) lens on the left and polished lenses on the right; the polishing parameters are 140 mJcm^{-2} fluence and 60 shots. The reduction in surface roughness is obvious. Note that the smoother surface reflects less light and hence the WLI cannot record as many data points as on the raw lens. Figure 97 shows a data plot of a WLI measurement of the central part of a raw and a laser polished lens at 200 mJcm^{-2} and 100 shots.

The improvements of the surface quality are significant with $Ra = 42$ nm, $Rq = 56$ nm and $Rt = 413$ nm for the raw and $Ra = 9$ nm, $Rq = 12$ nm and $Rt = 54$ nm for the

polished lens respectively. This shows that the *Ra* and *Rq* values can be reduced to less than a quarter and *Rt* to 1/8.
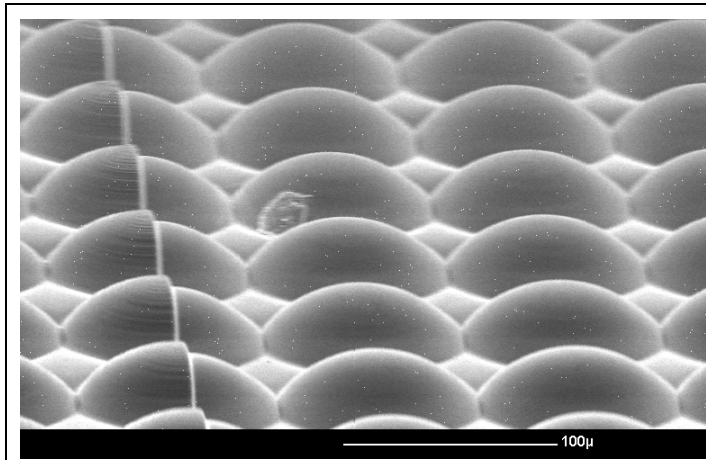

Figure 98. SEM picture of the scan edge of a laser polishing scan at 200mJcm^{-2} and 60 shots. On the left there is a column with half raw and half polished lenses.

The findings are qualitatively confirmed by inspecting the sample in an SEM. Figure 98 shows an SEM picture from the edge of a laser polishing scan at 200 mJcm^{-2} and 60 shots. On the left there is a column with half raw and half polished lenses. Note that the ring structure clearly visible on the raw lens is not detectable any more on the polished lenses; they look nice and smooth. There is no obvious distortion of the lens shape but
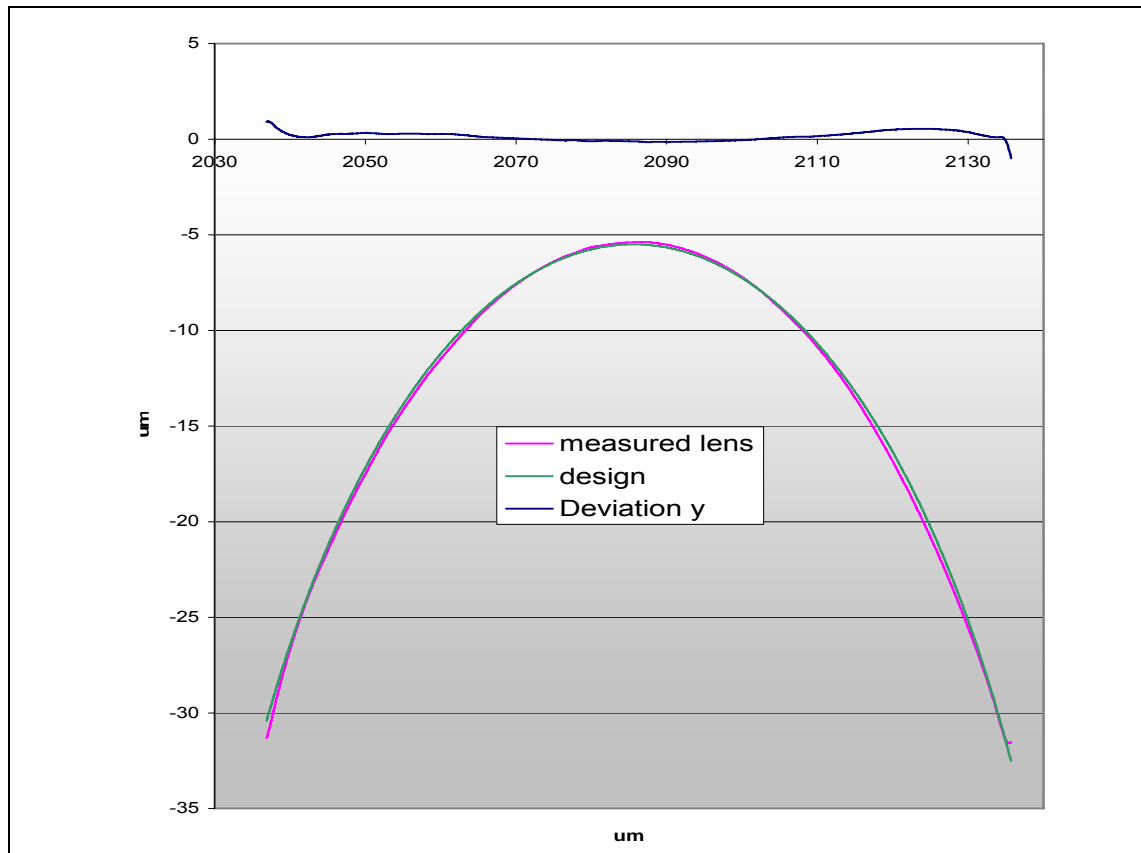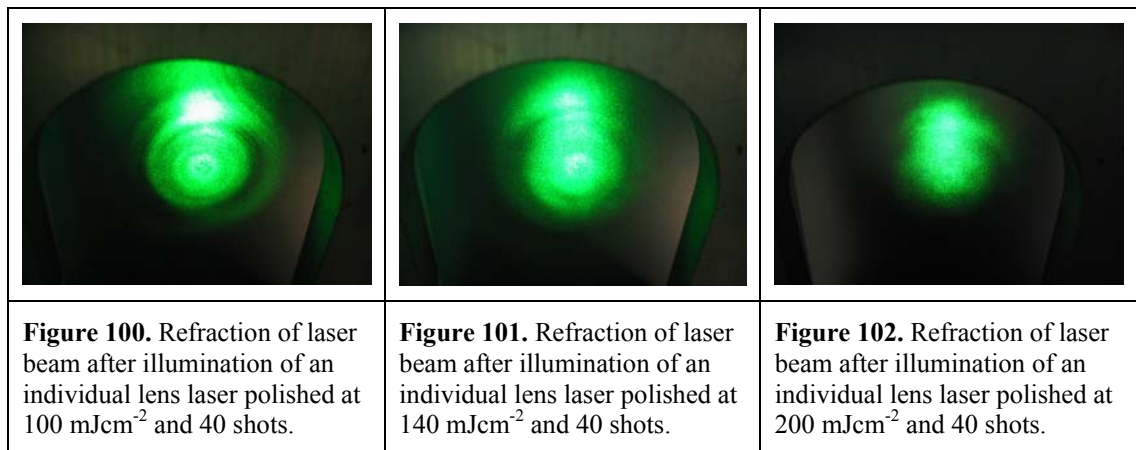

Figure 99. Stylus profiler data plot of a laser polished lens processed at 160mJcm^{-2} and 80 shots. The average deviation from the best fit ROC is 147 nm with a ROC of 59.2 μm while the target is 60 μm.

as seen before it is not possible to make a judgement on this matter by just looking at an SEM picture. What can be seen is that the lens structure has been significantly embedded by the laser polishing process. This is not surprising as at 200 mJcm^{-2} theoretically more than 130 nm is ablated per shot.

For the optical behaviour of the lens it is of course paramount that the lens shape is not distorted during laser polishing. It is known that uniform irradiation of a non-planar geometry will distort the original geometry [6]. As the tests here are mainly focussed on the surface polishing, no detailed investigations are made into how to compensate for possible distortion introduced by the polishing ablation. Nevertheless in a first attempt the raw lenses have been machined 2 μm deeper than the design. This means that the lenses are slightly elongated before the laser polishing. The laser polishing process has then a correcting effect on this as can be seen in a well matching result after polishing in Figure 99 where a data plot of a stylus measurement of a lens polished at 160mJcm^{-2} and 80 shots is shown. The *Ra* = 11 nm, *Rq* = 13 nm, *Rt* = 56 nm values already known from Table 1 are joined by a remarkably low average deviation from the best mean square ROC fit of 147 nm. The resulting ROC with 59.2 μm is only 1.4% off target. Note that the polishing step has embedded the whole lens around 6 μm into the Polycarbonate. The measurements made so far confirm that laser polishing as applied here can significantly enhance the overall lens quality.

In order to know if the lens is also behaving optically better after polishing the same refraction test of a single lens as in chapter 4 is performed. Figure 100-Figure 102 show lenses polished with 40 shots at an increasing fluence of 100, 140 and 200 mJcm^{-2}, respectively, expanding a 532 nm laser beam on a diffuser screen. It is clearly visible that an increase in fluence results in a more homogenous illumination of the diffuser screen; hence it can be concluded that the ring grating on the lens surface is reduced.

However, the illumination on the screen is not quantified here and a more sophisticated setup with calibrated image analysis would be needed to do so. Nevertheless, as this analysis is used in combination with other measurement methods that reveal in particular remarkably low *Rt* values, it can be said that the surface quality can be much improved by applying laser polishing as described here.

Figure 100. Refraction of laser beam after illumination of an individual lens laser polished at 100 mJcm^{-2} and 40 shots.	**Figure 101.** Refraction of laser beam after illumination of an individual lens laser polished at 140 mJcm^{-2} and 40 shots.	**Figure 102.** Refraction of laser beam after illumination of an individual lens laser polished at 200 mJcm^{-2} and 40 shots.

6.3 Summary and Conclusions

A fluence versus number-of-shots matrix has been superimposed on a laser-etched MLA. It can be concluded that uniform irradiation at 248 nm wavelength and relatively low fluence (< 200 mJcm^{-2}) and a modest number of pulses (< 100) have a polishing effect on micro-structures laser-etched at the same wavelength. Given the non-planar nature of micro-structures a non-uniform ablation occurs where convex structures are flattened and concave ones are stretched. As only a few tens of pulses are needed to achieve a polishing effect, the distortion of the original geometry is not that significant. Nonetheless this effect can be compensated for when the structures are laser etched by simply overcutting convex and undercutting concave structures.

More work would be needed to establish a model to predict the exact amount of over- or undercut needed to achieve the desired geometry within a tight tolerance after laser polishing. Nevertheless the results presented show that this should be relatively easy to establish.

For future work it could be interesting to test much longer wavelengths to introduce some thermal reflow at the lens surface without the disadvantages of embedding ablation.

---

1. K. M. Nowak, H. J. Baker, and D. R. Hall, Appl. Opt. 45, 165 (2006)

2. Y. M. Xiao, M. Bass, Appl. Opt. 22, 2933 (1983)

3. R. M. Wood, Laser damage in optical materials, Adam Hilger Bristol, p. 80, 1986

4. K.Naessens, H.Ottevaere, R. Baets, P.Van Daele, H. Thienpont, Appl. Opt. 42, 6349 (2003)

5. T. Gumpenberger, J. Heitz, D. Bauerle and T.C. Rosenmayer, Europhys. Lett. 70 (2005)

6. P.E. Dyer, D.M. Karnakis, P.H. Key, P. Monk, Appl. Surf. Sci. 96, 415 (1995)

7 Micro-lens arrays in various polymers

7.1 Introduction

In this chapter we investigate if SIS can be applied to polymers other than
Polycarbonate (PC). The polymers chosen are PolyImide (PI), PolyEthylene
Terephthalate (PET), Sol-Gel Ormocop [1], SU8 photoresist, Triazene, Clariant
AZ9620 and Parylene. There are several reasons why each of these materials has been
selected (see Table 16). The main goal of this chapter is not so much to get the best
possible lenses, but rather to apply the findings for PC to other materials and to be able
to find a more general case to model the ablation process of 3D features. By testing a
selection of materials and analysing the results it should be possible to derive a model
for SIS that enables us to predict results in materials not yet tested.

Material	Reason for testing
Polyimide (PI)	Tough polymer, arguably the most studied polymer for Excimer laser ablation [2,3].
Polyethylene terephthalate (PET)	Widely used optical grade polymer film e.g. for flexible displays [4]. The trade name of the PET used here is Melinex.
Sol-Gel	Ormocomp is a UV sensitive hybrid material, which was developed for the production of optical micro-structures (UV molding). It is an inorganic–organic hybrid polymer material synthesised by the sol–gel process [5,6].
SU-8	SU-8 photoresist (SU-8-100) supplied by Micro-Chem. Corporation, USA, a thick film photo resist well-known for the LIGA technique and direct laser ablation. [7,8]
Clariant AZ9620	Thick film photoresist used for reflow micro-lens fabrication (Suess).
Triazene	Especially designed for laser ablation at 308 nm [9]. Designed and synthesised at Paul Scherrer Institut, 5232 Villigen, Switzerland.
Parylene	Very high coating quality, very low surface roughness previous to laser ablation. Can be used as optical material. [10]

Table 16. Materials used to test the same mask as used for PC and the reasons why they have been chosen.

The plan is to machine micro-lens arrays into all the materials mentioned above to produce lenses that have a target ROC of 60 μm and an aperture of 100 μm diameter. If the considerations made so far add up, it should be possible to use the same mask as used before for the micro-lens array into PC. All that should be necessary is to find the fluence that corresponds to the ablation rate per pulse equal to the slice thickness used for the mask design.

7.2 Experiments with micro-lens arrays

7.2.1 Design of experiment

The layout for the experiments here is very similar to the one in chapter 4. The first step is to obtain the ablation curve for each material. It is possible to find parameters in the literature, but it can be difficult to find the ones that are applicable and in some cases there are just not the right values to be found. Hence to get an ablation curve of each material a scan through a fluence range from 150-1000 mJcm^{-2} with an increment of 50 mJcm^{-2} and 50 shots is carried out. The ablated depth for each fluence is measured with a stylus surface profiler. A least linear square fit of the Beer's law function through the data points:

$$d = \frac{1}{\alpha} \cdot \ln\left(\frac{F}{F_t}\right)$$

Equation 22.

is used to derive values for the effective absorption coefficient α and the threshold fluence F_t.
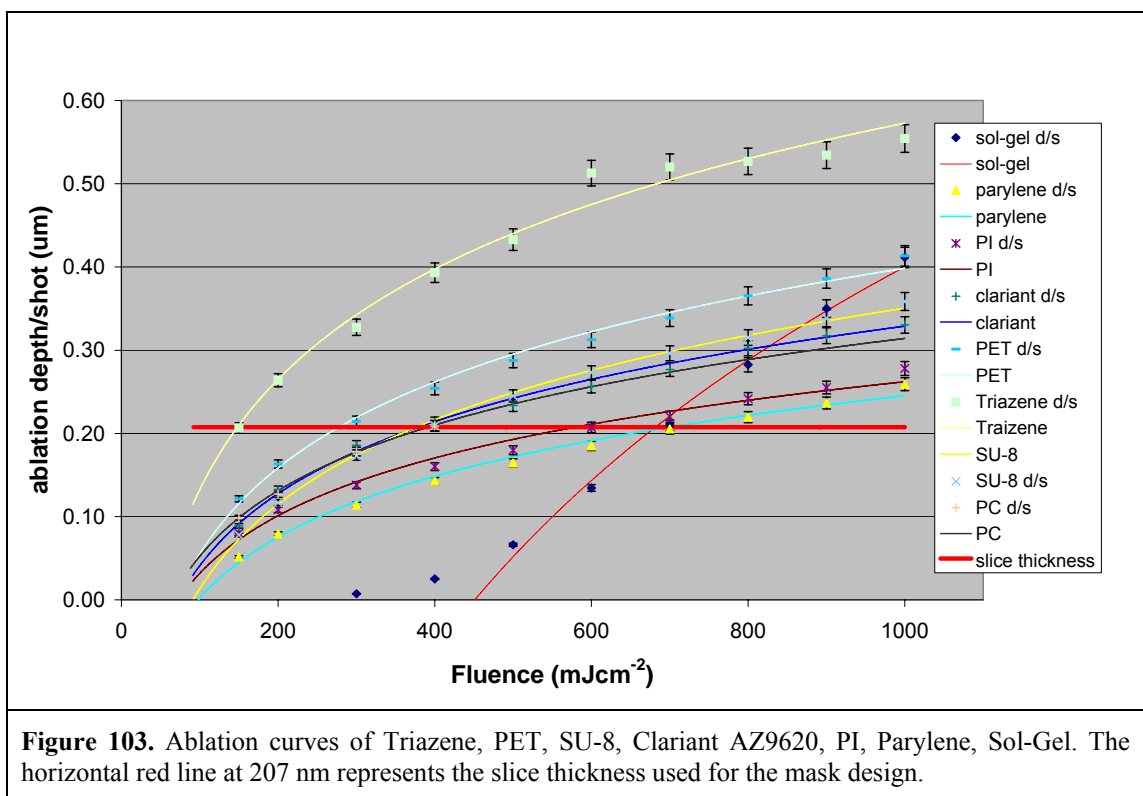
As the mask is given, the number of apertures is fixed and thus the ablation depth per shot, too. The value for d determined in chapter 4 is 207 nm. All that is necessary now is to determine the corresponding fluence for each material. To get a higher chance of machining the right shape a fluence range around the value found is machined where possible. Unfortunately there is not always enough test material available to do this, but

the objective of these experiments is not to achieve the very best lens for each material
but rather to get an idea if the tested material is generally suitable for SIS.

The results are analysed using optical and/or electron microscopy as well as a stylus
profiler. The lens in this case is chosen as a geometrical feature and the interest is
mainly on the resulting shape and surface roughness. No optical tests are planned as
some of the materials used are not optical grade.

7.2.2 Presentation of the results

7.2.2.1 *Ablation parameters of materials tested*

Figure 103. Ablation curves of Triazene, PET, SU-8, Clariant AZ9620, PI, Parylene, Sol-Gel. The horizontal red line at 207 nm represents the slice thickness used for the mask design.

A fluence scan as planned is performed for each of the selected materials. Figure 103
shows the ablation curves for all seven materials and includes PC as reference;
furthermore, a horizontal red line at 207 nm represents the slice thickness value used for
the PC mask design. All curves look similar except for the one for Sol-Gel; this is not
that surprising as Sol-Gel is strictly speaking inorganic rather than organic.

Material	α [μm^{-1}]	F_t [mJcm^{-2}]
Tirazene	5.23	50
PET	6.71	69
SU-8	6.83	91.1
AZ9620	8	72
PI	10	72.7
Parylene	9.47	98
Sol-Gel	1.99	451

Table 17. The effective absorption coefficient α and threshold fluence F_t are listed for all the materials tested.

Table 17 lists the effective absorption coefficient α and threshold fluence F_t for all the materials tested. With these data it is in principle possible to design an optimised SIS mask for each material and to freely choose the most suitable process fluence. However, this would be a laborious and costly thing to do for these studies; hence the approach here is as mentioned above to use the existing mask originally designed for PC and to find the

Polymer	Calculated process fluence [mJcm^{-2}]
Triazene	148
PET	278
SU-8	376
Clariant	379
PC	392
PI	580
Parylene	701
Sol-Gel	682

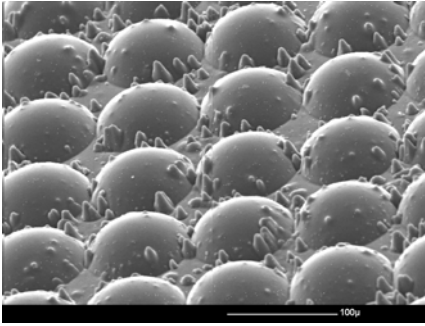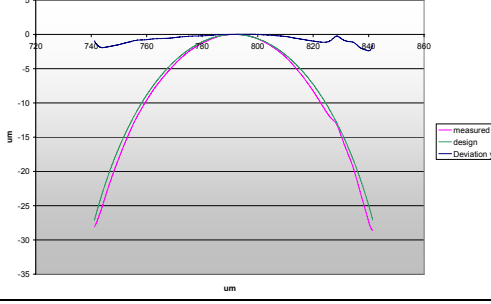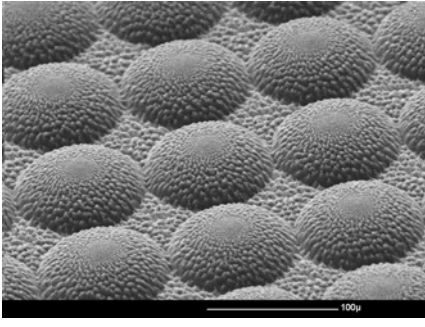**Table 18.** Test polymers and calculated process fluence to match slice thickness of existing mask of 207 nm.
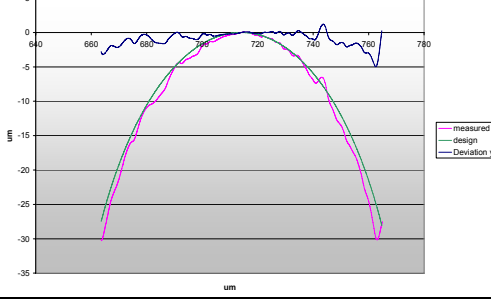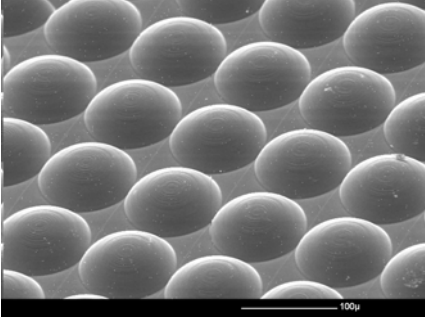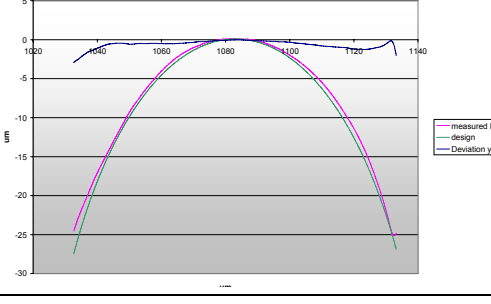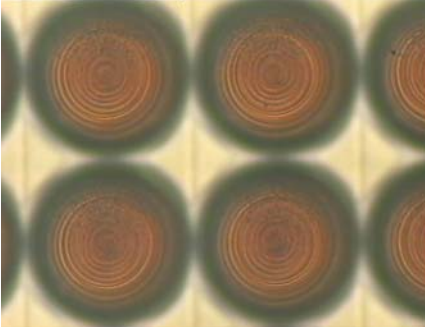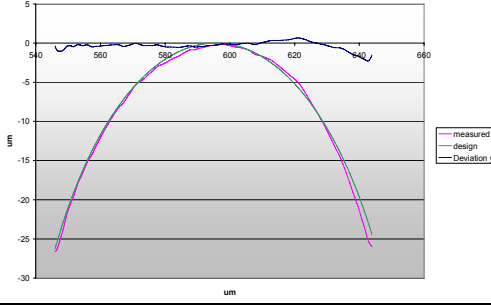
process fluence for each material that will result in an ablation rate of 207 nm per pulse.

Table 18 lists the test polymers and the corresponding process fluences that match the required ablation depth per pulse. A significant range in process fluence is observable with values between 148 and 701 mJcm^{-2}. If it is indeed possible to cut the same lens profile into various polymers using the same mask, this would of course be a big benefit as mask costs are high, but more importantly it would confirm the findings so far and that the model on which the SIS process is based it reliable.

7.2.2.2 *Geometrical and surface quality results of materials tested*

As mentioned above lenses are machined in all seven materials and in both scan directions. Optical or electron microscope pictures and measured profiles of the positive scan are shown in Table 19. Under each profile plot the *Ra*, *Rq* and Average Deviation (AD) values are given. Looking at this table it can be observed that a positive scan of

the mask image at the required fluence etches indeed a lens profile matching the target reasonably closely. As found in chapter 4, machining in the negative scan direction does not achieve a satisfactory result in respect of the expected profile. Hence the results are not shown in the table below. Each material and the resulting lens shape are discussed in more details after the summary in Table 19.

Material	Picture	Stylus profile
Triazene		 Rq = 19 nm, Ra = 15 nm, AD = 543 nm
PET		 Rq = 286 nm, Ra = 241 nm, AD = 632 nm
SU-8		 Rq = 47 nm, Ra = 38 nm, AD = 630 nm
AZ9620		 Rq = 61 nm, Ra = 52 nm, AD = 402 nm
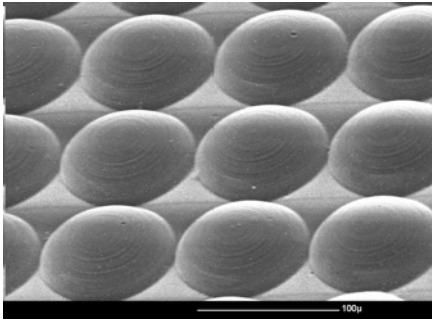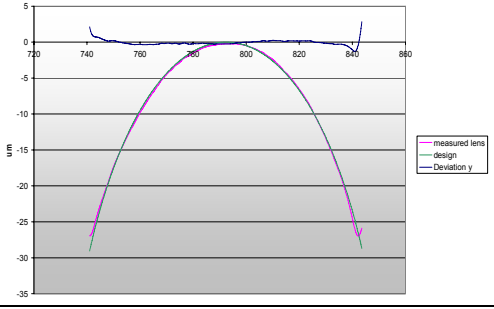
PI		
		Rq = 48 nm, *Ra* = 39 nm , AD = 271 nm
Parylene		
		Rq = 117 nm, *Ra* = 90 nm, AD = 245 nm
Sol-Gel		
		Rq = 31 nm, *Ra* = 26 nm, AD = 630 nm
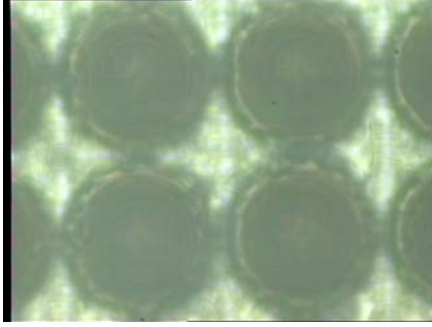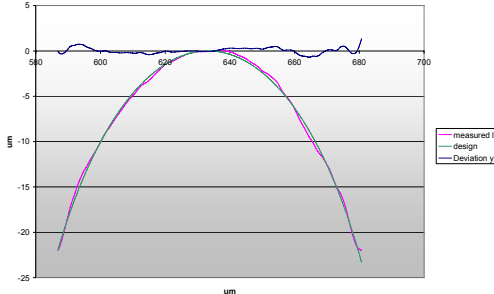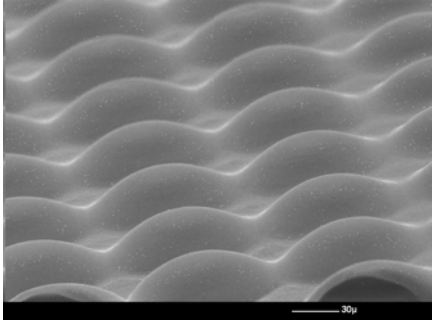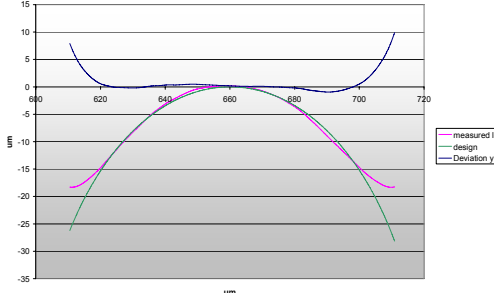
Table 19. Micro-lens arrays laser etched into seven different materials are presented by means of a microscope picture and a profiler measurement. Additionally the *Rq*, *Ra* and Average Deviation from the target sphere are listed.

A. Triazene

The most obvious feature is the large number of cones that are produced all over the area where the lenses are cut. The cones are growing because of particles with higher ablation threshold in or on top of the material [11,12]. The test material available contains a lot of particles as can be seen from the number of cones. It is rather unlikely that these cones have been caused by re-deposited ablation debris on the surface as hardly any debris can be observed after processing. Nevertheless the fact that the Triazene polymer used here is designed for ablation at λ = 308 nm [13] but was

machined at $\lambda = 248$ nm seems to favour the cone appearance as a direct comparison with the SEM picture in Figure 104 suggests.

Ignoring the cones the lenses etched look good with by far the best surface quality of all with $Ra = 15$ nm and $Rq = 19$ nm . The profile match is not very good as the applied fluence is slightly too low and hence the lenses are not etched deep enough. The results are very promising and with particle-free material processed at $\lambda = 308$ nm very high quality micro-features etched with high efficiency can be expected. This is partly confirmed by Figure 104 where a hexagonally packed micro-lens array is shown with lenses of an ROC of 25 μm and a maximum aperture of 50 μm etched with the 308 nm XeCl laser. The
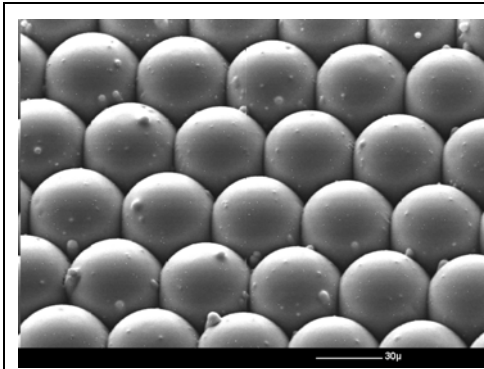
Figure 104. Hexagonally packed micro-lens array in Triazene etched at $\lambda = 308$ nm with ROC of 25 μm and maximum aperture 50 μm.

number of cones is reduced and the surface looks very smooth. The smaller lenses are chosen for this test as the spot size created by the 308 nm beam delivery optics is not large enough to illuminate the mask pattern for the 100 μm aperture lenses.

B. Polyethylene Terephthalat (PET)

It is well-known that the PET surface develops a granular appearance which seems to result from a relaxation of stress in the temperature rise during the ablation process [14,15], hence the surface roughness of the ablated lenses in PET is very high. This micro-structure on the surface after ablation is found in bi-axially oriented PET and can be eliminated using amorphous (not aligned) material. However, the optical properties tend to be compromised through the cloudiness of amorphous PET. Although the lens surface is rough the lens profile is still machined. This result could be regarded as a lens shape with an integrated diffuser, but it is questionable if this could be useful as an

optical component. Nevertheless it can be said that with SIS it is possible to create the desired geometry while the surface texturing is caused by stress release in the material.

C. SU-8

A good quality micro-lens array is produced. The surface roughness and process fluence are close to those of PC. The reason for a high average deviation is again a slightly too low fluence resulting in a not fully etched lens.
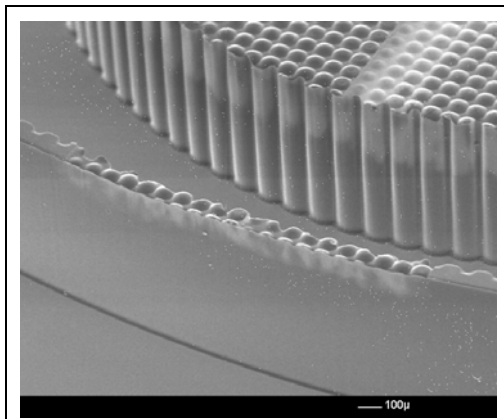
Figure 105. Micro-lens array machined onto a lithographically produced high aspect ratio structure of SU-8.

SU-8 as a thick film resist is interesting for various MEMS applications where the LIGA process can be applied [16,17]. Figure 105 shows the potential of a combination of thick film lithography and SIS: a lithographically produced high aspect ratio structure with a laser etched micro-lens array on top. Note that the lenses have been machined onto a ~1 mm high and 100 μm thick wall without any damage to the existing structure; the discolouration close to the rim is caused by debris deposition that could be washed off.

D. Clariant AZ9620

Again the ablation curve of AZ9620 is similar to the one of PC; hence the etching results are pretty similar too. The ring grating seems more pronounced. Note that the resist has been applied onto a 6" quartz wafer; due to the size of the wafer it is not possible to take SEM pictures.

E. Polyimide (PI)

Although the process fluence applied is significantly higher than for PC, the result looks

good and matches the one in PC. However, the debris is of a different kind and has to be taken care of; otherwise it will cause cones to appear.

As mentioned before PI is a very well investigated polymer in respect to laser ablation; hence it is positive to know that SIS can be applied to this widely used material although more likely for IR or non-optical applications.

F. Parylene

Even though the etched profile is close to the target, the surface roughness is rather high and similar to PET. Additionally debris deposition which is hard to clean off jeopardises strongly the overall quality of the structure. An untypical behaviour can be observed for the negative scan of Parylene (Figure 106 and Figure 107): while for all other materials tested a negative scan results in a strongly distorted lens, here it is surprisingly close to the target with much improved surface roughness compared with the positive scan. The smoother surface suggests that laser polishing could significantly enhance the surface quality when processing Parylene.

Figure 106. Parylene processed in a negative scan resulting in a relatively smooth lens surface.

Figure 107. $Rq = 40$ nm, $Ra = 30$ nm, AD = 390 nm.
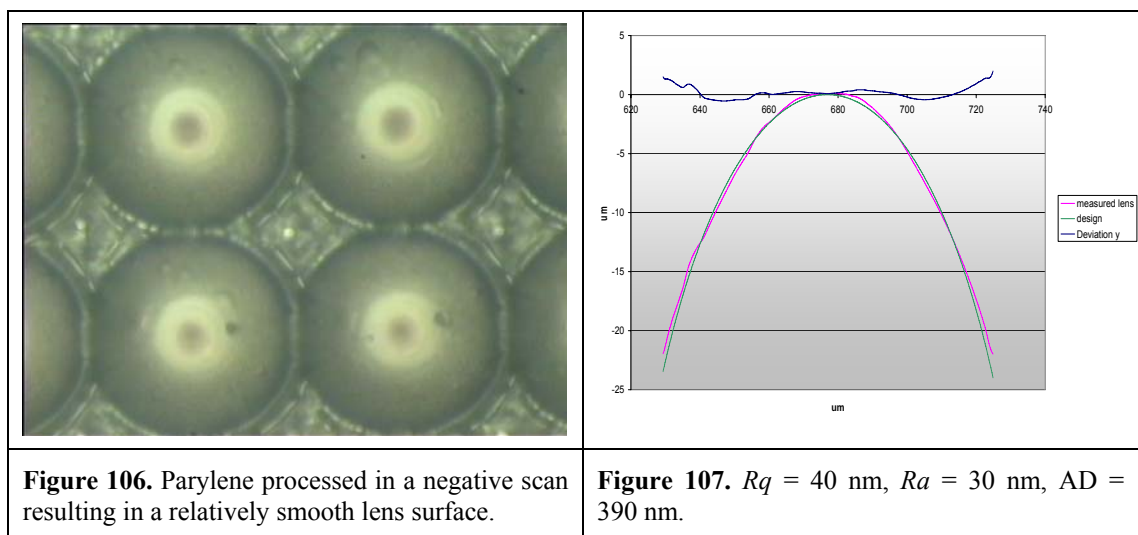
G. Ormocomp Sol-Gel

The ablation curve for Sol-Gel in Figure 103 differs significantly from all the other materials tested. The form $d = 1/\alpha \; ln \; (F/F_t)$ with $\alpha = 1.99 \; \mu m^{-1}$ and $F_t = 451 \; mJcm^{-2}$

gives a reasonable fit to the data in the higher fluence regime, but seriously overestimates the threshold fluence. As can be seen from Figure 103, etching persists at a fluence of ~300 mJcm^{-2}, which is well below this value of F_t. This implies that the simple Beer's law model is not particularly good for this case.

The reason for the poor results found when etching the lenses at ~700 mJcm^{-2} could be that this fluence is too low to produce consistent results. Although the surface roughness is good and 2/3 of the lens is reasonably well etched, the target profile is clearly not achieved and further etching could not correct for this. It could be argued that good results can be achieved at significantly higher fluences, but this would require a modified mask design as the ablation per pulse (slice thickness) increases accordingly.
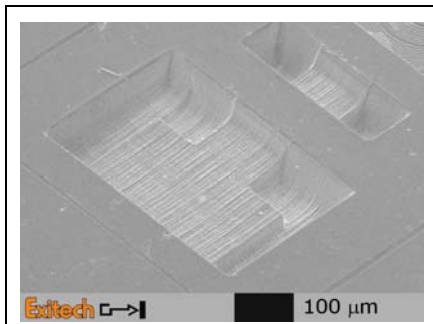
Figure 108. Structure machined at 266 nm wavelength into Sol-Gel; process fluence > 18 Jcm^{-2}.

Figure 108 gives evidence that reasonable results can be achieved by UV ablation of Sol-Gel. Here a focused quadrupled solid state laser beam ($\lambda = 266$ nm) guided by a galvo-scanner has been employed to etch this 3D pocket. Note that the fluence applied to ablate this pocket is ~25 times higher than the one used in the experiment with the KrF laser.

To make a judgement it can be said that 4 out of 7 polymers tested (Triazene, SU-8, Clariant AZ9620, and PI) achieve reasonable profiles and surface quality while the other 3 (PET, Parylene, Sol-Gel) either fail in profile or surface quality. Nevertheless even the failing ones show that SIS works in principle and that with specific adaptations there is scope to use SIS to structure those materials, too.

Triazene	✓
PET	✗
SU-8	✓
AZ9620	✓
PI	✓
Parylene	✗
Sol-Gel	✗

Table 20. Materials which show similar results in the SIS process like Polycarbonate (✓) and materials which show some issues when processed by SIS (✗).

On all materials the mask array is also scanned in negative scan direction and the findings discovered for PC and discussed in chapter 4 are confirmed. Plotting the data of the designed and the actual lens profile and the deviation of the two shows the typical "bull head" with an overcut of the middle part of the lens and the undercut at the top and foot of the lens. This is true for all materials but Parylene. Figure 109-Figure 111 show the plots of the negative scan results of SU-8, PI and AZ9620.

Figure 109. Negative scan into SU-8: Top of the lens closely matched design but sag height not reached; further ablation would distort the lens. Surface roughness similar as by positive scan with *Ra*: 33 nm, *Rq*: 41 nm.

Figure 110. Negative scan into PI: Too much material is removed in the middle part of the lens, but full sag height is not reached. Surface smooth with *Ra*: 25 nm, *Rq*: 32 nm.

Figure 111. Negative scan into AZ9620: Too much material is removed in the middle part of the lens; hence the resulting shape approaches a cone. Surface roughness half of the positive scan with *Ra*: 27 nm, *Rq*: 32 nm.

Beside the profile distortion a better surface quality as a typical result can be observed compared to the positive scan. The data plots in Figure 109-Figure 111 confirm the findings for PC: increasing the fluence to reach the sag height does not help to etch the desired lens. What can be seen when looking at the plots from left to right is that the deeper the structure is cut the more the resulting profile deviates from a spherical lens and approaches a more conical shape. Although only three different materials are shown, it is reasonable to draw the conclusion that this is a clear characteristic when scanning the aperture array in negative direction.

7.2.2.3   *Discrepancy between theory and result*

Although the target profile is matched quite closely for several of the materials, for all but Parylene a higher fluence than predicted is actually needed to achieve the target profile. In Table 21 and Figure 112 the theoretical fluence values are compared with the empirically found fluences. It is not that surprising that the actual effective fluence is slightly higher as some loss of energy can be assumed when a lens profile is machined instead of a flat bottomed feature square as was done to find the ablation curve.
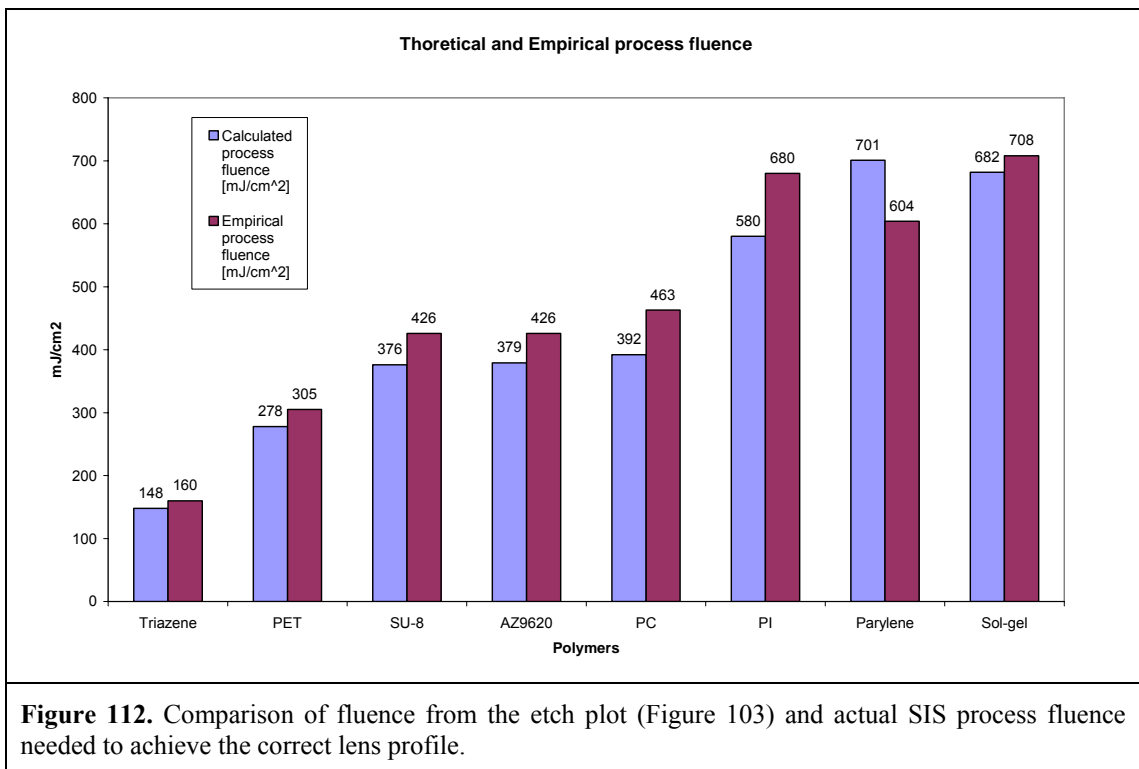
Polymer	% difference between calculated and empirically found fluence to etch a lens.
Triazene	8.1
PET	9.7
SU-8	13.3
AZ9620	12.4
PC	18.1
PI	17.2
Parylene	-13.8
Sol-Gel	3.8

Table 21. Differences between calculated and empirically found fluence values for laser etching lenses into various polymers. For all materials but Parylene a higher fluence than found from the etch plot was needed to achieve the right lens profile by SIS.

It is not understood why Parylene behaves in a fashion opposite to the other materials and further investigations would be needed to be able to explain this phenomenon. There is no clear correlation between calculated and empirical fluence and no simple factor can be applied that would cover a range of materials. This is not that surprising as the polymers do show quite different ablation behaviour in general. Nonetheless the discrepancy is not that big and for all polymers clearly below 20%. There is no clear link to the absorption coefficient, either, although the discrepancy is rather higher when α is bigger. As a rule of thumb between 10% and 20% more energy is needed to laser etch a lens shape than the value picked from the ablation curve representing the slice thickness.

Figure 112. Comparison of fluence from the etch plot (Figure 103) and actual SIS process fluence needed to achieve the correct lens profile.

7.3 Conclusions

It is remarkable that in all the materials tested at least part of the lens is etched. Even in the three materials not well suited for the SIS process (PET, Parylene, Sol-Gel) lenses could probably be cut that meet certain requirements if special care, process tuning and/or extra post-processing is applied. It has not been the objective of these studies to produce a perfect lens for each material, but looking at the results of the different polymers it can be said that with minor adaptations SIS can be applied to polymers other than PC. The assumptions and conclusions drawn from PC machining are transferable to other polymers as long as their ablation characteristics are known. In order to be able to predict the result of micro-structuring a polymer or indeed any ablatable material at any wavelength it is necessary to know the form of the ablation curve and how the surface appears after a few tens of pulses at around the process fluence. With the current knowledge and the use of the imaging system that has been employed there is no obvious reason why SIS could not be applied to micro-structure any other material that ablates well at a fluence below 1 Jcm^{-2}.

1. The optical materials ORMOCORE and ORMOCLAD are available from Micro Resist Technology, Berlin, Germany.

2. R. Srinivasan, V. Mayne-Banton, Appl. Phys. Lett. 41, 576 (1982)

3. P.E. Dyer, Appl. Phys. A 77, 167 (2003)

4. L.L. Moro et al. SPIE Vol. 5214, 83 (2004)

5. K.H. Haas, H. Wolter, Curr. Opin. Solid State Matter. Sci. 4, 571 (1999)

6. S. Obi, M.T. Gale, A. Kuoni, N. De Rooij, Microelec. Eng. 73-74, 157 (2004)

7. M.K. Ghantasala, J.P. Hayes, E.C. Harvey, D.K. Sood, J Micromech. Microeng. 11, 133 (2001)

8. M. Heckele, W.K. Schomburg, J. Micromech. Microeng. 14 R1–R14 (2004)

9. M.R. Hauer, DISS. ETH NO. 15422

10. R. Machorro, L.E. Regalado, J.M. Siqueiros, Appl. Opt. 30, 2778 (1991)

11 P.E. Dyer, S.D. Jenkins, J. Sidhu, Appl. Phys. Lett. 49, 453 (1986)

12 B. Hopp, Z.S.. Bor, E. Homolya, E. Mihalik, Appl. Surf. Sci. 109/110, 232 (1997)

13 T. Dumont, T. Lazare, T. Lippert, T. Wokaun, Appl. Phys. A 79, (2004)

14. R. Srinivasan, V. Mayne-Banton, Appl. Phys. Lett. 41, 576 (1982)

15. P.E. Dyer: Laser Ablation of Polymers, in Photochemical Processing of Electronic Materials, ed. by I.W. Boyd, R.B. Jackman (Academic, London 1992)

16. C.-R. Yang, Y.S.Hsieh, G.-Y. Hwang, Y.-D. Lee, J. Micromech. Microeng. 14, 480 (2004)

17. A.S. Holmes, IEE Proc.-Sci. Meas. Technol. 151, No. 2 (2004)

8 Summary, conclusions and outlook

8.1 Summary

In this thesis a novel technique to cut micro-structure arrays into polymers using a KrF laser with nanosecond pulse length is presented. The so-called Synchronised Image Scanning (SIS) method is systematically introduced by explaining the technique for four different applications of increasing complexity: thin film patterning, hole drilling, tapered nozzle drilling and structuring of surfaces with 3D micro-features of various geometries. The potential of SIS is further explored by direct comparison with the Step & Repeat method, highlighting several advantages of SIS such as higher quality features, consistency and efficiency. Micro-structure arrays of features with various geometries like lenses, prisms or corner cubes machined into Polycarbonate (PC) are presented. By concentrating on lenses as a very important optical component the achievable quality is determined by measuring the lens surface profile and surface roughness as well as carrying out some basic optical tests. As a by-product various measurement methods are evaluated. In order to get quantitative results four different metrology tools are used (optical microscopy, Scanning Electron Microscopy (SEM), White-light Interferometry (WLI) and stylus profiling). It is found that measuring these optical micro-structures is nearly as hard as creating them. By determining the ablation behaviour of the material in question, in this case Polycarbonate, it is possible to get the necessary parameters for the mask pattern design – arguably the key element of the SIS process. It is shown that with the right laser parameters and scan methods it is possible to produce micro-lens arrays closely matching the designed geometry and with good optical behaviour.
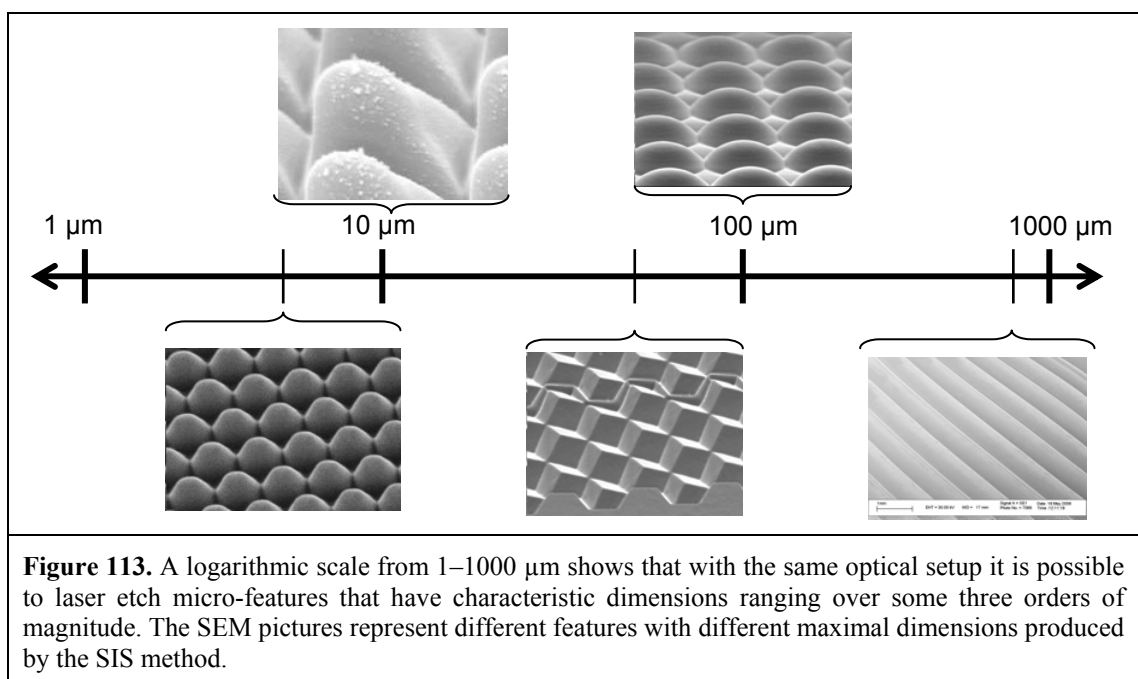
Further investigations are made into the influence of ablation debris on the structures and into the relatively high surface roughness of the features. The issue of ridge-like

artefacts between scans that appear when convex or positive features are created is explained, and a systematic investigation into ways of eliminating them is presented. It is found that the surface quality achieved when cutting geometrically accurate features is not acceptable for optical structures as the light scattering is too high. To address this issue a post-process employing low fluence and uniform exposure by a few tens of pulses is developed; this improves the surface quality significantly.

To get a better idea if the principle of SIS works in a more general case test experiments are expanded to materials other than Polycarbonate. It is demonstrated that micro-structures of a similarly high quality as those machined in Polycarbonate can be obtained in other materials and the same lens design is successfully laser etched into Triazene polymer, SU-8 and AZ9620 photoresists and Polyimide (PI).

8.2 Conclusions and outlook

Based on the experiments and findings presented in this thesis it can be said that SIS opens up a novel path to structuring surfaces with a wide variety of micro-features which can spread in lateral dimensions over three orders of magnitude without changing the optical system. Figure 113 shows a logarithmic scale from 1 μm to 1000 μm with

Figure 113. A logarithmic scale from 1–1000 μm shows that with the same optical setup it is possible to laser etch micro-features that have characteristic dimensions ranging over some three orders of magnitude. The SEM pictures represent different features with different maximal dimensions produced by the SIS method.

corresponding SEM pictures of micro-features with different dimensions produced by the SIS method. All features shown in Figure 113 have been machined with the same optical setup. This shows that beside the geometrical freedom, SIS offers also a wide dimensional range without time consuming and costly modifications to the beam delivery system.

The simple model based on the well-known etch rate-fluence dependence which obeys a form consistent with Beer's law used to find the right apertures and laser parameters is in good agreement with the results achieved. Using software that has been developed as part of these investigations to generate the mask pattern makes the mask design efficient and has been shown to deliver consistent results.

With the successful elimination of the artefacts generated when machining convex structures it is shown that the SIS process is well understood and that there is scope to deal with unexpected issues. The same is true for the surface enhancement process which reduces the roughness and therefore the light scattering of optical micro-structures significantly making them more efficient. It shows that by learning from previously made observations, problem solving can be made more efficient. Although laser polishing as presented here can be applied relatively easily, it is nevertheless an additional process step which influences the efficiency negatively. To eliminate this extra process step there is the option to integrate an energy modulating polishing aperture in the mask pattern containing all the other apertures. The features are then polished just after completion as this aperture is dragged directly behind the other apertures. But even this integrated polishing reduces the efficiency as the laser energy used for polishing cannot be employed to cut features. It would therefore be beneficial to achieve a higher surface quality directly by addressing what has been identified as the main cause for the surface roughness i.e. the groove and rim on the edge of each imaged

aperture. This could be done by blurring the hard edge of the binary apertures with features smaller than the resolution of the imaging lens.

The excellent results achieved when ablating polymers other than Polycarbonate provide strong evidence that the applied ablation model provides a good description of the laser-material interaction. Although only a selection of materials which have an ablation threshold well below 1 Jcm^{-2} at the 248 nm irradiation wavelength are investigated in this work, it seems reasonable to infer that SIS can equally work for materials demanding higher fluences and/or a different irradiation wavelength. There is no reason why with suitable optics for the beam delivery system it should not be possible to laser etch micro-structures by SIS, into, for instance, Borosilicate glass at ~10 Jcm^{-2} with a 193 nm ArF laser or into AlO_2 at ~8 Jcm^{-2} with a 248 nm KrF laser. For the latter it is already known that a polishing effect similar to the one in Polycarbonate reported here can be achieved [1]. The work in this thesis should give a suitable foundation to build on and to straighten the path to exploring the direct laser 3D structuring of other materials at various wavelengths.

Figure 114. Demonstrator of large area micro-lens array. The author (right) and a colleague are presenting a 1 m x 1.5 m sample with a micro-lens array of ~500 x 10^6 lenses. The sample was produced on the Exitech PPM 601E system on which the sample rests.

During the time in which the research for this thesis was carried out SIS generated a lot of interest for industrial use. A particular attraction is the capability to micro-structure large area substrates making this technique well suited for advanced display device applications. Figure 114 shows

an advanced display demonstrator of a 1 x 1.5 m sample with ~500 x 10^6 individual lenses that was fabricated by SIS. Other fields of interest are advanced lighting, large area waveguide structures, MEMS and fast prototyping of micro-optics. Although SIS is an efficient process, it is in most cases not fast enough for use in the mass production of such structures. It can much rather compete with conventional master cutting tools like diamond grooving to produce masters for a replication process.

SIS has matured considerably over the past few years and many sample tests producing other structures have been carried out which are not presented in this work. Table 1 summarises the main characteristics and parameters of other micro-structures produced by SIS. To push the boundaries to smaller features and steeper angles other projection optics are needed. Nevertheless with high resolution optics and ultra precise stages it should be possible to direct etch features smaller than 1 μm by SIS. Besides machining smaller features a high NA projection lens also addresses the wall angle limit and

- Feature sizes x: 5 μm – 1000 μm
- Feature height or depth z: 2 μm – 200 μm
- Wall angles and slopes α: 4° – 90°
- Fast micro-lenses f# < 2
- Any lens geometry (e.g. a-spherical, fresnel, elliptical)
- A vast range of optical geometries (e.g. moth eye, corner cube, prisms)
- High aspect ratio features (4:1)
- Optical surface finish (RMS roughness < 20 nm)
- Tight geometrical feature tolerances (±0.3 μm)
- 100% fill factor (with various packaging, e.g. hexagonal, square)
- Large area processing (demonstrated up to 1900 mm x 1400 mm)
- Fast rate for feature production: > 12 x 10^6 per h of a micro-lens with d = 100 μm, sag = 25 μm (80W laser)
- Process time: ~12h for 3 m^2 area 10 μm deep structures (80W laser)
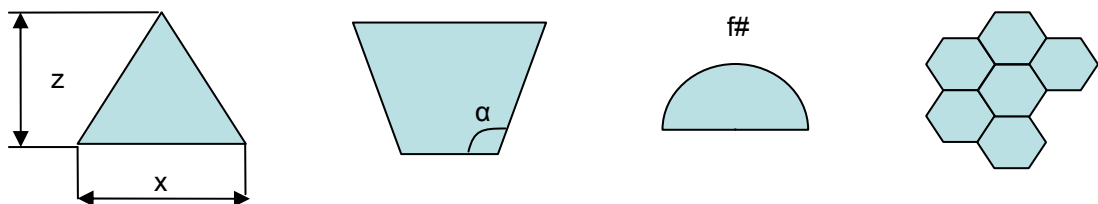

Table 22. List of state of the art properties achievable by SIS of micro features and arrays thereof and two examples of process speed and time. The geometrical and dimensional properties can generally be achieved by DUV ablation in polymers but the process time would go up by at least a factor of five.

enables features to be machined with vertical walls so that it should be possible to produce hemispherical micro-lenses. Additionally the aspect ratio of features could most likely be extended.

Where there is light, there is also shadow; the main issue which prevents SIS to be applied for commercial products is that so far it has not been possible to structure large areas without some inhomogeneous appearance. Although in the microscopic view there are barely any errors detectable, in the macro-view the sensitivity of the human eye for repeated or random irregularities is very high. This is especially true for display applications where the structured film is illuminated in various ways. The irregularities of a micro-structured area can have different causes; some are known, like stitching inaccuracy between scans, debris deposition within one image scan or from scan to scan, but others are not yet understood. The debris issue just mentioned could be addressed by especially designed polymers [2] where all material is vaporised or by a highly efficient debris extraction unit.

To turn direct laser ablation into a recognised competitor to conventional master cutting methods like micro-grooving, more work needs to be done and further improvements need to be realised; but the technique presented here does have real potential.

A useful side product of this work on micro-structuring surfaces is that it has driven an intense investigation into metrology solutions for measuring the micro-structures. As high level quality control is very important for any newly emerging technology trying to establish itself in industry, a significant amount of time was allocated to finding ways of measuring and evaluating the quality of the laser etched features. It can be concluded that with optical inspection and a modified surface profiler plus refraction tests of individual lenses some tools have been made available to quantify the quality of these

optical micro-features. Further work needs to be done to bring these tools to maturity and other techniques need to be investigated, but a good foundation has been laid with the tools presented.

1. K.L. Boehlen, P.T. Rumsby, A. Cerezo, M. Huang, SPIE Vol. 4557 (2001)

2. T. Lippert, C. David, M. Hauer, C. Phipps, A. Wokaun, Laser Eng. 29, 734 (2001)

Curriculum vitae

Personal details

Name: Karl Lukas Böhlen
Date of birth: 12 January 1969
Nationality: Swiss

Education

2002-2009   **University of Hull**, Hull, UK
             Part-time PhD in Applied Physics

1996-2000   **University of Applied Sciences**, Biel, Switzerland
             BSc in Micro-Technology

1995-1996   **School for Business and Industrial Education**, Biel, Switzerland
             University entrance qualification

1985-1989   **Häner AG**, Mühleturnen, Switzerland
             Apprenticeship as Mechanical Engineer

Work experience

2007 to date **Crealas – Smart Micromaching GmbH**, Dübendorf, Switzerland
              Technical Director

2001-2006   **Exitech – Advanced Laser Technology Ltd**, Oxford, UK
              Senior Development Engineer

2000   **University of Applied Sciences**, Biel, Switzerland
              Project Manager

1992-1995   **Silent Gliss International AG**, Gümligen, Switzerland
              Tool Maker

1990-1991   **ETA SA**, Grenchen, Switzerland
              Mechanical Engineer

Publication list

J. E. A. Pedder, A. S. Holmes, R. Allott, and K. Boehlen, *Pulsed laser ablation for volume fabrication of micro-optical arrays on large-area substrates*, Proc. SPIE 6462, 64620W (2007)

Karl L. Boehlen, Phil T. Rumsby, Neil Sykes, and Céline Lefevre, *High-speed laser cutting of micro structures with submicron details*, Proc. SPIE 6261, 62611F (2006)

Andrew S. Holmes, James E. A. Pedder, and Karl L. Boehlen, *Advanced laser micromachining processes for MEMS and optical applications*, Proc. SPIE 6261, 62611E (2006)

Heather J. Booth, Charles E. Abbott, Ric M. Allott, Karl L. Boehlen, Jim Fieret, Jako Greuters, Paul Trimble, and James Pedder, *Laser micromachining techniques for industrial MEMS applications*, Proc. SPIE 5713, 190 (2005)

Karl L. Boehlen, Ines B. Stassen Boehlen, and Ric M. Allott, *Advanced laser micro-structuring of super-large-area optical films*, Proc. SPIE 5720, 204 (2005)

D.G. Lidzey, M. Voigt, C. Giebeler, A. Buckley, J. Wright, K. Boehlen, J. Fieret, R. Allott, *Laser-assisted patterning of conjugated polymer light emitting diodes*, Organic Electronic, Volume 6, 2005

Charles Abbott, Ric M. Allott, Bob Bann, Karl L. Boehlen, Malcolm C. Gower, Phil T. Rumsby, Ines Stassen Boehlen, and Neil Sykes, *New techniques for laser micromachining MEMS devices*, Proc. SPIE 4760, 281 (2002)

Karl L. Boehlen, Phil T. Rumsby, Alfred Cerezo, and Min Huang, *Fabrication of axisymmetric ceramic microparts using pulsed laser ablation*, Proc. SPIE 4557, 129 (2001)

Patent list

Method and apparatus for micro-structuring a moving substrate
Inventor: Boehlen Karl Lukas
WO2007135379 (2007)

Method of patterning a functional material on to a substrate
Inventors: Buckelay Alastair Robert, Giebler Carsten, Voigt Monika, Lidzey David George, Boehlen Karl Lukas, Fieret Jacob
WO2005101505, (2005)